Elastic e^+p to μ^+p Scattering Cross Section Ratios at 210 MeV/c with the MUon Scattering Experiment

by

Haley Reid

A dissertation submitted in partial fulfillment
of the requirements for the degree of
Doctor of Philosophy
(Physics)
in the University of Michigan
2024

Doctoral Committee:

Professor Wolfgang Lorenzon, Chair
Professor Myron Campbell
Professor Igor Jovanovic
Professor Bjoern Penning, University of Zurich
Professor James Wells

Haley Reid
hrreid@umich.edu
ORCID iD: 0000-0002-6936-8423

DEDICATION

To the younger me
who never could have dreamed that
we would grow so much.

ACKNOWLEDGEMENTS

I first want to thank my advisor, Wolfgang Lorenzon, for his advising and mentorship over the past five years. From our first meeting, you advocated for me as a person and as a researcher, and you encouraged me throughout my time working for you through strenuous classes, stressful beam times, and difficult moments during my PhD. Without your support, I would not have made it to where I am today, thank you. I am thrilled that I get to continue working for you!

To my MUSE collaborators, I am grateful to work with so many people that I genuinely enjoy being on this experiment with. Tanvi, Win, Anne, and Rachel, thank you for being friends and support during long shifts, meetings, and analysis projects. I am so glad we met through this project and have gotten to work together, and I am so thrilled to see all of you grow and succeed within and beyond MUSE. Ievgen and Ethan, thank you for your unwavering willingness to help, to explain, to provide mentorship and wisdom throughout my degree. I hope to positively influence others in my life the way you have in mine. Evie, Paul, Konrad, Steffen, Michael, Jan, Richard, and Tiko, I have greatly enjoyed getting to work with you all, and I am glad that I will get to continue doing so with MUSE!

My physics journey started at Florida State University, and there are many people I met there that have or continue to play big roles in my life. Jorge Piekarewicz, Yuko Hori, and Carlos Villa: you believed in me before I knew how to believe in myself, especially as I grew in my physics knowledge. Thank you for invaluable mentorship, kindness, and support. The chances you gave me led me to where I am now. My undergraduate physics friends! Juan, Andrea, Aodhan, Sarah, Kelly, Marcus, Admir, and Fabio: I made it through long days and late nights at Keen because of you all, and you're also part of why I kept loving physics. Juan, you have always been my main physics partner; thank you for every late night homework deliberation, post-exam celebration, and for seeing me for who I could be long before I could see it myself. We learned and struggled together, and I will always be grateful for that.

In my last five years at the University of Michigan, I have met truly wonderful people that have impacted my life. Myron: your mentorship throughout the Physics REU in 2018 played a major role in my choice to attend the University of Michigan for graduate school, and your

advice taught me to reach further and dream bigger; thank you for giving me life-changing opportunities and encouragement. Liana, Alyssa, and Matt: I have learned how to be myself because of you, and I am better because I know you. Thank you for every laugh, game night, movie night, adventure, bar, and park. Thank you bringing me to karaoke enough that I finally worked up the courage to do it myself, and for coming line dancing with me. I hope we get many more romcom movie nights and karaoke nights in the future, and I am so grateful to have you in my life.

Joe, Christina, Kevin, Avik, Chami, and Thomas: physics brought you into my life, and you brought adventure, excitement and the Michigan Center for Brains and Gains into my life. I can't thank you enough for all the amazing memories I have because I accompanied you outside my comfort zone. Erin, Sean, and Nora, I couldn't ask for a better group to have emotional support coffee and power through the last year of my PhD with. Sean and Nora, you rescued us from the office for coffee breaks and sustained us with support. Erin, from the first book recommendation, I looked forward to coming into the office because it was a place we shared. For every high and every low, you made West Hall feel more like home, and I am so excited to continue on in Switzerland with you. To our Survivor crew, the ritual of Wednesday nights has made every week brighter for the last three years. You all brought so much joy and love and laughter to our living room every single Wednesday, and it was constantly a highlight. The community we have together is my dream, so thank you all for making it come true. Annie and Ariana, finding you as friends was a key serendipitous moment in my life. Thank you for being such a big and beautiful part of my journey here, and I know that I am better because you both have been a part of it.

Finally, my longest standing supporters, my family. Mom, Dad, and Jake. Mom and Dad, thank you endlessly for believing unwaveringly in my abilities and potential, even when I wasn't sure of myself. You have been my cheerleaders from day one, and you have always been so excited to see me grow, to succeed, and to learn. You have seen me go through so much, changing and growing, and you have been with me every step of the way. I was able to pursue this opportunity because I grew up being taught that I could do anything; you gave me confidence and encouragement that helped me reach where I am today. Jake, thank you for being a kindred spirit. The growth we have experienced, both together and apart, has strengthened and taught me so much, and I am grateful to have you as my brother and friend.

This thesis is based upon work supported by the National Science Foundation under NSF grant PHY-2110229. The MUSE experiment is supported by the Department of Energy, NSF, PSI, and the US-Israel Binational Science Foundation.

TABLE OF CONTENTS

LIST OF FIGURES

FIGURE

LIST OF TABLES

TABLE

LIST OF ACRONYMS

MUSE MUon Scattering Experiment

PSI Paul Scherrer Institute

HIPA High Intensity Proton Accelerator

BH Beam Hodoscope

GEMs Gas Electron Multipliers

GEM Gas Electron Multiplier

BFM Beam Focusing Monitor

BM Beam Monitor

STT Straw Tube Tracker

SPS Scattered Particle Scintillator

DOCA Distance of Closest Approach

TOF time of flight

PID particle identification

TCPVs Target Chamber Post Vetos

TCPV Target Chamber Post Veto

L1 Level 1

L2 Level 2

DAQ Data Aquisition

RF Radio Frequency

ADC Analog-to-Digital Converter

ADCs Analog-to-Digital Converters

SiPM Silicon Photomultiplier

SiPMs Silicon Photomultipliers

PMTs Photomultipler tubes

QDC Charge-to-Digital Converter

TDC Time-to-Digital Converter

MCFD Mesytec Constant Fraction Discriminator

CFD Constant Fraction Discriminator

MQDC Mesytec Charge to Digital Converter

MPD Multi-Purpose Digitizer

LUX Large Underground Xenon

LZ LUX ZEPLIN

CI confidence interval

ABSTRACT

The proton radius puzzle names the discrepancy between measurements of the proton charge radius done with atomic hydrogen spectroscopy, muonic hydrogen spectroscopy, and elastic electron-proton scattering. This puzzle initialized in 2010 with the first published results of proton radius extraction from muonic hydrogen spectroscopy, and since then, the discrepancy found has been investigated without a conclusive result.

The MUon proton Scattering Experiment (MUSE) simultaneously measures elastic electron-proton and muon-proton scattering using the PiM1 beam line at Paul Scherrer Institute in Villigen, Switzerland. Using both positive and negative beam polarities, MUSE will extract the proton charge radius by scattering off a liquid hydrogen target and contribute precise data to the investigation of the proton radius puzzle. MUSE also aims to test lepton universality by comparing the scattering cross sections for electrons and muons at both polarities. In the quest for the radius, additional interesting physics such as two-photon-exchange effects and the extraction of the electric and magnetic form factors are included in the physics goals of MUSE.

The detector components of MUSE and their respective roles in data collection and analysis are explained, as well as the trigger and data acquisition employed by MUSE. This thesis highlights and details the design, construction, commissioning, and operation of the liquid hydrogen target and all of its system components, which have operated successfully in beam times since 2019. Improvements to the system and their motivations will also be discussed.

This thesis will discuss analysis development projects including path length reconstruction of scattered particles to contribute to scattering event identification, trigger reconstruction within the analysis for selecting on events that fire desired triggers, and corrections to the incident beam flux at the target to improve the accuracy of the scattering cross section calculation. Scattering data from ± 210 MeV/c is analyzed and differential cross section results are extracted. These differential cross section and cross section ratio results will be presented for ep and μp elastic scattering and discussed with respect to MUSE's physics goals as well as the test for lepton universality.

CHAPTER 1

Introduction

The work for this thesis is inspired by the proton radius puzzle, and its motivations are embedded in the birth and evolution of this puzzle over the last fourteen years and the capability to test the principle of lepton universality.

1.1 Proton Radius Puzzle

The proton constitutes a fundamental component of our understanding of physics, as well as our continued exploration of the universe. Ernest Rutherford, with his experiments in the 1910's, confirmed atoms to have an internal structure with a smaller charged nucleus orbited by lower-mass electrons [7]. In his initial reports, he named the emitted particles "hydrogen atoms," and they were later renamed as protons. With the proton's existence and general role established, the next step was to explore the nature of the proton.

The technology that would make this exploration possible came in 1932 with the construction of the first particle accelerator, done by Cockcroft and Walton [8]. We thus gained the ability to probe the proton's internal structure, for which the scattering theory was discussed by Rosenbluth in 1950 [9]. The first results from elastic electron-proton scattering from Hofstadter [10] in 1956 opened an entirely new discussion around the internal structure of the proton with Hofstadter concluding that is was prudent to gather more data at higher precision and absolute cross sections in order to further investigate.

Other notable early electron-proton scattering experiments that contributed to the measurement of the proton radius include work by Lehmann et al. at Orsay in 1962 [11], Hand at Stanford in 1963 [12], Murphy II at Saskatoon in 1974 [13], and work at Mainz in 1980 [14] - a summary of the early radius measurements can be seen in figure 1.1. Other early measurements obtained from hydrogen spectroscopy experiments started being reported in the mid 1990s, when the detector technology for spectroscopy reached the sensitivity needed for radius extraction.

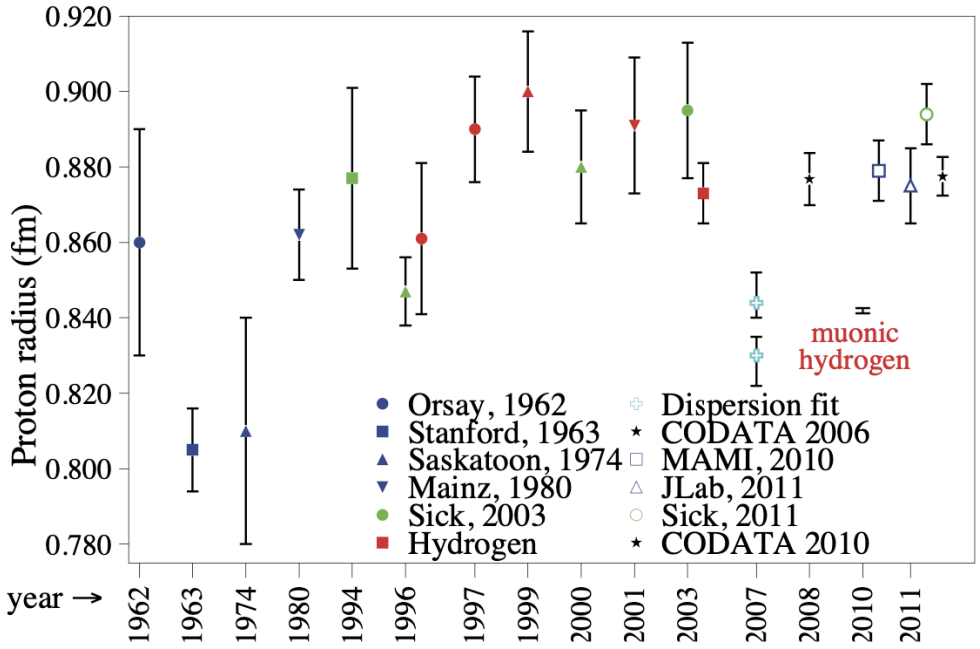

Figure 1.1: Summary of the proton charge radius measurements from the 1960s to 2010s. Figure from Ref. [1].

The proton charge radius had, up to 2010, been obtained using electron-proton scattering and hydrogen spectroscopy. In order to calculate the radius from a scattering measurement, we must look at the electric and magnetic form factors [15], which, when taken in the low Q^2 limit, can be defined as

$$\langle r_p^2 \rangle = -6 \frac{dG_E(Q^2)}{dQ^2}\Big|_{Q^2=0}. \tag{1.1}$$

In this equation, r_p is the proton charge radius, G_E is the Sachs electric form factor, and Q^2 is the momentum transfer. With this relation, we can then look at the equation for the one-photon-exchange approximation ep elastic cross section in terms of the electric and magnetic form factors given by

$$\frac{d\sigma}{d\Omega} = \left(\frac{d\sigma}{d\Omega}\right)_{Mott} \frac{1}{1+\tau}\left[G_E^2(Q^2) + \frac{\tau}{\epsilon} G_M^2(Q^2)\right], \tag{1.2}$$

where $Q^2 = -4EE'\sin^2(\frac{\theta}{2})$, E and E' are the incident and scattered lepton energy, θ is the scattering angle. $\tau = \frac{Q^2}{M^2}$, M is the proton mass, $\epsilon = [1 + 2(1+\tau)\tan^2(\frac{\theta}{2})]$, and $\left(\frac{d\sigma}{d\Omega}\right)_{Mott}$ is

the Mott cross section, given by

$$\left(\frac{d\sigma}{d\Omega}\right)_{Mott} = \frac{\alpha^2 \cos^2(\frac{\theta}{2})}{4E^2 \sin^4(\frac{\theta}{2})} \frac{E'}{E}. \tag{1.3}$$

From the experimentally measured scattering cross section, the electric and magnetic form factors are extracted by either a Rosenbluth separation by holding constant the momentum transfer while varying beam energy and scattering angle, or by directly fitting form factor models to the measured cross section. At low Q^2, the magnetic form factor is suppressed, and the electric form factor dominates in the expression for the scattering cross section. By fitting and extrapolating the function to $Q^2 = 0$, we can calculate the slope at the intercept to find the proton radius, from equation 1.1. The choice of fitting methods for this procedure has been discussed extensively, such as in Ref. [16], which considers multiple key obstacles in the process of extracting the radius from the scattering cross section. These include the difficulty of measuring the absolute cross section to a high enough precision, the truncation of polynomial fits often used on these data sets, as well as accounting for the normalization of different data sets.

For hydrogen spectroscopy experiments, s-states are the focal point because these are the only states of the hydrogen atom that have a non-zero wavefunction when evaluated at the origin, which is representative of the non-zero probability that the orbiting electron is inside of the proton. The energy for a hydrogen s-state is given by

$$E(nS) \approx -\frac{R_\infty}{n^2} + \frac{L_{1s}}{n^3}, \tag{1.4}$$

where n is the principal quantum number, R_∞ is the Rydberg constant, and L_{1S} is the Lamb shift, which is dependent on the proton radius r_p by $8172 + 1.56r_p^2$ MHz. From this, it can be shown that the energy shift for the s-states is

$$\Delta E = \frac{2}{3}\pi\alpha|\psi_S(0)|^2 r_p^2. \tag{1.5}$$

This energy shift measurement and radius extraction probes in the Q^2 range of 10^{-4} to 10^{-5}, which is lower than the Q^2 range accessible by ep scattering experiments (the low end of the Q^2 is 10^{-3} [1]).

Until 2010, the charge radius of the proton was measured by electron-proton scattering and atomic hydrogen spectroscopy. This charge radius was widely accepted and reported by CODATA as a fundamental value, at 0.88 fm [17, 18]. Still, the uncertainty on this measurement was large, and efforts continued to more precisely measure the radius. Muonic hydrogen spectroscopy was an especially important pursuit because of the opportunity for

much more precise measurement because the Bohr radius for a muonic hydrogen atom is 207 times smaller than the Bohr radius for an atomic hydrogen atom, which is given by

$$a_B = \frac{\hbar c}{c^2} \frac{1}{m_e \alpha}, \tag{1.6}$$

where m_e is the electron mass, α is the fine structure constant, and a_B is the Bohr radius. The likelihood of overlap in the wavefunction is approximately given by the ratio of the proton volume to the Bohr radius volume, which is

$$\left(\frac{r_p}{a_B}\right)^3 = (\alpha r_p)^3 m_l^3, \tag{1.7}$$

where r_p is the proton charge radius and m_l is the lepton mass. Therefore the probability of overlap is 8 million times greater for muonic hydrogen than for atomic hydrogen, and muonic hydrogen is much more sensitive to the radius of the proton.

In 2010, the first radius measurement from muonic hydrogen spectroscopy done by Pohl et al. [19] at PSI produced a value of 0.84 fm with crucially smaller error bars, leaving more than 5 standard deviations between the accepted CODATA value at the time and this new value. Three years later, Antognini et al. [20] provided another muonic hydrogen radius measurement, agreeing with the first and solidfying the mystery of the discrepancy between old and new measurements: the proton radius puzzle was established by this new method of measurement and its conflicting results.

Since 2010, spectroscopy of both electronic and muonic hydrogen as well as electron-proton scattering have provided color to the picture of the proton radius. Notably, electron-proton scattering experiments in 2010 at Mainz [21] and 2011 at Jefferson Lab [22] both agreed with earlier (larger) measurements of the radius, while PRad's result in 2019 [23] was the first electron scattering result to agree with the muonic hydrogen result. However, another ep scattering result just three years later still produced 0.88 fm, leaving us with an unsolved puzzle. Electronic hydrogen spectroscopy had disparaging results as well, with Beyer [24] and Bezignov in 2019 [25] agreeing with the smaller radius results but Fleurbaey [26] siding with the scattering experiments on the larger radius value. Two more hydrogen spectroscopy experiments published results in 2020 [27] and 2022 [28], both of which stood closer to the middle of the gap between the smaller and larger values, rather than reinforcing one of the previous measurements. Reanalyzing older data sets did not fare much more successfully in the effort of converging on a value, with a refitting in 2018 [29] producing a value in agreement with the larger radius and a refitting in 2019 [30] agreeing with the smaller radius. While CODATA continued using the larger radius definition in 2014 after the two muonic hydrogen

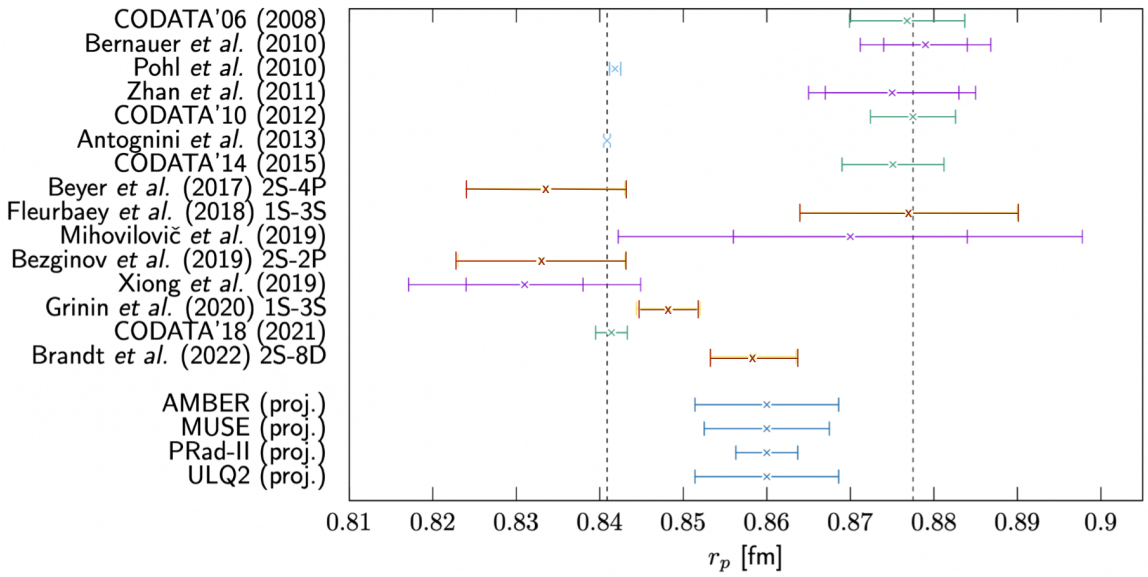

Figure 1.2: Summary of the proton radius puzzle and measurements reported since 2010. Points plotted in green are the CODATA published values, purple are electron-proton scattering, light blue are muonic hydrogen spectroscopy, red are atomic hydrogen spectroscopy, and darker blue are planned or in-progress experiments.

spectroscopy measurements [31], their 2018 report had shifted the proton charge radius value to be more closely aligned with the smaller radius [32]. Despite this, there is still not general agreement on the "true value."

With all the scattering and spectroscopy experiments that have contributed to the clarity of the proton radius puzzle over the last fourteen years, summarized in figure 1.2, we have far more information and nuance concerning conflicting results and possible causes of both the initial discrepancies and the persistent unanswered questions. In addition to MUon Scattering Experiment (MUSE), other experiments that are actively running or planning to contribute to the proton radius puzzle include PRad II [33] with an adjusted set up from their first data collection of electron-proton scattering, AMBER, also doing muon-proton scattering at CERN, though at much higher beam energies than MUSE [34], MAGIX at MESA, planning to do electron-proton scattering at extremely low Q^2 [35], and the ULQ2 experiment at Tohoku [36]. As we add data points to the overall picture, there are several popular explanations for the lack of convergence on a single value for the proton radius.

One explanation for the persisting measurement discrepancy points to experimental error that has not been well-studied or well-understood. Between the short lifetime of the muon and systematic errors involved in scattering experiments, it is possible that the distance

between found values is hidden in the margin of error that is larger for data gathered from scattering than it is from spectroscopy. Additionally, each scattering experiment handles its systematic uncertainties in its own way, and there may be differences in the processes.

Aside from experimental error, novel conventional physics is another consideration in the source of radius measurement discrepancies. Since scattering cross sections are determined to the one-photon-exchange (Born) approximation, higher order corrections to the cross section may not be properly accounted for. Scattering cross section measurements used unpolarized beams, and these cross sections provided an avenue to extract the electric and magnetic form factors.

When experiments began utilizing polarized beams for polarization transfer measurements, the resulting difference in the extracted ratio of proton electric to magnetic form factors $\frac{G_E}{G_M}$ [37, 38]. Two-photon-exchange effects remain a point of interest within the proton radius measurement in part because calculated form factor ratio using Rosenbluth separation is not in agreement with ratios obtained through polarization transfer measurements [39].

While the Standard Model has been well-established and in many cases successfully describes the universal structure and behavior of particles, cases such as the proton radius puzzle pose the possibility that the Standard Model is not complete in characterizing fundamental particles and their behavior. Beyond the Standard Model physics is being explored by a host of experiments, a section of which Section 1.2 discusses current experiments investigating the principles of lepton universality, one of the tenets of the Standard Model.

The piece of this puzzle that is still missing is a radius extraction from elastic muon-proton scattering, which would complete the picture of obtaining the radius with both leptons from both experimental methods. Muon scattering presents some difficulties that are not relevant in electron-proton scattering, such as the background of a mixed beam with electrons and pions, which MUSE handles using particle and reaction identification (more details are discussed in sections 4.2.1 and 4.2.2). Additionally, muon decay further complicates the task of successfully detecting muon scattering events - the decay processes are discussed explicitly in section 2.1.1.

MUSE takes advantage of the mixed-beam during data-taking by measuring both electron-proton and muon-proton scattering simultaneously, which not only gives a direct comparison of the cross sections with a consistent regiment for handling systematic uncertainties, but also allows for the opportunity to measure the two-photon-exchange effects by using positive and negative polarity beam, as well as test/contribute to the constraints of lepton universality with cross section ratios.

1.2 Lepton Universality

A main principle of the Standard Model of particle physics dictates that leptons (muons, electrons, and taus) have the same interaction strength with respect to other particles. However, the Standard Model does not suffice to explain a number of observed facts, including the matter-antimatter asymmetry, as well as the presence of dark matter which, though it has not been observed, has many astrophysical observations that support its existence. The endless possibilities of an incomplete model that describes fundamental particles and their behaviors has inspired a host of experiments and searches. In addition to MUSE and its measurement of elastic μp scattering, efforts in searching for violations of lepton universality include the precision measurement of the anomalous muon magnetic moment, or the muon g-2 value, which has produced particularly interesting results in the context of the testing and constraining of lepton universality and the search for "new physics."

Operating on the principles of lepton universality, we expect interactions between protons and electrons to have the characteristics as between protons and muons, when the different masses are taken into account. Many of the current experiments investigating lepton universality are searching for violations of lepton universality through the measurement of decay processes, such as the beauty quark decay [40], where they are exploring discrepancies in the branching fraction of the beauty quark decay to two muons vs. to two electrons, which we would expect to be identical under lepton universality.

MUSE will be the first experiment to measure elastic muon-proton scattering to a high enough precision that allows the testing of lepton universality through the ep to μp cross section ratios. Additionally, by measuring the scattering for both electrons and muons within the same experimental environment, we can confirm that background and uncertainties for both cases are handled with the same prescription, providing an advantage in the process of calculating the ratios and comparing them to the theoretical calculations. The theoretical and experimental determination of cross sections and ratios will be discussed in more detail in section 5.1.

In addition to the proton charge radius and tests of lepton universality, MUSE is also probing two-photon-exchange effects through the e^+/e^- cross section ratio, given by

$$R^{e^+e^-} = \frac{\sigma^{e^+}}{\sigma^{e^-}} \approx \frac{|\mathcal{M}_\gamma^{e^+}|^2 + \mathcal{R}](\mathcal{M}_\gamma^{e^+} \times \mathcal{M}_{\gamma\gamma}^{e^+})}{|\mathcal{M}_\gamma^{e^-}|^2 + \mathcal{R}](\mathcal{M}_\gamma^{e^-} \times \mathcal{M}_{\gamma\gamma}^{e^-})}, \tag{1.8}$$

where the Born amplitude $\mathcal{M}_\gamma^{e^\pm}$ changes sign between electron and positron scattering, canceling out of the ratio, and the two-photon-exchange amplitude $\mathcal{M}_{\gamma\gamma}^{e^\pm}$ does not, leaving only the two-photon-exchange contributions [38]. Therefore the e^+/e^- cross section ratio

provides direct access to measuring two-photon-exchange effects and gaining insight on how it contributes to scattering measurements.

The following chapters will discuss work done in an effort to extract scattering cross sections and to compare the electron-proton and muon-proton cross sections within the context of testing lepton universality by examining their interactions with protons. Chapter 2 will discuss the MUSE experimental set up: its components, the motivation behind instrument design and construction, and its data-taking progress. Chapter 3 focuses on the liquid hydrogen cryotarget, which provides the source of protons for scattering events, including its design and construction, as well as its operation during beam time over the last five years. Chapter 4 discusses the dedicated analysis development projects that I played a major role in, including path length reconstruction for scattered particles, event trigger reconstruction, and corrections to the flux calculation for cross section normalization. Chapter 5 details the cross section analysis and results for the electron-proton scattering and muon-proton scattering, and ultimately the cross section ratios. In chapter 6, I conclude with reflections on results and next steps for MUSE in data-taking and analysis.

CHAPTER 2

The MUon Scattering Experiment

The MUSE is performed using the PiM1 beam line at PSI in Villigen, Switzerland. PSI provides the mixed particle beam and beam time for MUSE to measure the proton radius through simultaneous ep and μp scattering. The mechanisms for this environment are detailed in section 2.1.

2.1 PiM1 Beam Line at PSI

2.1.1 The High Intensity Proton Accelerator and the M Production Target

PSI hosts the world's most powerful High Intensity Proton Accelerator (HIPA), which produces a 590 MeV and 1.4 MW proton beam that is then utilized by multiple facilities at the lab: the Swiss Spallation Neutron Source (SINQ), the Swiss Muon Source (SμS), and the Swiss Light Source (SLS).

The proton beam is produced in the HIPA through multiple accelerators, where, first, the protons are pre-accelerated by a Cockcroft-Walton column [8], which brings the protons up to a momentum of 870 keV/c. After the Cockcroft-Walton acceleration, the protons enter the Injector 2 cyclotron and are accelerated up to 72 MeV/c, then passed to the final accelerator: the 8-sector Ring Cyclotron. This Ring Cyclotron takes the protons and accelerates them up to 590 MeV/c over 220 revolutions at the center of the Ring.

The resulting beam produces a bunch of protons every 19.75 ns that is passed down the beam line to the M target, which is the starting point for the PiM1 beam line (as well as the PiM3 beam line, another high π flux beam at PSI). The proton beam also goes an E target from which there are more secondary π beam lines: PiE1, PiE3, and PiE5. Later on, two muon secondary beams μE1 and μE4 were designed and added for in-depth muon studies at much lower momentum than PiM1, with a maximum momentum of around 28 MeV/c.

The start of the PiM1 channel is where the 590 MeV/c proton beam collides with the M target, which is a spinning graphite wheel that is 5.2 mm thick, made of graphite, and rotates with a frequency of 1 Hz. The interaction of the protons and graphite produces pions through the collision

$$pC \to \pi X, \tag{2.1}$$

in which X can be any state where C has broken into smaller nuclei through the interaction. From this pion production, the electrons and muons that we want for scattering are born through pion decay. Electrons are produced through two different decay processes: the first happens in two stages, where a neutral pion decays to two photons, which then interact with the carbon to produce an electron positron pair:

$$\begin{aligned} \pi^0 &\to \gamma\gamma \\ \gamma C &\to e^+e^- X. \end{aligned} \tag{2.2}$$

This pion decay has a branching ratio of $\approx 98.8\%$, and the other source of electrons is from the Dalitz decay,

$$\pi^0 \to e^+e^-\gamma, \tag{2.3}$$

which has a branching ratio of around $\approx 1.2\%$. Since a large majority of the electrons are produced at the M target from reaction 2.2, we have a similar source characterization for the pions as for most of the electrons.

The muons in the PiM1 beam are produced from charged pion decay:

$$\pi^+ \to \mu^+\nu_\mu \qquad \pi^- \to \mu^-\overline{\nu}_\mu. \tag{2.4}$$

This charged pion decay can happen at any point along the PiM1 beam line, so the time of flight MUSE uses for particle identification must accordingly handle the possibility of pions decaying to muons both before and inside the MUSE experimental set up. Additionally, muons can decay into electrons according to

$$\mu^- \to e^-\overline{\nu}_e\nu_\mu \qquad \mu^+ \to e^+\overline{\nu}_\mu\nu_e, \tag{2.5}$$

which both contributes more electrons and positrons to the beam, as well as further complicates particle identification, which also accounts for the muon to electron decay both before and in PiM1.

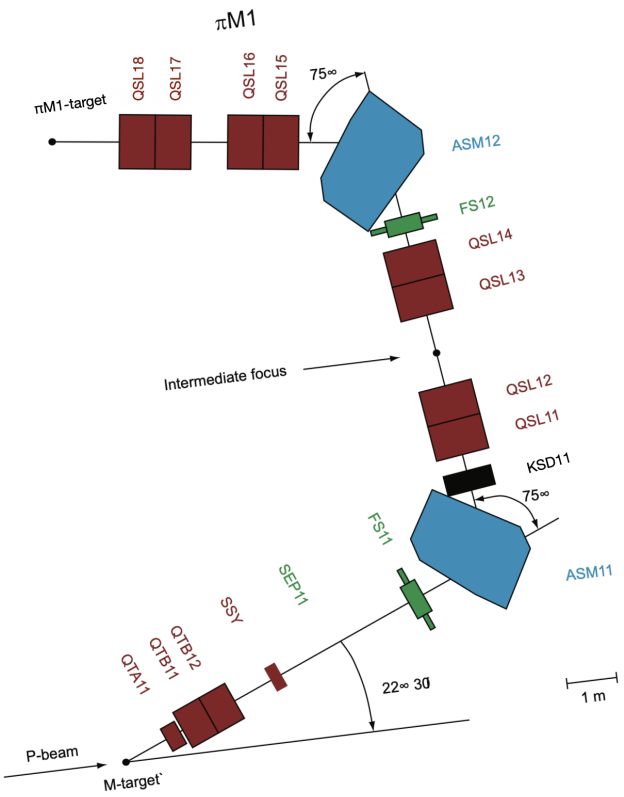

Figure 2.1: Drawing of the PiM1 channel. Figure from Ethan Cline [2]. The blue objects are dipole magnets, the red objects are quadrupole magnets, and the green objects are sets of moveable jaws that can increase or decrease the physical opening for the beam to pass through. The beam is dispersed at the intermediate focus and refocused, allowing for a better determination of the momentum.

2.1.2 PiM1 Channel and Beam Properties

The PiM1 secondary beam line is connected to the primary beam line of HIPA at the M production target, at an angle of 22°. The channel for this secondary beam line consists of sets of dipole and quadrupole magnets that bend and focus the beam of particles as it travels to the PiM1 area. The set up of all the channel elements can be seen in figure 2.1 [2]. Immediately after the M-target is a triplet of quadrupole magnets (QTA 11, 12, and 13) which function to increase the beam flux; the two doublets of quadrupoles (QSL 11-12 and 13-14) in between the dipoles ASM11 and ASM12 collaborate to create a momentum dispersion at FS13, the intermediate focus point. In the last stretch of the channel before the PiM1 area, the sets of quadrupole doublets QSL 15-16 and 17-18 work to focus the beam at the target for MUSE.

In order to optimize the time separation for the different particle species in the PiM1 beam line coming into the target in the MUSE set up, the specific beam momenta of 115,

Parameter	Value
Beam momenta, MeV/c	115, 160, 210
Scattering angle range	20° - 100°
Q^2 range for electrons	0.0016 - 0.820
Q^2 range for muons	0.0016 - 0.0799

Table 2.1: PiM1 beam kinematics MUSE utilizes for data taking.

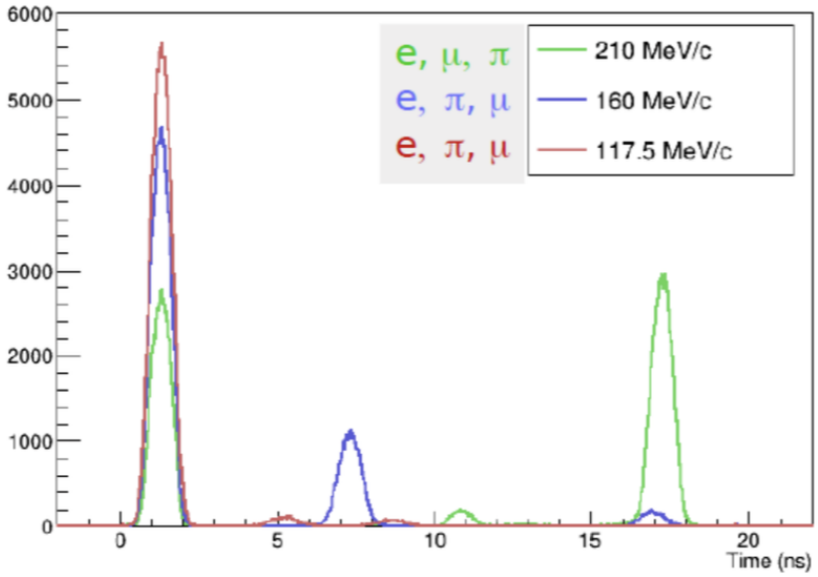

Figure 2.2: RF timing at 117.5, 160, and 210 MeV/c when doing tests to optimize time separation of particle species for MUSE data collection [3]. The legend shows the order of peaks with respect to their particle types.

160, and 210 were selected following studies done in 2013 [3]. The corresponding kinematics for MUSE can be seen in table 2.1, and the different momenta are taken into account when calculating the total flux for electrons, muons, and pions MUSE will receive.

Electrons, at a mass of 0.511 MeV/c^2, will take the same amount of time to travel from the M target to the beam hodoscope in the MUSE set up at all three momentum settings because they are relativistic. The pions and muons, with the same momenta and heavier masses of 139.57 MeV/c^2 and 105.67 MeV/c^2 respectively, will have slower velocities and arrive at the detectors after the electrons. The time separation between the three species at all momenta can be seen in figure 2.2, which also highlights the relative difference in the ratios of species between each momentum: 115 MeV/c is dominated by electrons, whereas 210 MeV/c has a similar count of electrons and pions. The full species make-up of particles at each momentum in the context of the expected flux for MUSE can be seen in table 2.2.

Momentum (MeV/c)	**Total Flux (MHz)**	e **Flux (MHz)**	π **Flux (MHz)**	μ **Flux (MHz)**
(+)115	8.3	8.05 (3.2)	0.17 (0.07)	0.08 (0.02)
(−)115	7.4	7.29 (3.25)	0.07 (0.03)	0.04 (0.02)
(+)160	16.9	10.65 (2.08)	2.03 (0.4)	4.23 (0.83)
(−)160	11.9	10.71 (2.97)	0.38 (0.11)	0.81 (0.22)
(+)210	79.2	9.5 (0.4)	6.34 (0.26)	63.36 (2.64)
(−)210	24.0	11.28 (1.55)	0.96 (0.13)	11.76 (1.62)

Table 2.2: MUSE projected flux by momentum and particle species. The number in parenthesis next to each value in the individual species columns shows the scaled down expected flux with respect to the overall expected MUSE flux of 3.3 MHz. More details around this calculation and these parameters are discussed in Ref. [3].

2.2 Detector Set Up

MUSE uses the PiM1 beam line to take electron-proton and muon-proton scattering, but it is not the only experiment that utilizes this area. In order to share occupation of PiM1, the experimental set up for MUSE was required to be fully contained in a moveable platform that would be craned in and out of PiM1 (shown in figure 2.3). This limited space budget, alongside the physics requirements that must be satisfied, provide the framework from which the detector components of MUSE were designed, built, and commissioned in the system.

The physics requirements for MUSE include:

1. identify particles by species and their decays without a magnetic spectrometer, both along the beam line and scattered from the target.

2. reconstruct scattering events that occur in the target region within the vacuum chamber using timing and tracking information of incoming and scattered particles.

3. cover the scattered particle range of $\phi = 20^\circ - 100^\circ$ and $\theta = \pm 45^\circ$.

With these prerequisites, the experiment contains a set of beam line (section 2.2.1) and scattering (2.2.2) detectors, shown in figure 2.4 that collect information and play specific roles in reconstructing scattering events.

2.2.1 Beam Line Detectors

The first detector inside the MUSE setup is the BH, shown in figure 2.5, which is comprised of four planes of scintillating paddles and provides precise timing information to determine particle identification when combined with the timing information from the accelerator. Its

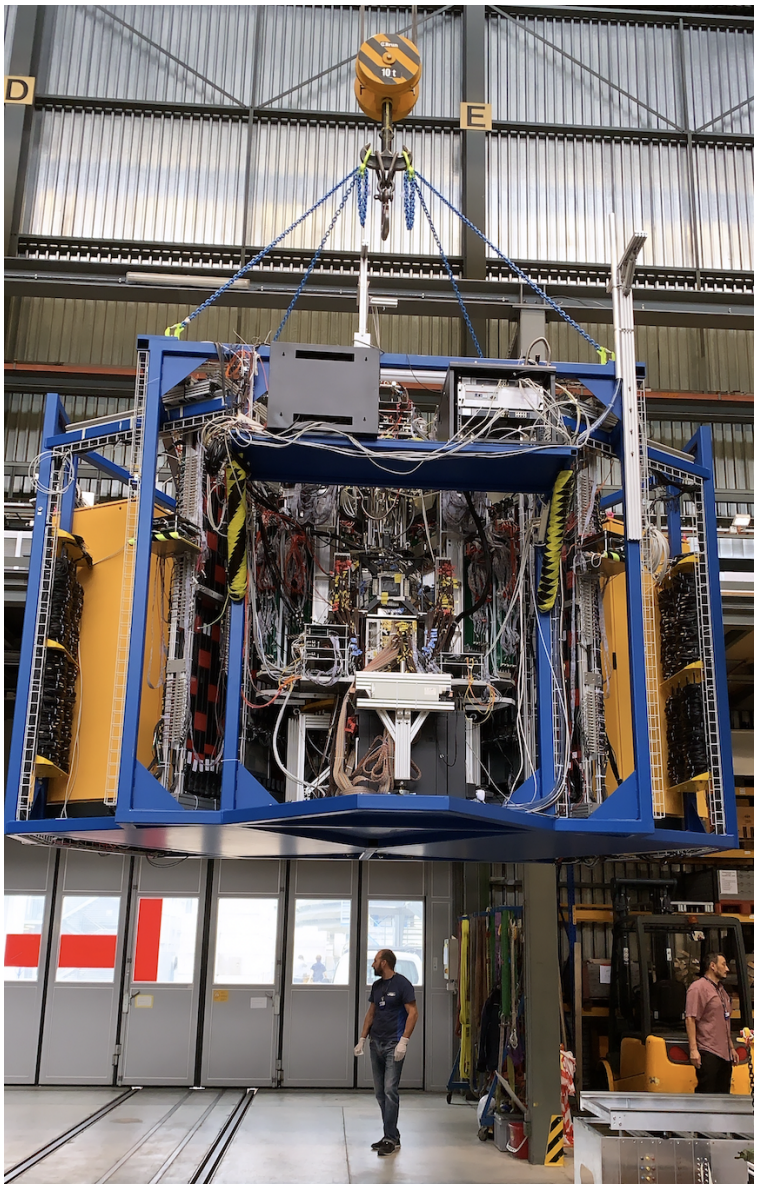

Figure 2.3: Photo of the MUSE set up being craned out of the PiM1 area on its platform.

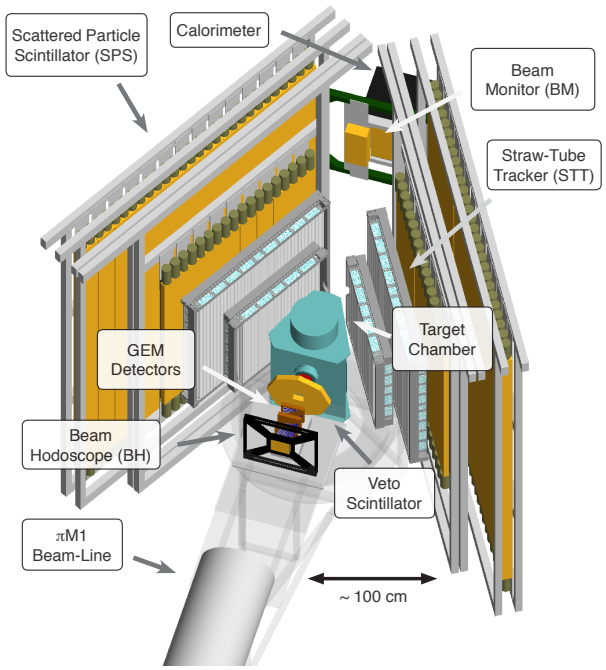

Figure 2.4: Schematic drawing of the MUSE set up and its beam line and scattering detectors. Generated in Geant4 by Steffen Strauch.

main purposes, in addition to particle identification, are providing beam flux and precise timing information for time of flight calculations for particles within the experimental set up. The four planes of the beam hodoscope are oriented in an alternating pattern between horizontal and vertically oriented scintillating paddles to improve the precision of the reported hit position of a detected particle.

The BH detector was designed and constructed by the group at Rutgers University. Each plane has 16 paddles that are all 100 mm long and 2 mm thick, but they vary in width: the six paddles at the center of each plane are 4 mm wide, and the five paddles on each side of the central six are twice as wide. This distribution of paddles is used so that the higher concentration of particles in the middle of the detector have a smaller chance of passing through the same bar, and it provides limitations for the rate in each paddle. More technical information about the BH can be found in Ref. [41].

The next detector in the beam line is a set of Gas Electron Multipliers (GEMs), which can be seen in figure 2.6 and constitutes the tracking detector for beam line particles going into the target. The GEM detector uses three or four planes(depending on the configuration) to detect a particle going through the plane, and it fits the pattern of hits to form tracks that show the trajectory of the particle as it travels to the target. The GEM chambers have a

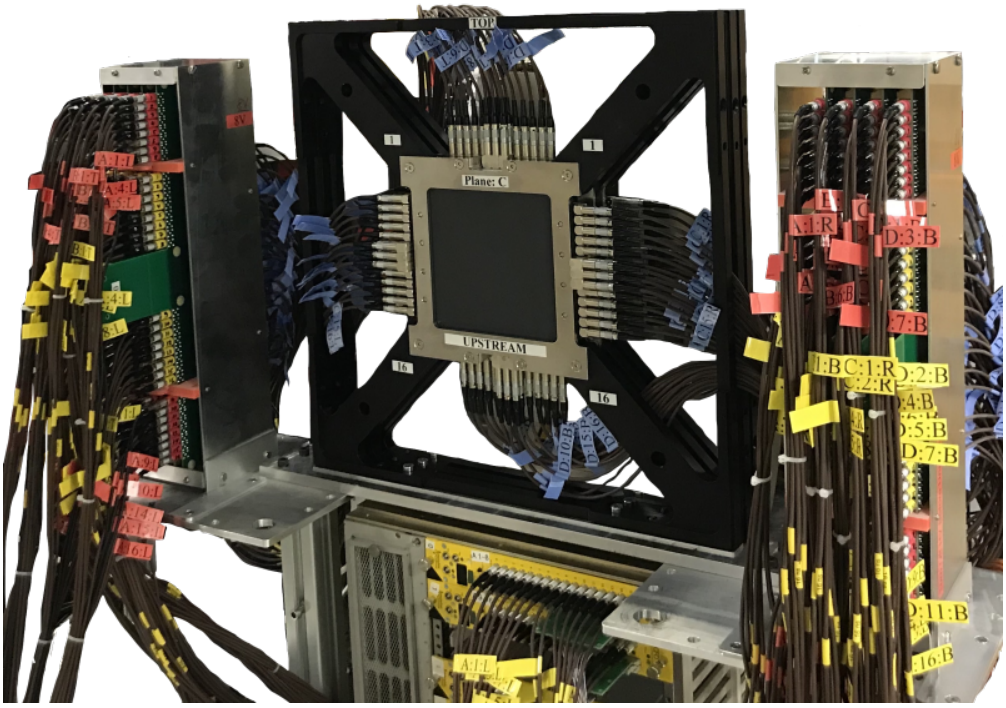

Figure 2.5: Photo of the BH detector, the detector furthest upstream in the MUSE set up.

gas mixture of 70% Ar and 30% CO_2, and a particle passing through a GEM plane locally ionizes the gas in that chamber, which amplifies the signal as the released electrons travel through the layers in the chamber [42].

The GEM detectors were built and are maintained by the Hampton University group, which were used previously in the OLYMPUS experiment [43]. They also use a very similar detector set up for experiments as Jefferson Lab. Each 10 cm by 10 cm chamber of the GEM detector utilizes four analogue pipeline voltage (APV) integrated circuits, each with 128 readout strips There are two APVs and 250 readout channels allotted for the x-direction and two APVs and 250 readout chambers allotted for the y-direction for each of the four chambers in the MUSE setup.

The beam veto detector, shown in figure 2.7, is the third detector in the MUSE set up and is the last detector upstream of the target and vacuum chamber; the veto is donut-shaped and is comprised of four trapezoidal scintillators that each have two Photomultipler tubes (PMTs) for digital readout. The purpose of the beam veto is to reduce the trigger rate by vetoing decaying particles or particles upstream of the target that are not on a trajectory to travel to the target region. The opening at the center of the veto has an inner radius of 3 cm and is roughly the same size as the vacuum chamber's entrance window, which has an inner radius of 3.1 cm.

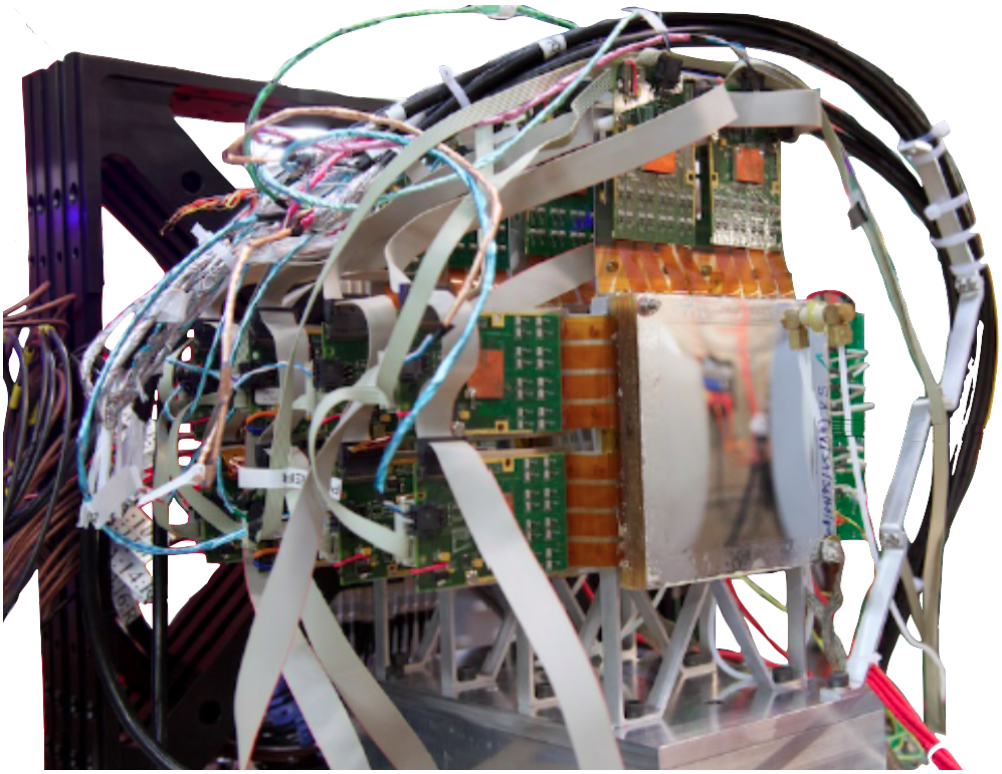

Figure 2.6: Photo of the GEM detectors for the MUSE beam line tracking.

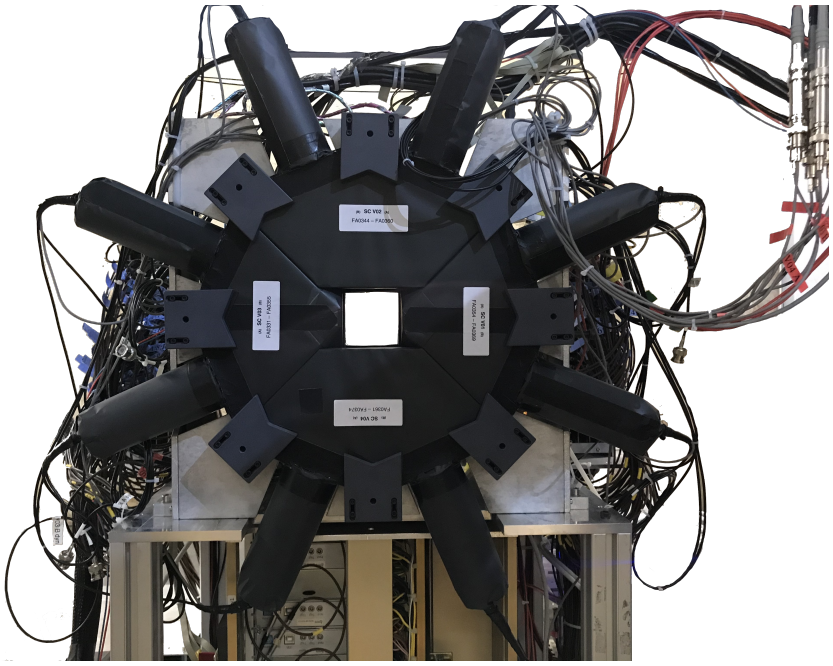

Figure 2.7: Photo of the beam line veto detector for MUSE. The opening at the center is aligned with the beam so that it matches the height and opening of the vacuum chamber entrance aperture.

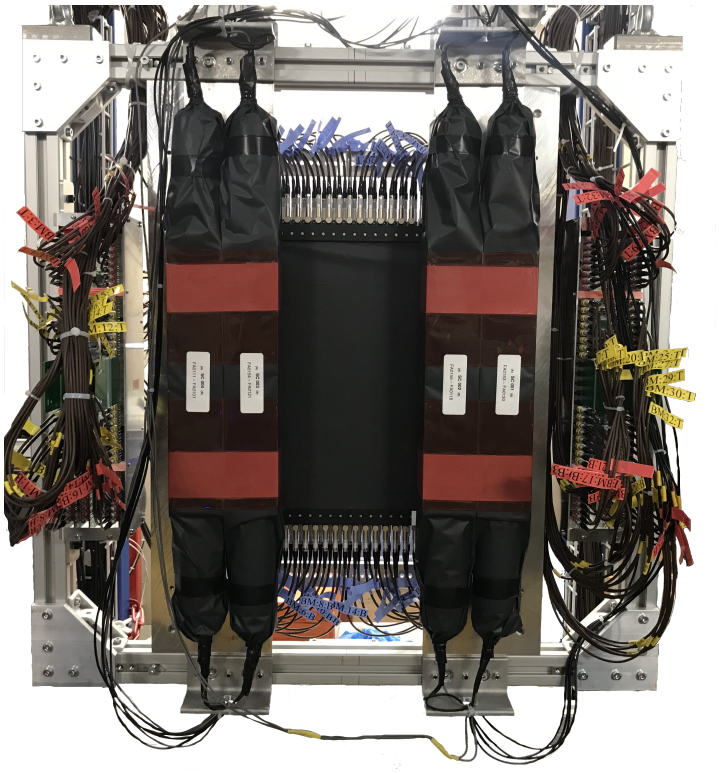

Figure 2.8: Photo of the beam monitor for MUSE.

The vacuum chamber resides at the center of the MUSE apparatus, as shown in figure 2.4, and houses the target ladder and the Beam Focusing Monitor (BFM). Due to my extensive involvement with the target system, full details of the components of the target system, including the BFM and the Target Chamber Post Vetos (TCPVs), are described in chapter 3.

After the vacuum chamber, the next detector in the beam line is the Beam Monitor (BM), shown in figure 2.8, which provides flux determination of particles downstream of the target, as well as time of flight (TOF) information using timing information from both the BM and the BH. This allows us to see on an event-by-event basis when particles are not scattering in the target and/or are decaying in flight within the MUSE set up. Ideally, if a particle scatters off the target, there will be no particle detected in the BM, so it is also used to limit trigger rate by rejecting background events where a particle is seen in the BM. This especially pertains to background created by Møller and Bhabha scattering.

The BM is made up of a central scintillator with two planes, surrounded by four larger outer detector bars. The central scintillator planes contain 16 paddles each that are 300 mm long, 12 mm wide, and 33 mm thick. The two planes are therefore offset by 6 mm, which lessens the chance of a particle traveling in between bars for both planes. The four outer

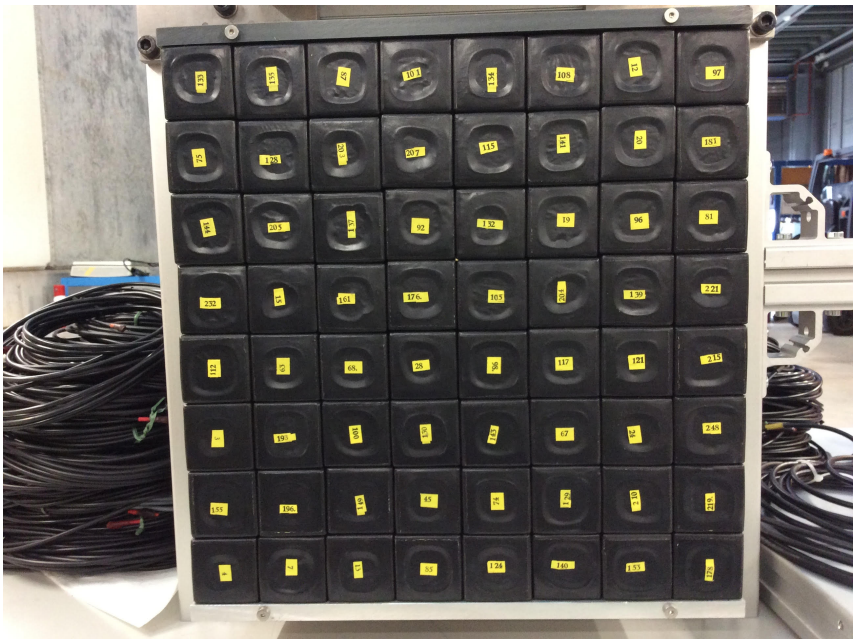

Figure 2.9: Photo of the calorimeter for MUSE before being installed on the platform; photo provided by Tiko Rostomayan.

bars, two on each side of the scintillator planes, are larger bars with dimensions of 30 cm long by 6 cm wide and 6 cm thick, which are read out by PMTs.

The final beam line detector is the photon calorimeter, which is installed at the farthest downstream point of the MUSE set up. The calorimeter is made up of 64 lead-glass blocks arranged in an 8×8 square; each block is 4 cm wide, 4 cm tall, and 30 cm long. The 4 cm by 4 cm square is oriented perpendicular to the beam's travel, and it can be seen in figure 2.9. Each block in the calorimeter is individually connected to a PMT and its light output is read out separately.

The calorimeter vetos photons that radiate from the initial-state Bremsstrahlung effect, which produces high-energy forward-scattered photons. Vetoing these events through the detection of the high-energy photons will allow MUSE to limit the radiative corrections that need to be considered in the electron-proton and muon-proton scattering measurement; radiative corrections are discussed further in section 5.3. More technical information about the photon calorimeter's design, construction, and performance can be found in Ref. [44].

2.2.2 Scattering Detectors

In order to reconstruct scattering events including the proper identification of particles involved, two scattering detectors are employed by MUSE to collect the necessary information for this comprehensive reconstruction: the STT and the SPS.

Figure 2.10: Photo of the STT detector while it is being repaired outside of the MUSE platform. The image is looking in the beam direction, and the straws shown are closest to the vacuum chamber in the detector set up.

For particles that scatter off the target and exit the vacuum chamber through the two large exit windows, the STT is stationed on either side of the vacuum chamber. The STT is a tracking detector with four chambers that follows the design from the PANDA experiment [45], and has two symmetric chambers on each side of the vacuum chamber. On each side, one chamber contains 60-cm long straws and the other has 90-cm long straws, in order to cover the desired scattering angle range of MUSE. Figure 2.10 shows an inner view of the 60-cm chambers, which are directly next to the target in the experimental set up. Each chamber has ten planes of straws, for which five are horizontally oriented and five are vertically oriented. All forty planes have a total of 2,850 straws, which are filled with an Ar and CO_2 mixture with a ratio of 90:10 and have a wire down the center of each that carries a voltage of 1800 V during operation.

The STT provides information to reconstruct tracks of scattered particles by fitting groups of hits in the detector. The fitting requires several hits that pass a chi-squared threshold for goodness of fitting. This allows good tracks to be formed, and noise and background to be filtered out.

The final detector that is furthest downstream for scattered particles is the SPS, which has two walls of scintillators that are symmetric on each side of the target chamber; one set of walls is shown in figure 2.11. The front walls each contain 18 120-cm long bars, and the

Figure 2.11: Photo of one set of walls of the SPS detector used for collecting timing and position information of scattered particles. Each side of the detector set up has two walls: a smaller front wall and a larger back wall.

back walls each contain 28 220-cm long bars, which allows the SPS to cover the area needed to reach MUSE's desired angle coverage (shown in table 2.1).

The SPS collects precise timing and coordinate information for scattered particles, which are used in conjunction with the position and timing from the BH to calculate time of flight, path length, and determine the species that participated in an event's scattering event. It also allows us to determine whether or not a particle decayed before or after scattering and subsequently remove these decay events.

2.3 Trigger and Data Acquisition for MUSE

All of the detectors in the MUSE set up contribute individual information to collaborate on the event reconstruction for scattering events of interest, and the intake and processing of all these signals is handled by the DAQ system.

2.3.1 DAQ

The DAQ for MUSE reads out the event data, the detector signals, and the timing and size information of the signals from each detector for each event. The control software for the

DAQ system is called MIDAS, which was developed by Stefan Ritt at PSI, in collaboration with TRIUMF in Canada. The DAQ system collects timing and position information and delivers it ultimately to two places: the master trigger, for the decision-making around accepting events, and the TRB that brings the information to the DAQ in a consolidated format for each event.

The BH, GEMs, veto, TCPV, BM, STT and SPS all send information to the DAQ, but only the BH, veto, TCPV, BM, and SPS also send information to the trigger. The BH and BM both are required to report high-precision timing information, so the readout for these detectors are amplified and sent to a Mesytec Constant Fraction Discriminator (MCFD), which then sends the analog signal to a LVDS splitter. This splitter sends the discriminated output to two separate TRBs: one for the master trigger decision-making, and one that sends the information to the DAQ. A channel's block diagram for this readout process is shown in figure 2.12.

The veto's readout scheme is very similar to the BH, however, because precise timing is not required from the veto to the same degree as the BH, the signal is not amplified and instead sent straight to the MCFD, where it is then sent on, split, and delivers information to both the trigger and the DAQ. While the SPS also reports information to both the trigger and DAQ, its readout uses PaDIWa discriminators, which digitize the signals from the SPS bars and send them onto the splitter, where information is then delivered to the trigger and DAQ.

The GEMs and STTs are sending information to just the DAQ and not the trigger system; the GEMs are read out using four APV25 Analog-to-Digital Converters (ADCs) per GEM plane to accommodate the 500 readout channels each plane has. These ADCs then send the signal to a Multi-Purpose Digitizer (MPD) board, which digitizes and sends the information to the DAQ. The STT, instead of using APV25s, is read out through first, a HV readout card designed specifically for MUSE, and then, a PASTREC card (originally designed for the straw tubes in the PANDA experiment [45]). Each plane of straws has its own PASTREC card, which sends the signal to the TRBs that communicate with and package information for the DAQ.

The DAQ has an online GUI that shows the event collection in live time and acts as a base of operation for the monitoring and data-taking. This consolidates all of the information about where the signal digitization is happening for each detector's output, and it shows the event synchronization done by the DAQ to package timing information by event across all detectors, as seen in figure 2.13.

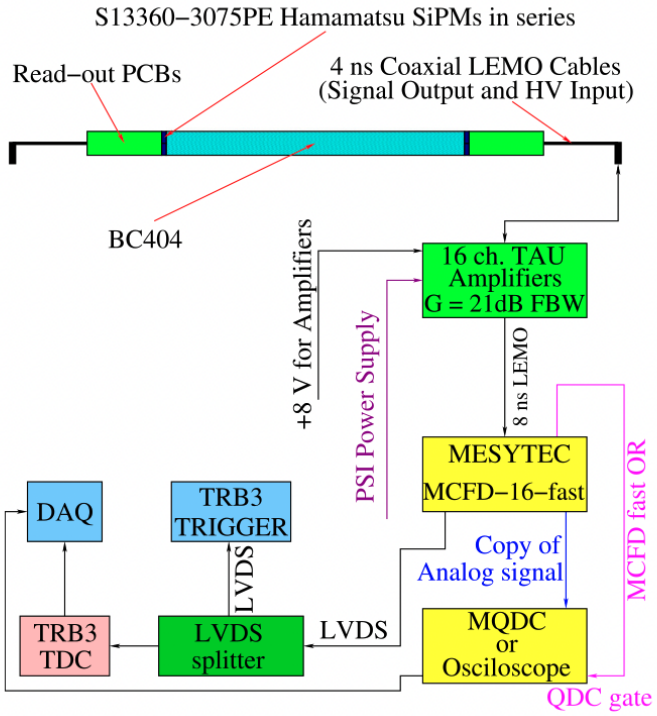

Figure 2.12: Block diagram for a single BH channel (also accurate for a BFM or BM channel), from Ref [4]. The amplifier that reads out the SiPMs is specially built by the Tel Aviv University group, and the analog signal is copied and sent to the QDC for digitization.

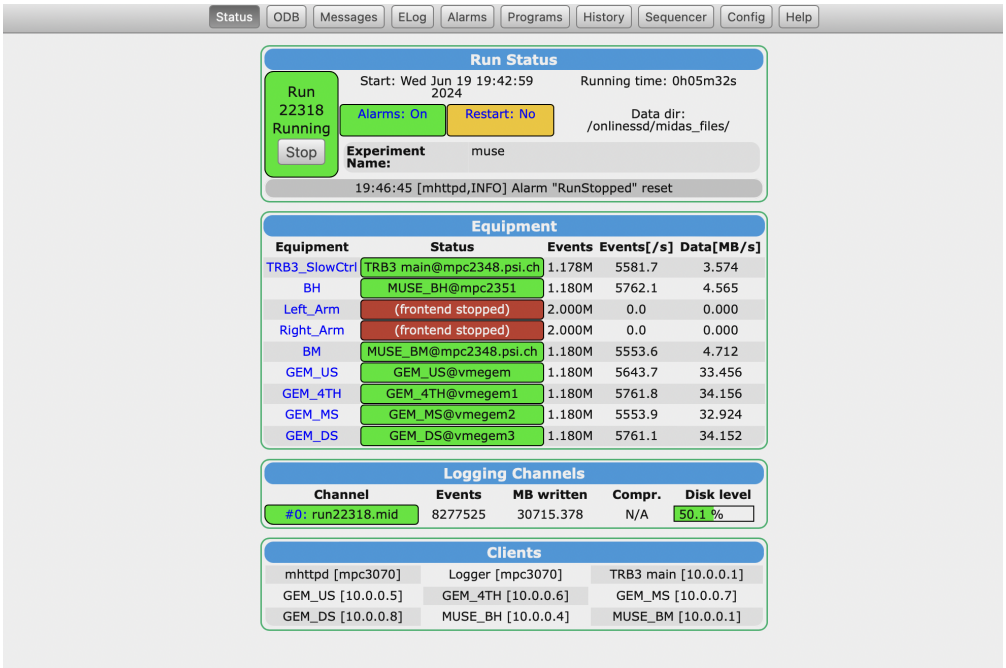

Figure 2.13: Screenshot of the online GUI used to operate and monitor the DAQ for MUSE data collection. The Left Arm and Right Arm each respectively control that side's STT and SPS detector signal collection and digitization, and the TRB3 SlowCtrl is the component that communicates with all detectors and delivers the information to the DAQ ultimately.

2.3.2 Trigger and Trigger Logic

With PiM1's mixed beam, the trigger and trigger logic for MUSE prioritize collecting electron-proton and muon-proton scattering events, while suppressing pion-proton scattering events and filtering out particle decays or non-scattering particles. To accomplish this, the trigger is comprised of two levels: the first level takes input directly from the detectors, and the second level ANDs and ORs these inputs together to ultimately determine whether or not an event is accepted by the trigger.

The first level of the trigger is comprised of the following main inputs that are components used in the higher level decision-making:

1. PID: The input from the BH and the accelerator RF allows us to determine the species of a detected particle, which we can use to focus on electron and muons while preventing pions from triggering events.

2. SPS: The input from the SPS provides timing information for a particle and allows us to confirm that a particle scattered, so we are able to require that the SPS sees a signal in order to trigger on an event.

3. Veto: The veto before the vacuum chamber, the TCPVs, and the BM all provide input that a particle is not scattering off the target in the desired angle range, and we can use this to remove cases that will not be able to construct a scattering event.

4. BUSY: To prevent the trigger and DAQ from becoming overwhelmed, a BUSY signal is produced by BH, BM, GEMs, and SPS when the system cannot accept more data because it is working on consolidating and sending information of a triggered event to the DAQ.

The second level of the trigger, also known as the master trigger, takes these inputs and determines if the conditions for a scattering event using the logic Trigger = (e OR μ) AND (not π) AND (SPS - scattered) AND (not (BM OR TCPV OR veto)). This trigger logic allows us to suppress unwanted background events while having the basic necessary components to be able to reconstruct events of interest. Further discussion of the trigger and its reconstruction in the analysis process is in section 4.2.2.

2.3.3 Data Taking: Summary and Plans

MUSE aims to have a relative cross section measurement with a precision better than 1%, for which a large number of scattering events is needed. MUSE began commissioning the full integrated detector systems for data-taking in 2018, with the first preliminary scattering data collected in the summer and fall beam times in 2019. The data analysis performed on the 2019 data allowed us to examine and confirm that our detectors had the required resolution for the cross section measurement precision we aim for, and so it allowed us to prepare for the following years of data-taking.

During the 2021 beam time, we prioritized data collection at $\pm$115 MeV/c (summarized in tables 2.3 and 2.4) because the dominating presence of electrons at this momentum provides ideal circumstances to perform time-walk corrections and adjust time alignment for the scintillating paddles of the BH and SPS, so that the timing information we extract is helping us accurately reconstruct scattering events of interest.

For the 2022 beam time, plans for data-taking expanded to include scattering and calibration data at all three momenta and both polarities, with the goal to understand our yield of good scattering events and predict the statistics needed to achieve the total desired number of events for cross section calculation. The data collection was spread evenly across the momentum and polarity configurations, as can be seen in table 2.5.

During the two beam times for 2023, data was again collected at all three momenta for both polarities, and am emphasis was placed on collecting $\pm$210 MeV/c data in order to look more closely at handling muon decay events within the MUSE experimental set up. In

Production Scattering Data +115 MeV/c			
Elog Entry	**Runs**	**Comments**	**Bad Runs**
2120	10524-10555	production data with test runs at end	10549-10555
2123	10556-10586	production data	10559, 10560, 10561
2125	10587-10600	production data	10592, 10593
2127	10601-10612	prod. data; GEMs changed to 1 sample in middle, noisy STT's most of runs	10608
2131	10613-10629	prod. data	n/a
2133	10630-10640	prod. data	10630, 10633, 10634
2137	10641-10652	prod. data - ALL BAD; STT HV was off for all runs	all
2138	10653-10669	prod. data	10653,
2139	10670-10695	prod. data and new trigger	10671-10673, 10682-10695
2144	10696-10700, 10712-10715	prod data and FS-13 adjustment	10696, 10697, 10699, 10713, 10714
2146	10716-10727	prod data	n/a
2147	10728-10740	prod data	10729
2151	10741-10744	prod data	n/a
2155	10770-10785	prod data	n/a
2156	10786-10792	prod data - right before thanksgiving maintenance	10790
2276	11444-11455	prod data	n/a
2277	11456-11469	prod data	11459

Table 2.3: Summary of the (+)115 MeV/c data collected in 2021. Each run number for a "good run" (no known detector or electronic issues or interruptions) signifies 2 million events collected at a time. This number of events was decided upon to keep the resulting data files at a manageable size when performing analysis.

Production Scattering Data -115 MeV/c			
Elog Entry	**Runs**	**Comments**	**Bad Runs**
2175	10887-10892	prod. data (first one, plus emergence of PID issues)	n/a
2176	10893-10905	prod. data	10893, 10898, 10899, 10902-10904
2178	10906-10915	prod. data	10907, 10908
2179	10916-10931	prod. data - very few good runs	10916-10926
2180	10932-10957	prod data, lots of JUNK runs - note, all scattering runs before this had 12x12 in	10932, 10937, 10938, 10948-10952, 10955, 10956
2184	10964-10968	prod data all empty cell	n/a
2186	10969	prod data 1 empty cell run, accelerator shut off	n/a
2187	10971-10980	prod data	10971-10975
2192	10987-10988	prod data with new prescale factor	n/a
2194	10989-10999	prod data- all empty cell	1989, 10992-10994, 10996, 10998
2201	11014-11015	prod. data - empty cell	n/a
2204	11016-11019	prod. data - empty cell	n/a
2205	11020-11028	prod data - empty cell	11021,
2209	11029-11038	prod data - empty cell	n/a
2210	11039-11046	prod data - empty cell	n/a
2211	11047-11051	prod data - empty cell	11048
2214	11052-11064	prod data - empty cell	11057, 11059, 11060, 11063
2215	11065-11075	prod data - empty cell	11065, 11073
2218	11076-11084	prod data - empty cell	11076, 11080-11083
2220	11104-11108	prod data - LH2	11106
2224	11108-11118	prod data - LH2	11112
2225	11119-11127	prod data - LH2	11119, 11120, 11122-11124
2227	11128-11134	prod data - lH2; , but 11130 is +115	n/a
2228	11134-11144	prod data -LH2	11142
2229	11144-11154	prod data- LH2	n/a
2234	11163-11172	prod data- LH2 - likely all bad bc target went to shut down mode	ALL
2238	11185-11202	prod data - LH2	11185, 11187-11197, 11202
2242	11203-11217	prod data - LH2	11204, 11206, 11207, 11217
2245	11218-11225	prod data - LH2	11218, 11219, 11225
2248	11226-11234	prod data - LH2	n/a
2250	11235-11247	prod data - LH2	11236, 11245
2252	11248-11254	prod data - LH2	11251, 11252
2254	11255-11266	prod data - LH2	11259, 11265
2257	11267-11280	prod data - LH2	11273, 11274, 11276-11280
2266	11367-11379	prod data	n/a
2267	11380-11388	prod data	11382
2268	11389-11401	prod data	n/a
2269	11402-11412	prod data	11408
2272	11413-11420	prod data	11413
2273	11421-11433	prod data	11422, 11433
2274	11434-11443	prod data	11434

Table 2.4: Summary of the (-)115 MeV/c data taken in 2021.

2022 Run Plan: Data-taking Summary						
Momentum	**(+)115**	**(-)115**	**(+)160**	**(-)160**	**(+)210**	**(-)210**
LH2 scattering	13987-13991 13998-14017 14019, 14021, 14023 14029-14030 14032-14056 14060-14068 14070-14075 14077-14094	14354-14369 14374-14375 14377-14383 14495-14499 14505-14520 14529, 14531-14572	14714-14745 14782-14801 14803-14805 14879-14886 14889-14894	14958-14985 15033-15056 15102-15123 15186-15191 15267-15268	15324-15335 15337-15342 15389-15392 15394 15413-15415 15419, 15423 15468-15469 15471-15474 15477-15482 15688-15715	15490-15502 15504-15511 15572-15576 15581-15589 15593-15594 15597-15600
Empty cell scattering	14095-14114 14177-14185 14187-14204 14206-14208 14217-14224 14261-14277	14384-14386 14449, 14456, 14459-14469 14471-14489 14573-14574 14576-14580 14631-14638 15672, 15675-15680	14746-14747 14762-14781 14806-14814 14825-14827 14829, 14831, 14832 14833-14838 14840-14853 14912-14920	15001-15026 15062-15064 15087-15101 15125-15138 15269-15272	15343-15349 15355-15357 15359-15360 15366, 15370 15373-15375 15378-15379 15457-15461 15463-15467 15681-15687 15716-15725 15730-15733 15812-15820	15540-15545 15547-15548 15550-15555 15601-15602 15604-15620
Carbon scattering	14278-14297 14698-14705	14323-14326 14328-14334 14338-14340 14342-14343 14349-14352 14683-14697	14921-14927 14931-14938 14940-14942	15166-15180 15185 15264-15266	15446-15450 15483-15485 15488 15734-15738	15621-15628
Empty space scattering	14313-14317	14318-14322	14944-14945 14951-14952	15144-15148 15665	15424-15426 15429-15434	15567-15571
Pions (LH2)	n/a	n/a	14865 14867-14870	15057-15061	n/a	n/a
Pions (empty cell)	n/a	n/a	14904-14911	15149-15151 15162-15165	n/a	n/a
No vetos	14301-14305	14494	14854-14859	15027-15032 15065-15066	15629-15632 15635-15637	15516-15517 15520-15523
Positron efficiency	n/a	n/a	14871-14874 14877	10567-10571	15638-15642	15524-15525 15529-15531
SPS efficiency	14307-14309 14311-14312	14500-14504	148460-14864	10572 10583-10586 15149-15142	15643 15646-15647 15649-15652, 15655	15532-15534 15538-15539
Collimator Scan	15295-15303 (empty cell) 15668-15672	15074-15082 (LH2)	15656-15663	14989-14996 14999-15000	15435-15440 15442-15445	15556-15565

Table 2.5: Summary of the production data taken in 2022 that was not interrupted or affected by any detector and electronic issues.

Category	Total Events (in millions)	Total Goal (in millions)	Ratio
(+)210 LH2 Scattering	307.663	564	0.55
(+)210 Empty Cell Scattering	281.661	378	0.75
(+)210 Rod Target Scattering	49.957	20	2.50
(+)210 Empty Space Scattering	0	64	0.00
(+)210 Unfilled LH2 Cell Scattering	160.87	40	4.02
(+)210 LH2 No Vetos	37.9	64	0.59
(+)210 LH2 SPS + Positron Efficiency	70	64	1.09
(+)210 Empty Cell TOF	12	12	1.00
(+)210 Empty Cell Collimator Scan	20	10	2.00

Table 2.6: Summary of the (+)210 MeV/c data taken in 2023, from both the summer and fall beam times.

addition to taking shift during beam time, part of my contribution toward data-taking has been constructing and expanding a database that summarizes and organizes the data taken each year. Additionally, I helped create and modify the data-taking plan through the 2022 and 2023 beam times depending on the troubleshooting or adjustments needed to achieve our desired number of events. From the database, tables 2.6 and 2.7 show the summary for the ±210 MeV/c data collected in 2023.

From 2021 through 2023, the amount of data MUSE collected drastically increased, and as a result, we changed our structure for cataloguing the collected data, so that it was convenient to parse and access data with the desired parameters. MUSE plans to take data for two more years at PSI, with beam times in 2024 and 2025. Using our estimation of collected scattering events by particle type, as shown in figure 2.8, we are currently working on a data collection plan for 2024 and 2025 that satisfies our events needed for a sub-percent-level precision cross section measurement.

Category	Total Events (in millions)	Total Goal (in millions)	Ratio
(-)210 LH2 Scattering	674.43	564	1.20
(-)210 Empty Cell Scattering	498.83	378	1.32
(-)210 Rod Target Scattering	44.749	20	2.24
(-)210 Empty Space Scattering	65.3	64	1.02
(-)210 Unfilled LH2 Cell Scattering	24.6	20	1.23
(-)210 LH2 No Vetos	79.8	64	1.25
(-)210 LH2 SPS + Positron Efficiency	80.6	64	1.26
(-)210 Empty Cell TOF	22	12	1.83
(-)210 Empty Cell Collimator Scan	52	10	5.20

Table 2.7: Summary of the (-)210 MeV/c data taken in 2023, from both the summer and fall beam times.

Momentum	Category	Total	Beam Electrons (millions)	Beam Muons (millions)	Beam Pions (millions)
(+)115	Scattering	121.04	114.988	1.2104	4.8416
(+)115	Scattering	80.24	76.228	0.8024	3.2096
(+)115	Scattering	21.76	20.672	0.2176	0.8704
(+)115	Scattering	6.8	6.46	0.068	0.272
(+)115	Pions	0	0	0	0
(+)115	No Vetos	6.8	6.46	0.068	0.272
(+)115	SPS Efficiency	6.8	6.46	0.068	0.272
(+)115	Collimator Scan	5.44	5.168	0.0544	0.2176
(-)115	Scattering	108.8	106.624	1.088	1.088
(-)115	Scattering	77.52	75.9696	0.7752	0.7752
(-)115	Scattering	21.76	21.3248	0.2176	0.2176
(-)115	Scattering	6.8	6.664	0.068	0.068
(-)115	Pions	0	0	0	0
(-)115	No Vetos	6.8	6.664	0.068	0.068
(-)115	SPS Efficiency	6.8	6.664	0.068	0.068
(-)115	Collimator Scan	5.44	5.3312	0.0544	0.0544
(+)160	Scattering	108.8	59.84	11.968	36.992
(+)160	Scattering	77.52	42.636	8.5272	26.3568
(+)160	Scattering	21.76	11.968	2.3936	7.3984
(+)160	Scattering	6.8	3.74	0.748	2.312
(+)160	Pions	6.8	3.74	0.748	2.312
(+)160	Pions	6.8	3.74	0.748	2.312
(+)160	No Vetos	6.8	3.74	0.748	2.312
(+)160	Positron Efficiency	6.8	3.74	0.748	2.312
(+)160	SPS Efficiency	6.8	3.74	0.748	2.312
(+)160	Collimator Scan	5.44	2.992	0.5984	1.8496
(-)160	Scattering	108.8	95.744	4.352	8.704
(-)160	Scattering	77.52	68.2176	3.1008	6.2016
(-)160	Scattering	21.76	19.1488	0.8704	1.7408
(-)160	Scattering	6.8	5.984	0.272	0.544
(-)160	Pions	6.8	5.984	0.272	0.544
(-)160	Pions	6.8	5.984	0.272	0.544
(-)160	No Vetos	6.8	5.984	0.272	0.544
(-)160	Positron Efficiency	6.8	5.984	0.272	0.544
(-)160	SPS Efficiency	6.8	5.984	0.272	0.544
(-)160	Collimator Scan	5.44	4.7872	0.2176	0.4352
(+)210	Scattering	107.95	12.954	7.5565	87.4395
(+)210	Scattering	74.8	8.976	5.236	60.588
(+)210	Scattering	21.25	2.55	1.4875	17.2125
(+)210	Scattering	8.5	1.02	0.595	6.885
(+)210	Pions	0	0	0	0
(+)210	Pions	0	0	0	0
(+)210	No Vetos	8.5	1.02	0.595	6.885
(+)210	Positron Efficiency	8.5	1.02	0.595	6.885
(+)210	SPS Efficiency	8.5	1.02	0.595	6.885
(+)210	Collimator Scan	8.5	1.02	0.595	6.885
(-)210	Scattering	61.2	28.152	0.612	32.436
(-)210	Scattering	44.2	20.332	0.442	23.426
(-)210	Scattering	12.75	5.865	0.1275	6.7575
(-)210	Scattering	8.5	3.91	0.085	4.505
(-)210	Pions	0	0	0	0
(-)210	Pions	0	0	0	0
(-)210	No Vetos	8.5	3.91	0.085	4.505
(-)210	Positron Efficiency	8.5	3.91	0.085	4.505
(-)210	SPS Efficiency	8.5	3.91	0.085	4.505
(-)210	Collimator Scan	8.5	3.91	0.085	4.505

Table 2.8: Summary of scattering events by particle species, from the data collected in 2022.

CHAPTER 3

Liquid Hydrogen Target

The collaborating group at the University of Michigan is responsible for the construction, maintenance, and operation of the liquid hydrogen target [46] that is employed at the heart of the MUSE experimental setup. In collaboration with the target, vacuum, safety, and engineering groups at PSI during construction, testing, and operation, as well as George Washington University during initial conception, and a private company, Creare, for detailed design and engineering, the target system was designed and constructed across 2017-2018 and was first commissioned at PSI in December 2018.

3.1 Design and Construction

When designing the system for the liquid hydrogen target, many factors played a role in the constraints of the target system, including but not limited to:

- The vacuum chamber entrance window and target center position must be 1.5 m above the floor of the PiM1 area.
- The target system must have a maximum outer diameter of 49 cm.
- The vacuum chamber must include four targets: LH_2, GH_2, a solid target, and an empty space.
- LH_2 target must have an outer diameter of 6 cm, and a height of 8 cm plus end caps.
- There shall be one heater at the bottom of each cell.
- There shall be one temperature sensor at the bottom of each cell.
- There shall be redundant heaters and temperature sensors on the copper condenser.

The full list of requirements can be found in Appendix A.

Operating in the context of these constraints for the target system, the Lorenzon group at the University of Michigan and Creare constructed a system that includes a target ladder with five specific targets and vertical mobility in and out of the beam, a cryocooler and condenser used to liquefy hydrogen into the designated cell in the target ladder, and a vacuum chamber that encases the ladder and allows for its full mobility. A gas system for filling and venting the LH_2 cell, a LabVIEW slow control system used to operate and monitor all constituents of the system, and a camera system for monitoring the target ladder inside the vacuum chamber were also all developed as components of the target system.

3.1.1 Target Ladder

The target ladder itself is made of two cells, a solid target, and a beam focusing monitor combined into a ladder capable of vertical movement within the vacuum chamber that contains it. The ladder can be positioned at multiple different targets that all have intentional purposes in data collection and analysis for MUSE. The first target position is the LH_2 position, which is the cell that is filled with liquid hydrogen. The cell is a cylinder with a diameter of 6 cm and a height of 13.7 cm, including the copper end caps. The walls of the cylinder are made of Kapton sheets that are 25 μm thick, and the Kapton is wrapped four times in a cylinder and glued using a mixture of Stycast 1266 A and B epoxies to create walls that are 120 μm thick. The end caps that attach to the Kapton cylinder to create the cell are made of copper and also have a diameter of 6 cm; they have a lip that extends 1 cm into the cell at each end. Multiple strips of Kapton are glued on top of the Kapton cell over the lip of the end cap to strengthen the seal created. Additionally, two rectangular pieces of Kapton are glued on top of this joint to further

Figure 3.1: Photo of the target ladder wrapped in superinsulation before being craned into the vacuum chamber in PiM1 at PSI.

reinforce the strength of the seal with glue. The LH_2 cell has the capacity for 280 mL of LH_2.

Below the LH_2 cell on the ladder is an identical cell with the same dimensions and materials that remains unfilled, in order to provide precise background data for subtraction when analysing the scattering data. The vertical separation between the full and empty cells is 150.5 mm. The two cells, as well as the condenser, are wrapped in ten layers of aluminized Mylar, also called superinsulation (shown in figure 3.1), which lowers the radiation heat load from the vacuum chamber on the cells from 1.4W to 130 mW.

The third target on the ladder was originally a solid target consisting of two rectangles, each 3 cm by 6 cm and 1 mm thick, of a carbon and CH_2 target that are stacked on top of one another to form a 6 cm by 6 cm square. The split target was used in the 2019 summer and fall beam times, with the goal of being able to subtract the carbon scattering data from the CH_2 scattering data to have hydrogen scattering data to compare to the liquid hydrogen scattering. This split solid target was later replaced by a full carbon target, consisting of a 6 cm by 6 cm square of carbon, also 1 mm thick, to fit in the previous space. The full carbon solid target was used in the 2020, 2021, and 2022 beam times, with the purpose of using the carbon scattering data to fine-tune and confirm precise event reconstruction from a vertex on the solid target. Most recently, the solid carbon target was replaced with a 1 mm thick rod target that was constructed with a 6 cm by 6 cm frame to fit in the place of the square frame that held the solid target. The rod target was used in the 2023 summer and fall beam times, and a schematic view of all three solid targets in the ladder can be seen in figure 3.2.

The BFM is located below the solid target and is used for identifying characteristics of the beam spot at the target such as its size and how well it is focused in the scattering region. The BFM consists of three scintillators, each 2 mm by 2 mm by 2 mm, that are each connected to Silicon Photomultipliers (SiPMs) through light guides that route up the ladder and out the top of the vacuum chamber. A voltage of 50 V is applied to each BFM scintillator, and this is only used when the target does not contain liquid hydrogen. The final target position of the ladder is the empty space, and it is the position at which the target ladder is moved above the beam so that the incoming particles do not scatter off any of the physical targets on the ladder. Another component of the target ladder is an optical bull's-eye that faces in the $-y$ direction; this bull's-eye is not a target position for data taking, but instead it is used to observe/record the offsets of the different ladder positions in the x and z directions as the ladder moves vertically within the vacuum chamber.

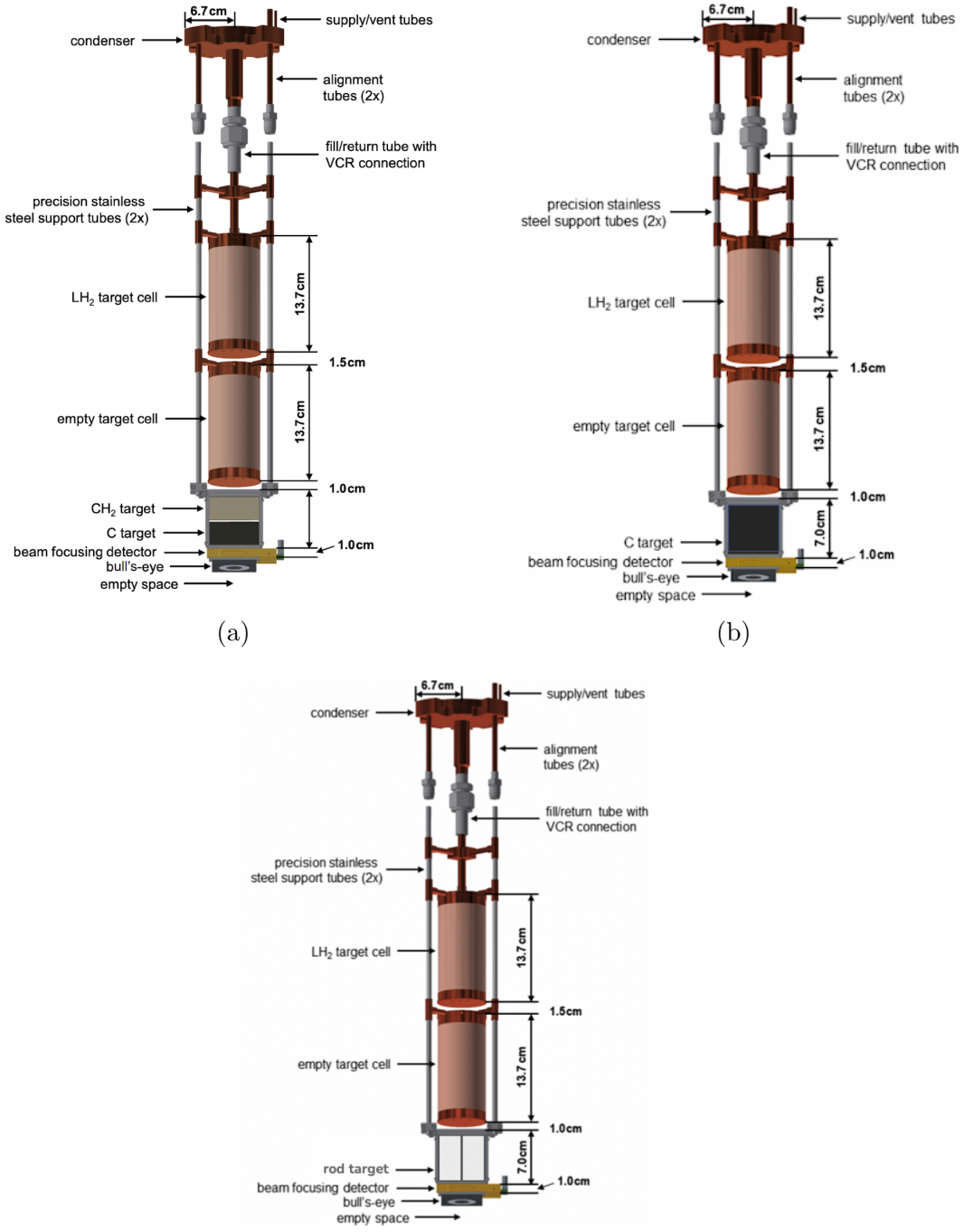

Figure 3.2: Target ladder with the three different solid targets used. Panel (a) shows the first target used, the split target with both C and CH_2, panel (b) shows the solid C target, and panel (c) shows the rod target, which is currently being used in the target ladder.

3.1.2 Vacuum chamber and TCPV

The vacuum chamber, shown in figure 3.3, that houses the target ladder has a trapezoidal shape, which corresponds to the large scattering angle coverage MUSE collects data for. The side exit windows cover the angle range $20^\circ \leq \theta \leq 100^\circ$ on each side, with the polar angle coverage $\phi = \pm 45^\circ$ [46]. On the upstream side of the vacuum chamber, the beam entrance window has a 7-cm diameter, a clear aperture, and is made of aluminized Kapton. The full technical details of the vacuum chamber, as well as the rest of the target system, are reported in Ref. [46].

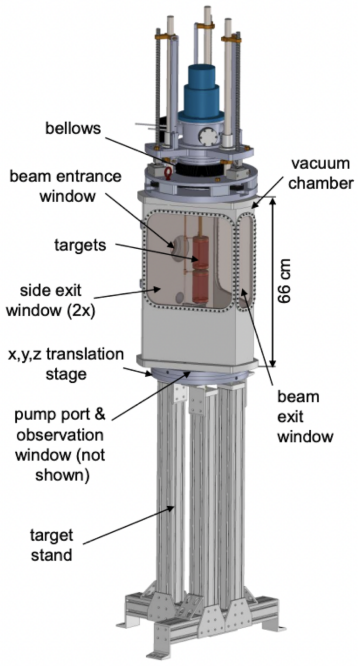

Figure 3.3: Schematic view of the vacuum chamber and stand with the target ladder inside the chamber.

For the scattering angles which contain the exit posts of the vacuum chamber, more than 90% of the detected events are from background scattering due to particles hitting these posts. As a result, the TCPVs were constructed and integrated into the target system's vacuum chamber in order to veto on these background events during data collection [47]. The TCPVs are comprised of two scintillator paddles that are 200 mm tall, 20.5 mm wide, and 4 mm thick and are mounted in the vacuum just upstream of the two vacuum chamber exit posts, perpendicular to the incoming beam. This detector was added to the target system in 2022 before the beam time, and it has since been commissioned, used, and upgraded for use of background vetoing during multiple beam times. The details of the TCPV construction and components can be found in Ref. [47].

3.1.3 LabVIEW Slow Control System, Camera System, and Target Monitoring

The target system is monitored and operated through a LabVIEW program written by Konrad Deiters (PSI) and controls every aspect of the system. We use the LabVIEW program to set and monitor the temperature of the cell, to operate the gas system to fill or purge the target cell with LH_2 or LNe_2, to vertically move the ladder and position different targets in the beam line, and to control and monitor the pressure inside the vacuum chamber. During data taking, the main screen of the slow control program plots the temperature, inlet and

outlet pressures, resistance of the level resistor, and power output of the heater to provide a full picture of the target's status at any given time. Figure 3.4 shows the slow control program during a cool down operation with LH_2, performed for the 2022 beam time.

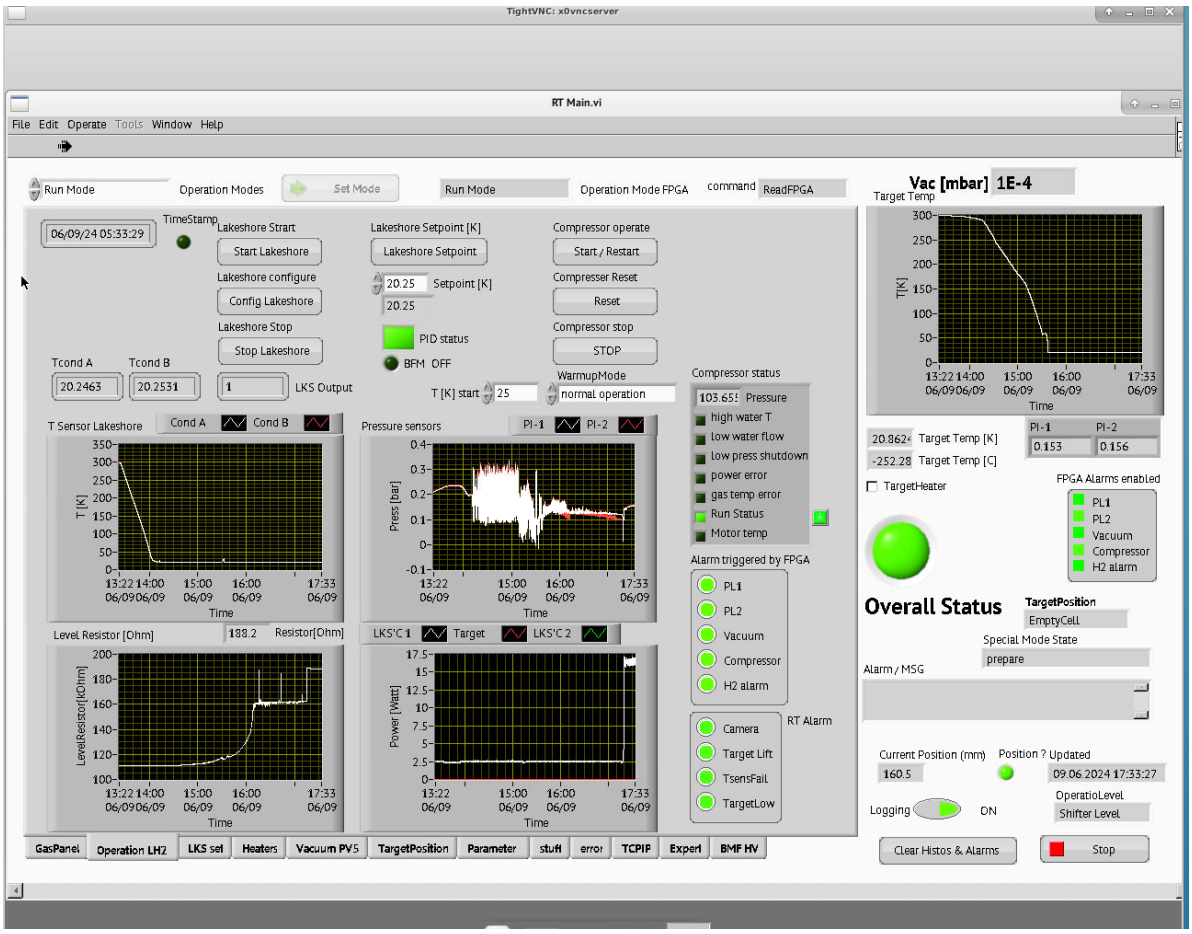

Figure 3.4: Screenshot of the LabVIEW slow control program that operates and monitors the target system. This was taken during a cool down with LH_2, which is why the temperature set point was at 20.25 K.

The slow control program was designed for use by target experts, so a separate monitoring page for the target was created and integrated into the MUSE-wide DAQ system by Jan Bernauer. This monitoring page, shown in figure 3.5, was designed for shift takers to be able to quickly and easily check the status of the target during data-taking, and it has explicit parameters for acceptable performance, as well as conditions under which a target expert should be called or consulted.

The camera system for the target was designed and built with the goal of being able to monitor the target ladder while it is inside the vacuum chamber during operation. It serves the purpose of both confirming the location of the ladder, using the known distances between

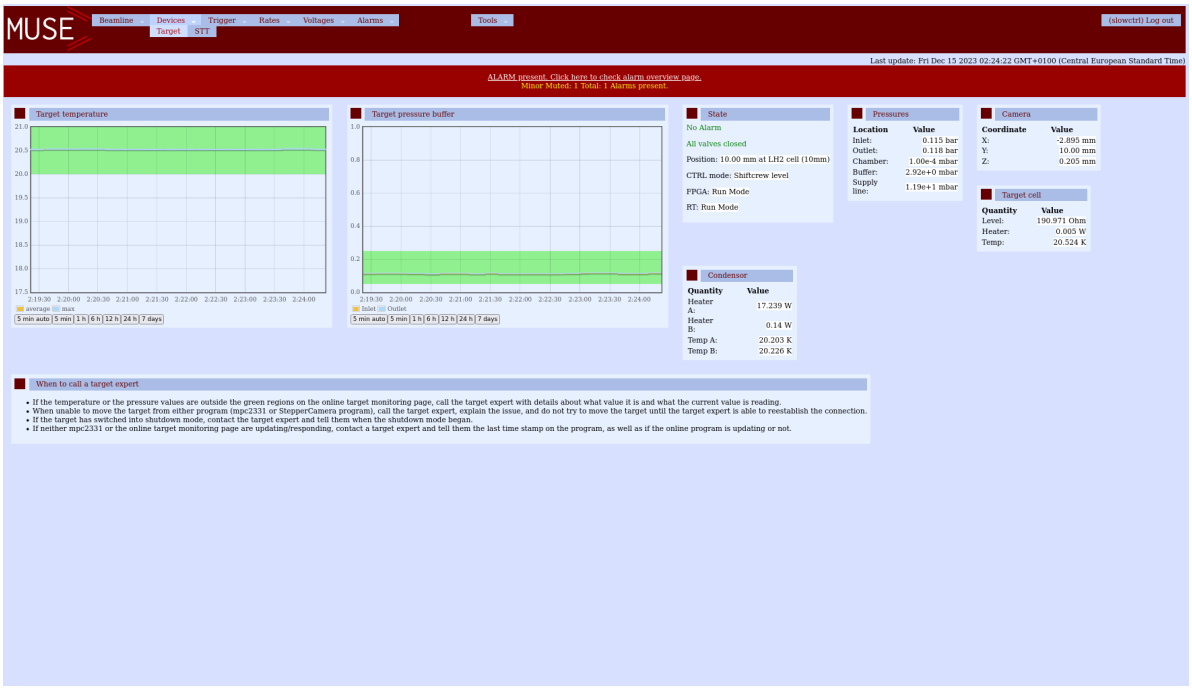

Figure 3.5: Screenshot of the target monitoring page made for shift takers to more easily watch the target during data taking. The temperature and pressure graphs both have green bands to represent the acceptable range of these parameters.

the camera and the bull's-eye at the bottom of the ladder, as well as to observe any potential shift of the target at beam height in the x or z direction during temperature and pressure changes in the vacuum chamber. The camera is located below the vacuum chamber at the pump port and observation window labeled in figure 3.3, and it looks in the $+y$ direction up at the target ladder's bull's-eye.

The software that originally interfaced with the camera and displayed the image of the ladder was written by an undergraduate Matthew Dimond in Python. This software was later rewritten and upgraded by Ievgen Lavrukhin in LabVIEW, which interfaced with the already existing target slow control system more easily.

3.2 Filling the Target with LH_2

The target ladder is connected to fill and exhaust lines for LH_2, which is cooled and condensed by the CH110-LT single-stage cryocooler in conjunction with the condenser. The condenser is comprised of two copper plates that are soldered together and are arranged such that the top plate has a series of copper fins that increase the surface area available for the gas condensing. The bottom plate has a concave cone-shaped surface that funnels the liquefied

hydrogen into the supply tube that takes it to the target cell. The condenser is attached to the coldhead of the cryocooler and has two heater circuits as well as two temperature sensors, for redundancy.

After pumping the vacuum chamber down, we use a Lakeshore temperature controller to set the goal temperature to 20.25 K, which the cell needs to reach before it can be filled with the liquefied hydrogen. This process of reaching 20.25 K takes approximately 75 minutes with the cooling power of the cryocooler, 25 W at 20 K. Once the system has reached 20.25 K, the setpoint on the temperature controller is adjusted to 20.65 K, and the cell begins to fill with hydrogen. The level resistor on the inside of the cell's top end cap will indicate when the cell fills with LH_2 by measuring a resistance of 188 Ω, jumping from around 160 Ω while the cell is filling, as shown in the bottom left plot in figure 3.4. Once this indication has occurred, we shut the pneumatic valves for the hydrogen supply line and carefully adjust the temperature to maintain the cell's pressure at about 1.1 bar. This pressure is maintained to prevent air from entering the cell while it is cooled down, in case of a leak in the cell.

3.3 Target Operation during Data Taking

The target system was first commissioned in December 2018, for a 72-hour test period to ensure all components were operating as expected. The commissioning was incredibly successful, and the target stabilized at 20.67 K with a standard deviation of 0.01 K. Since the initial commissioning of the target system, it has been operated for data-taking in 2012, 2021, 2022, and 2023; the full summary of beam time temperatures and stability can be found in table 3.1. It is important to note that when operating the target for MUSE, we maintain the target's stability by its temperature setpoint. As a result of this, the target's temperature remains extremely stable to a one-hundredth of a Kelvin or better, but the pressure of the hydrogen fill and exhaust lines would vary between 1.08 and 1.18 bar, depending on the temperature and humidity of the experimental hall.

For the 2019 beam time, the target was operated for five days - as shown in figure 3.6a - with a 100% up time (August 6-11, 2019). The step down just before hour 100 was due to a change in the temperature set point in the slow control system, and its temperature stability (adjusted for the set point change) is shown in figure 3.6b. Later that year, the target was operated for thirty days with a 97% up time (November 27 - December 23) to a similar stability level. The 2019 beam times were used mainly for commissioning detectors, as well as integrating and testing systems. The interruptions in the Fall 2019 beam time were due to brief communication freezes between the Lakeshore temperature controller and the target slow control program, during which the system continued to operate smoothly.

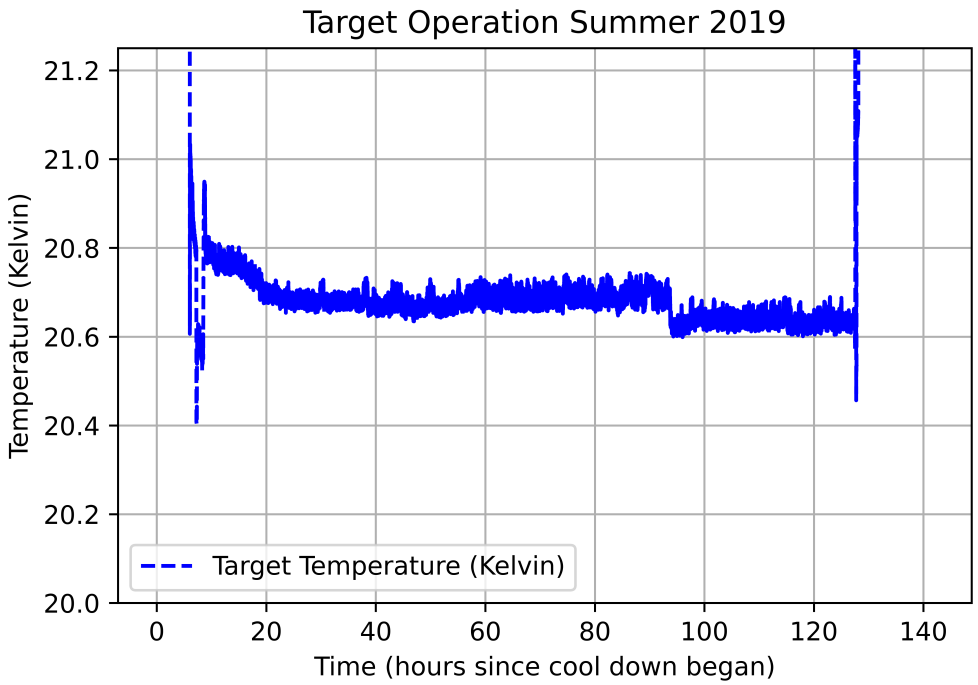

(a)

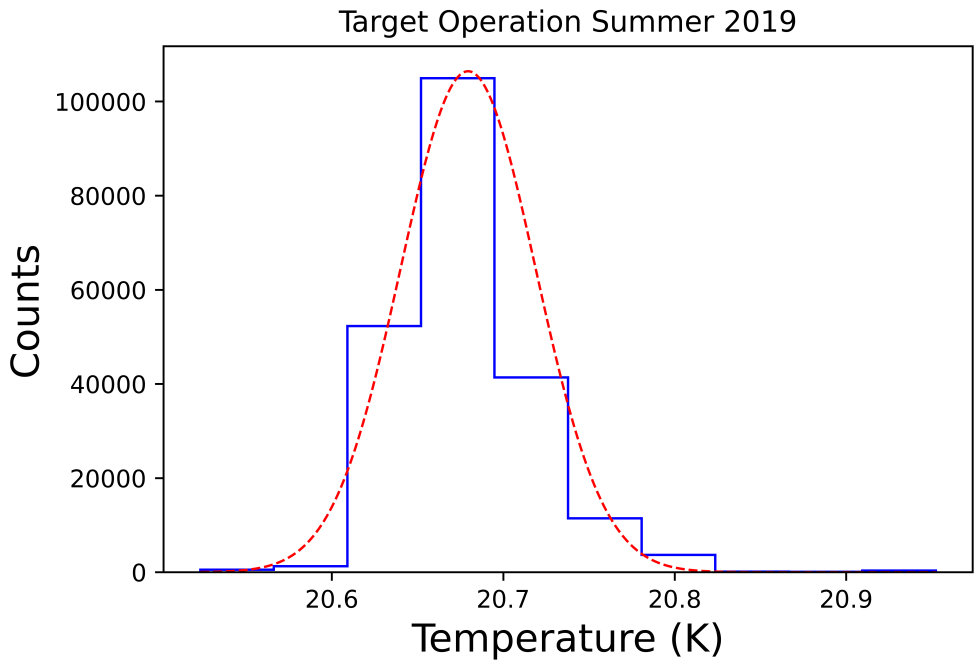

(b)

Figure 3.6: Target operation from August 6 - 11, 2019. Panel (a) shows the temperature trends for the Summer 2019 beam time, where the target was cooled down for 5 days. There were no interruptions to the operation of the target during this operation. Panel (b) shows the histogram of temperature data from the Summer 2019 beam time. The average temperature was 20.69 K, with a standard deviation of 0.015 K.

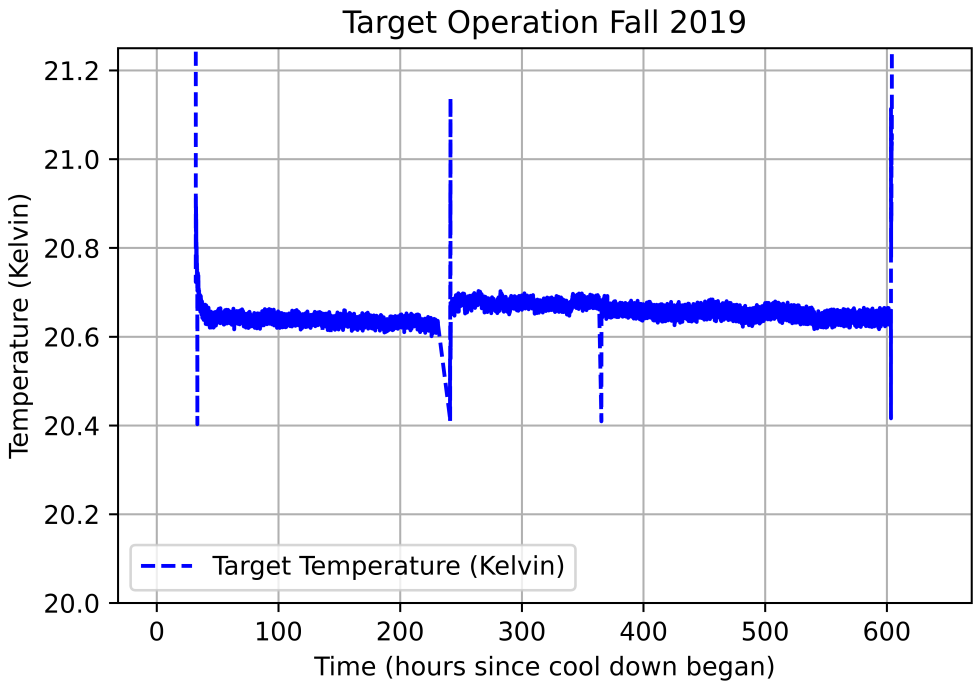

(a)

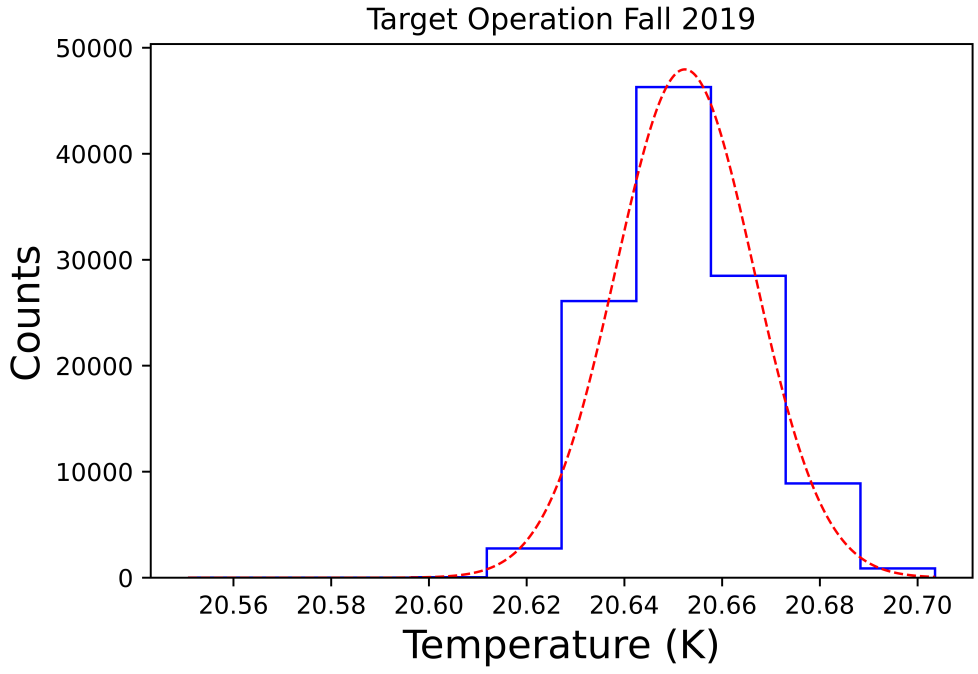

(b)

Figure 3.7: Target operation from November 27 - December 23, 2019. Panel (a) shows the temperature trend for the Fall 2019 beam time. The two brief interruptions were due to communication freezes between the LabVIEW program controlling the target and the temperature controller module. Panel (b) shows the histogram of the target's temperature data from the Fall 2019 beam time. This target mean temperature was 20.68 K, with a standard deviation of 0.01 K.

The temperature was set at a slightly different set point after the recoveries from each interruption, which is visible in figure 3.7a, and the average temperature shown in figure 3.7b was calculated after performing a shift on the data that accounts for the different set points. This gives a clear picture of the extremely stable operation of the target over the thirty days. As a result of the communication interruptions, a backup Lakeshore temperature controller was obtained in order to remedy the communication issues and improve the system for the next beam time.

In January 2020, the target's hydrogen cell was damaged during a leak test, and the ladder was shipped back to the University of Michigan for repair (see section 3.4 for details on the maintenance performed). Due to the COVID-19 pandemic and inability to travel internationally in 2020, no liquid hydrogen scattering data was taken in 2020 due to a shortage of on-site support at PSI.

In 2021, the target was cooled down and operated from November 16 - December 18 with an up time of 82%, due to a communication lapse between the Lakeshore temperature controller and the slow control program, stopping operation to address a leak that developed in the compressor's pipe, and an lab-wide interruption in the chilled water service needed to operate the compressor. The temperature of the target during this time, including during the interruptions, is illustrated in figure 3.8a. The three interruptions that are highlighted in orange are excluded from the temperature data in the histogram in figure 3.8b. When the compressor pipe developed a leak, the LH_2 in the target was evaporated and the target warmed up in order to replace the compressor.

This allowed us to continue taking data while the copper pipe from the compressor was repaired. We also switched to using distilled chilled water in the compressor, as the non-distilled water was likely what caused the pinhole leak in the pipe (seen in figure 3.9). When taking into account the offsets to the temperature during each stable point, accounted for in the same manner as in the Fall 2019 data, the target performed at stable temperature for 620 hours.

For the 2022 beam time, the target was filled with LH_2 from October 13 - December 15 with a 100% up time, as shown in figure 3.10a. This almost two-month period faced no interruptions and allowed for continuous data taking during the 2022 beam time, during which MUSE collected data mainly at ± 115 MeV/c. From the Fall 2019 and 2021 beam times, we were able to address previous causes of interruptions to operation - there were no communication freezes during the 2022 beam time as a result of replacing the Lakeshore temperature controller and updating the slow control program to check and accommodate for any possible lapses in communication. This continuous operation resulted in the longest uninterrupted running of the target, and one of the most stable temperature behaviors as

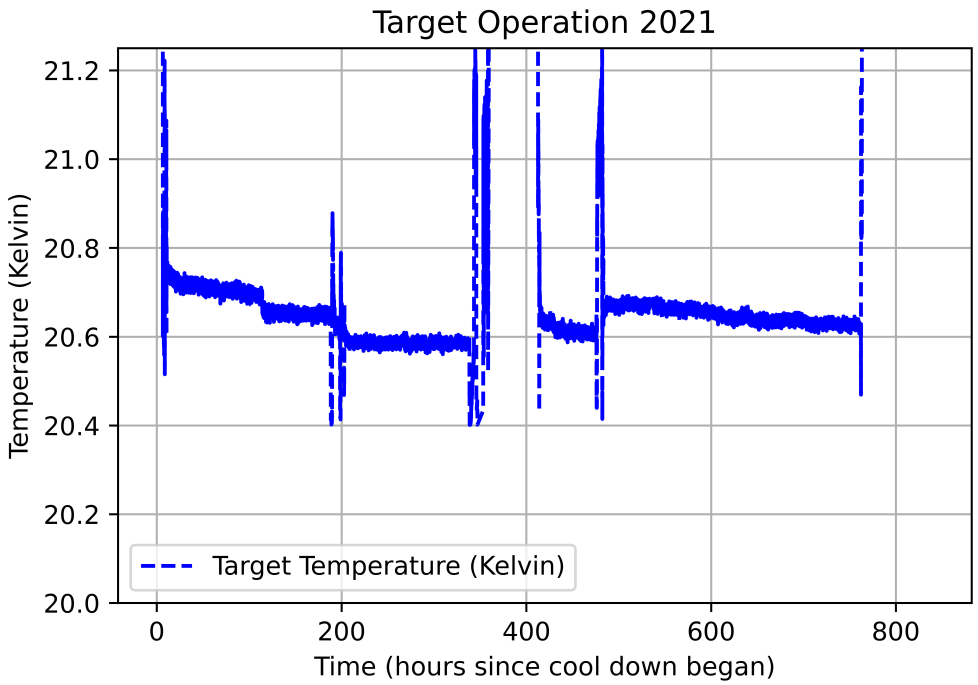

(a)

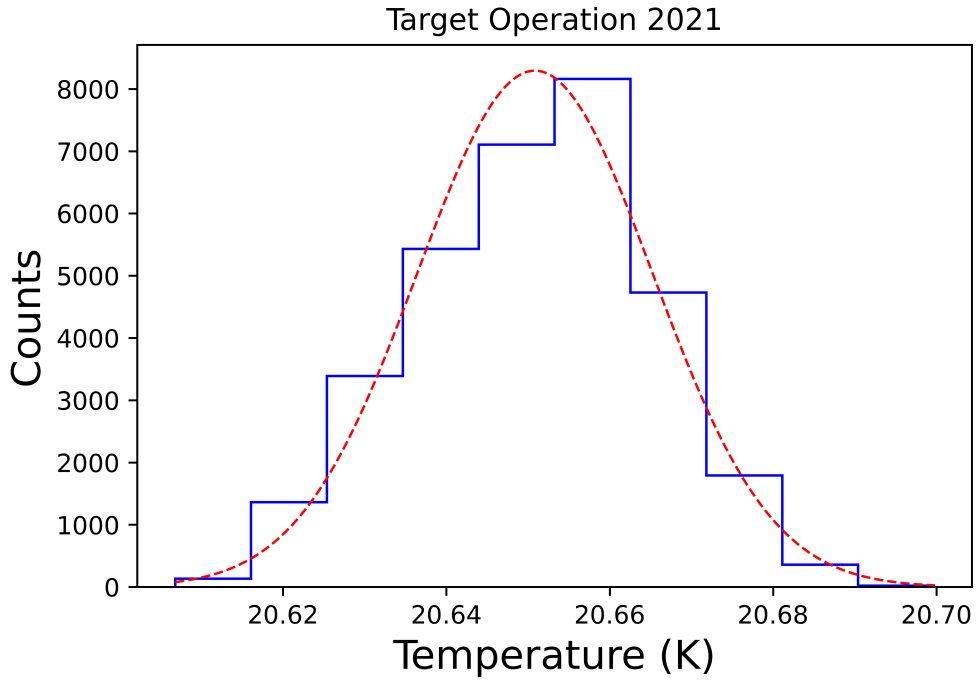

(b)

Figure 3.8: Target operation from November 16 - December 18, 2021. Panel (a) shows the target temperature data trend over time during the 2021 beam time. Panel (b) shows the histogram of temperature data from the target during the 2021 beam time. From the four stable operation periods, offsets were applied according to the different temperature set points used, which gave a mean temperature of 20.71 K and stability of 0.013 K.

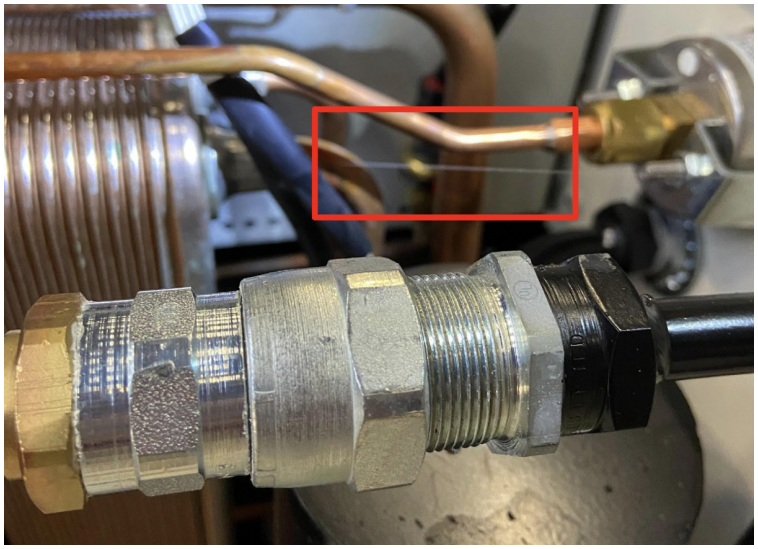

Figure 3.9: Photo of pinhole leak in the compressor used in the target system visible in the red box. The target operation was paused while this compressor was replaced during the 2021 beam time.

seen in figure 3.10b.

In 2023, MUSE utilized two separate beam times in PiM1 and had target operation from July 10 - September 8 (seen in figure 3.11a) with a 99.7% up time for the first one, and operation from December 8 - 18 (in figure 3.12a) with 100% up time. The beam time in December 2023 is the first beam time to use a different ladder from the rest of the beam times 2019 - Summer 2023; due to a leak caused by an overheating of the target after a chilled water interruption in September 2023, the ladder that had been used consistently was shipped back to the University of Michigan to replace the cell and repair the leak. More information on this cell repair is detailed in section 3.4.

With a minor interruption in the middle of the summer operation time, around hour 800 in figure 3.11a, caused by an update done to the slow control system that required the system to be restarted, the temperature setpoint shift was accounted for when looking at the temperature histogram for this period, shown in figure 3.11b. The shorter running period in December was continuous, and its histogram in figure 3.12b. This mean of 20.53 K corresponds to a target density of 0.07 $\frac{g}{cm^3}$ with a density stability of 0.03%.

From the original integration and commissioning of the full target system, the operation has been incredibly stable and successful, with the operation and monitoring systems working as expected to properly handle the aforementioned interruptions in operation. With the temperature data, we are able to calculate the target density, which is used in the calculation of the cross section, and its dependence is shown in equation 4.16. The target density can

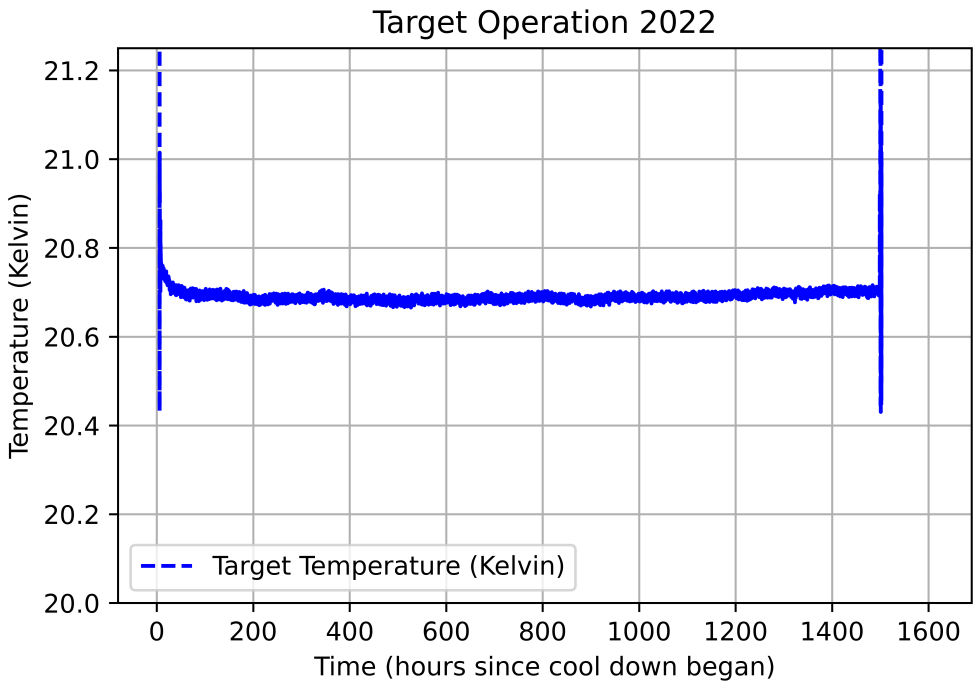

(a)

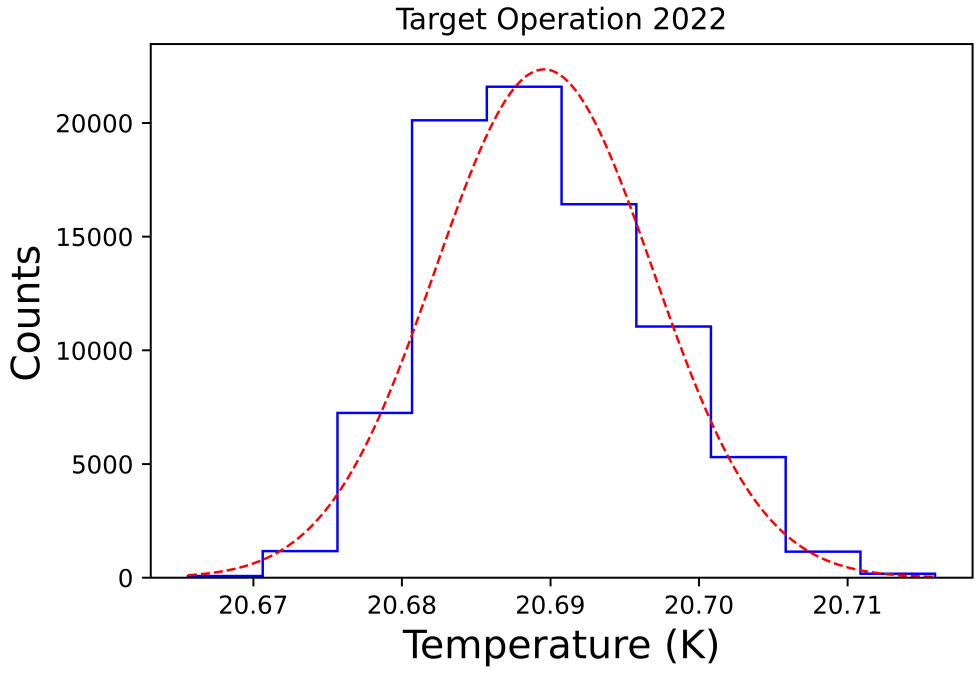

(b)

Figure 3.10: Target operation from October 13 - December 15, 2022. Panel (a) shows the temperature trend data during the 2022 beam time. The target operated for two months continuously without any interruptions, which is its longest sustained operation period. Panel (b) shows the histogram of temperature data for the target from the 2022 beam time; the mean temperature was 20.69 K, with a standard deviation of 0.008 K.

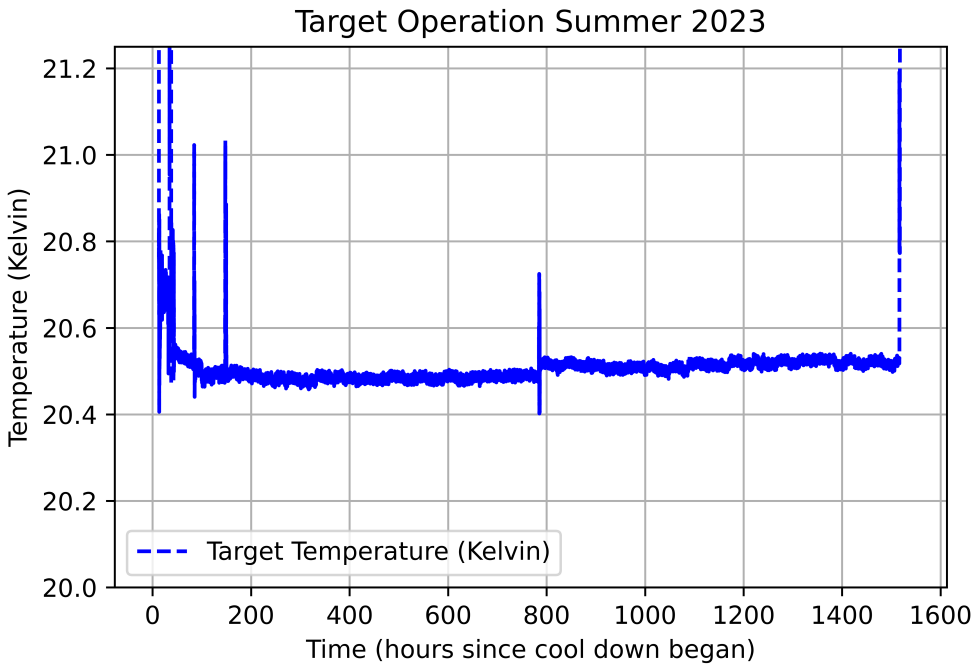

(a)

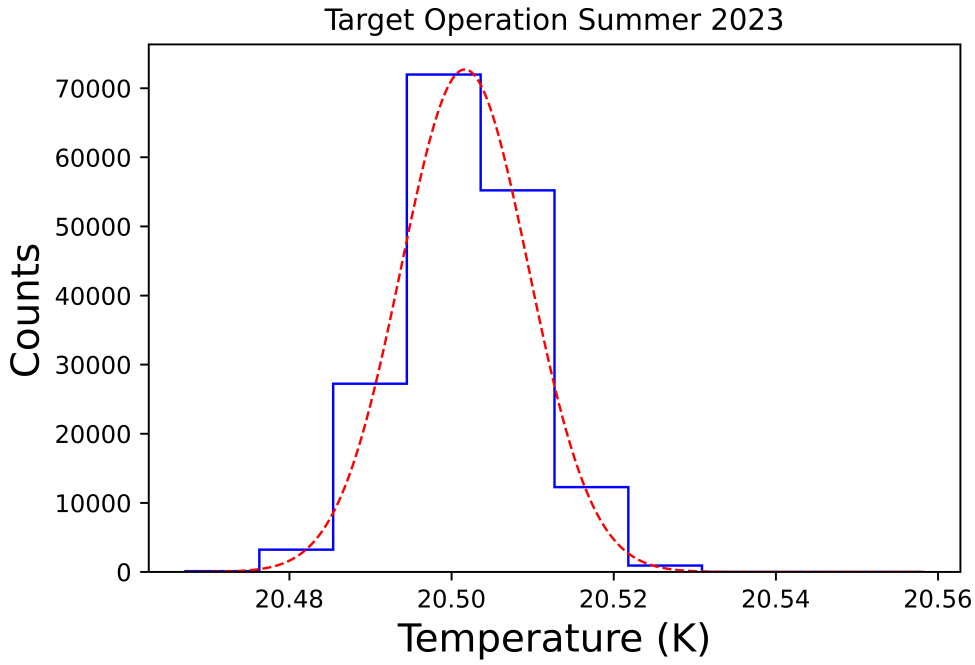

(b)

Figure 3.11: Target operation from July 10 - September 8. Panel (a) shows the temperature trend data where the target operated from July 7 to September 8, and the early temperature fluctuations are due to extremely high temperatures at PSI in Switzerland, which required us to replace the MUSE water chiller with a higher-powered water chiller in order to continue operating during the summer. Panel (b) shows the histogram of target temperature data for the Summer 2023 beam time; the mean temperature was 20.50 K with a standard deviation of 0.008 K.

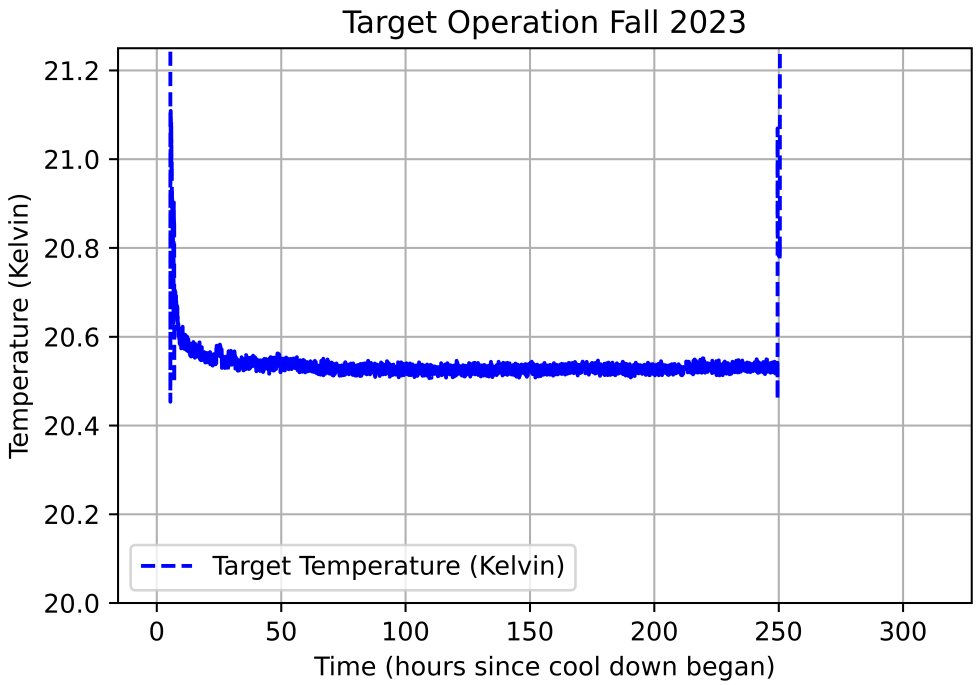

(a)

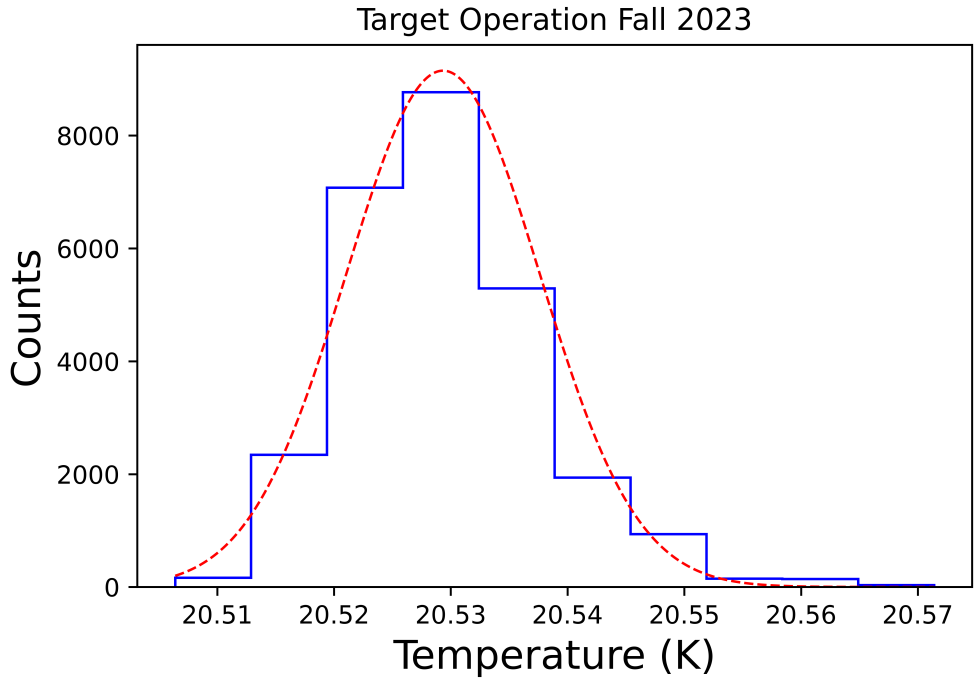

(b)

Figure 3.12: Target operation from December 8 - 18, 2023. Panel (a) shows the target temperature data over the Fall 2023 beam time. There were no interruptions during this 11-day running period. Panel (b) shows the histogram of the target temperature data for the Fall 2023 beam time; the mean temperature was 20.53 K, and the standard deviation was 0.008 K.

Beam Time	% Uptime	Mean Temperature (Kelvin)	Temperature Stability (Kelvin)	Mean Target Density ($\frac{g}{cm^3}$)
2019 - Summer August 6 - 11	100% 128/128 hours	20.69	0.015	0.0697
2019 - Fall November 27 - December 23	97% 546/562 hours	20.68	0.010	0.0698
2020	-	-	-	-
2021 November 16 - December 18	82.4% 620/752 hours	20.71	0.013	0.0697
2022 October 13 - December 15	100% 1450/1450 hours	20.69	0.008	0.0697
2023 - Summer July 10 - September 8	99.7% 1426/1431 hours	20.50	0.008	0.0700
2023 - Fall December 8 - 18	100% 233/233 hours	20.53	0.008	0.0699

Table 3.1: Summary of the hydrogen target performance for beam times from 2019 - 2023. Years where the MUSE beam time was split into multiple sections are treated as two different operation periods.

be written as a function of temperature

$$\rho(T) = a \cdot T^2 + b \cdot T + c, \tag{3.1}$$

where $a = -3.09 \times 10^{-5} \frac{\frac{g}{cm^3}}{K^2}$, $b = 9.99 \times 10^{-5} \frac{\frac{g}{cm^3}}{K}$, and $c = 8.09 \times 10^{-2} \frac{g}{cm^3}$. With this, we can calculate the mean temperature density for each running period, as well as the density stability; these values are included in table 3.1.

3.4 Target Ladder Repair and Improvement

To prepare for unexpected events during data taking for MUSE, three identical target ladders were constructed, so that two spare ladders would be available and ready to replace the ladder currently in use. The three ladders were at both the University of Michigan and PSI between their construction and present day; the specification of the ladder numbering, and the full timeline of the ladders' improvement and survey work is catalogued in Appendix B. In addition to the three ladders, Creare provided a soldering jig that has a straight alignment and gives us a baseline of reproducibility between the ladders. This was utilized when soldering the VCR connection to the fill tube on the LH_2 cell, or resoldering it in an attempt to make the ladders straighter, since this was the main connection point at which the ladders developed an angle offset away from the center of the chamber where the beam comes in.

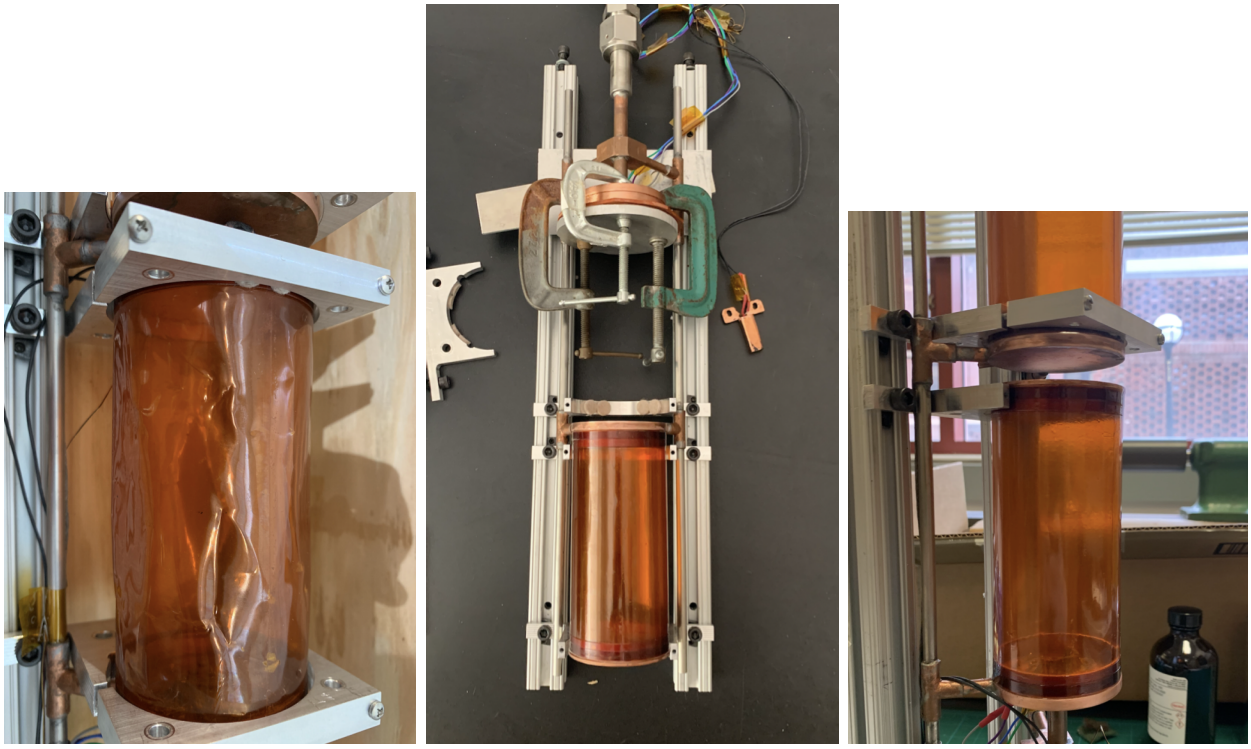

(a) (b) (c)

Figure 3.13: Photos taken during LH_2 cell replacement in July 2020. Panel (a) shows the original cell that was crumpled during a leak test, planel (b) shows the ladder during the repair process where the old cell is removed, and panel (c) shows the new cell in place while the epoxy is drying.

3.4.1 Target Ladder 3 LH_2 Cell Replacement 2020

After work was done at PSI to straighten the ladder used in 2019, the LH_2 cell was damaged, and the Kapton cell needed to be replaced; the ladder was shipped from PSI to Ann Arbor in early 2020. During the initial construction of the target ladders, additional cylinders made of the four layers of Kapton were constructed to be available in case there was a need to replace just a cell at any point in the future. The Kapton cell fabrication process is meticulous and time consuming, so multiple extras were made on top of the two spare ladders to prevent the need to go back and create more cells later. In July 2020, I worked with the target group at the University of Michigan to remove the damaged hydrogen cell and residual glue, replace the cell and extra strips of Kapton, and leak check the system after the cell was exchanged. This successful replacement of the damaged cell allowed MUSE to continue taking data with the same ladder, which was also the ladder with the smallest angle offset.

The use of the same ladder through beam times 2019-2023 gives MUSE a geometric

advantage because, although all three ladders were made using the same schematic and alignment tools, the soldering of the main VCR joint that connects the hydrogen gas line to the LH_2 cell is not exactly reproducible. The goal of the ladder is to have the full and empty cell occupy the same space when moved vertically in and out of the beam, but each ladder has a different small angle offset from perfectly straight, causing a slight displacement in the $\pm x$ direction that affects the background subtraction of the cells. Using the same ladder across beam times allows us to study, better understand, and more precisely account for the angle offset.

3.4.2 Target Ladder Alignments

Once ladder 3 was shipped back to Michigan and repaired, it was used as the standard of alignment for all three ladders. In order to have the three ladders be as identical as possible, we rebuilt the soldering jig from Creare by machining new components and resurveying all the measurements for the jig. We then placed ladder 3 in the jig and made precise adjustments to the components so that the jig was well-aligned with the ladder. Once these adjustments were made, we used the soldering jig to resolder the support pipes and VCR connections of ladder 1 such that it would more consistently match the alignment of ladder 3.

After these two ladders were repaired and resoldered, ladder 3 was sent back to PSI, along with a set of alignment components constructed at Michigan to more precisely measure the straightness of the ladders. After surveys were performed at PSI on the target ladders using the alignment rod and plate, ladder 2 was shipped back, and ladders 1 and 2 were resoldered with the jig in August 2021 (the comprehensive timeline of ladder improvement and shipping between Michigan and PSI is detailed in Appendix B).

3.4.3 Ladders 1 and 3 LH_2 Cell Replacement 2024

As mentioned in section 3.3, ladder 3 developed a leak in the seal of Kapton to the copper end caps because of an overheating issue, that melted some of the epoxy used. In addition to this, ladder 2 developed a leak in the cell as a result of a faulty pressure regulator during a leak check. Both of these ladders were shipped back to the University of Michigan to be repaired, where the LH_2 cell and its seal would be replaced for each ladder.

I worked with several undergraduate students in the Lorenzon group: Ethan Hazelton, Ruide Xu, and Jessica Brandt, to attach new Kapton cells to the ladders. We glued the bottom end caps, then the top end caps, and finally added the broad and narrow strips of Kapton that strengthen the seal at the lip of each end cap. This repair work took place over the course of January 26 - February 7, 2024, and we worked with Richard Raymond

to perform pressure tests on both ladders to check for leaks after the epoxy had dried and sealed. Both ladders had some form of leak, and we are currently working on repairs before we plan to ship them back to PSI before the 2024 beam time starts in June.

CHAPTER 4

MUSE Analysis

4.1 Overview of Analysis

In order to achieve the physics goals for MUSE and extract cross sections and the proton radius, the analysis software must handle input from our scintillating and tracking detectors, reconstruct scattering events of interest as well as identify the particle species involved, and have the capability to account for noise, multiple scattering, and radiative correction effects from higher order processes such as two-photon exchange contributions. In response to these needs, the analysis software for MUSE employs a structure, represented in figure 4.1, that allows us to process data from experimental data collection as well as simulation in the same framework, with a difference in the initial process of preparing the raw data from each source to be compatible with the software. For the experimental data, the decoding and channel mapping step is handled in the conversion of the raw detector data, described in section 4.1.1.

4.1.1 Midas to ROOT Conversion

The MUSE analysis framework is inherited from a previous experiment OLYMPUS [48], where the analyzing capabilities are handled through plug-ins, files that contain modular groups of functions written for a specific purpose, such as the analysis of data input from a single detector. The process of analyzing is done through the cooker, which is the framework's executable structure. This structure takes in commands in the form of a recipe or set of recipes, which call any combination of plug-ins and run the indicated data through the selected recipe(s). Information is relayed through this framework by trees containing relevant information and respective identifying labels.

The MUSE trigger and the DAQ system collect information from the scintillating and tracking detectors during a run and store this information in the form of Midas files, which are then processed by the converter within the analysis. This file structure includes event

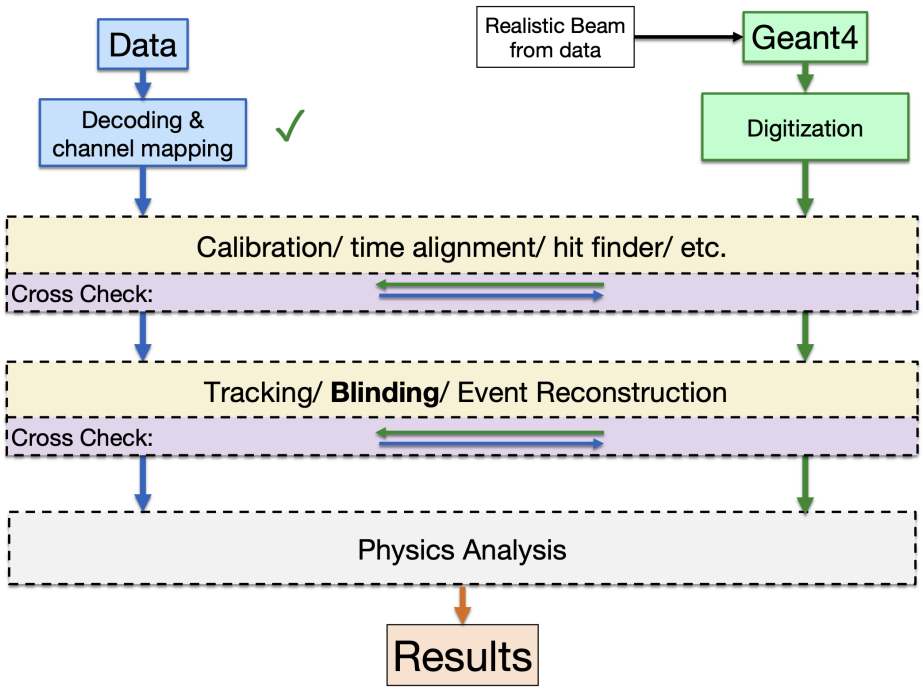

Figure 4.1: Graphic representation of the MUSE analysis structure. Produced by Ievgen Lavrukhin.

identification, a time stamp, and recorded timing and energy information. The base level of the analysis is this converter, which decodes the timing and deposited energy information from the detectors and produces the information in a format that can be physically interpreted. The output of the converter contains the raw information from the detectors, and it is now in a ROOT format, which is used throughout the rest of the analysis process. This first step also evaluates channels from all detectors and checks that they are properly mapped and ordered within the MUSE coordinate system, so that the reconstruction of events is handled by an accurate geographical representation of the detectors in the MUSE setup.

4.1.2 Low-Level Detector Analysis

Once a ROOT file is produced, the next step in the analysis process is mainly individual detector analysis; for each detector that collects and stores data, there is a set of analysis that processes its inputs and produces identifying information for each event, including the presence or absence of hits in the detector along with its timing information and coordinates for its perceived location. The components from each detector's input allow us to comprehensively reconstruct events and select on scattering events with sufficient information and

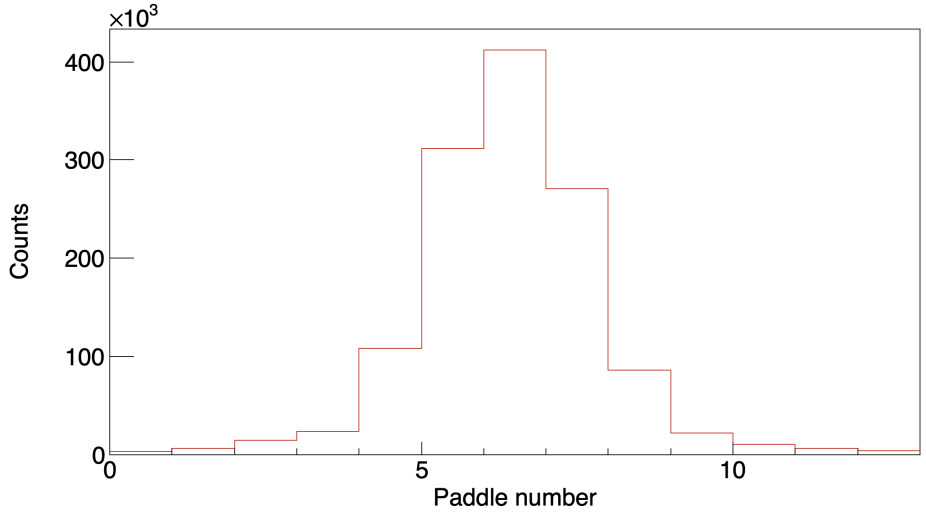

Figure 4.2: Distribution of hits on the paddles in plane D of the BH.

particle species of interest.

The BH and SPS are the scintillating detectors utilized for identifying and characterizing the beam line and scattered particles, respectively. For the incident particles, the BH collects timing and coordinate information that, when packaged into hits for each event, allow us to identify particle species through TOF calculations done using the timing information from the BH-registered hits and the Radio Frequency (RF) timing information from the accelerator. Figure 4.2 shows an example distribution where the BH plane is collecting hits for incoming detected particles. We use the RF spectrum, seen in figure 4.3, in the BH to determine incoming particle identification (PID), which helps inform the scattering events of interest to select on later, as well as providing a baseline to compare potential particle decays to. The analysis for the BH takes in the raw ROOT data file and produces an output tree containing PID, timing, and location data for each registered hit. For scattered particles, the SPS processes raw signals in a very similar way, taking in the raw run data from the ROOT file and producing a catalogue of hits detected for each event in the run that inventories each hit's timing and location data. At higher levels, the timing information from the BH and SPS will be combined to determine the reaction ID and reconstruct the particles involved in a scattering event of interest.

The GEMs and STTs are our track-forming detectors for incident and scattered particles, respectively. The processing step before the track formation involves translating the Analog-to-Digital Converter (ADC) information from each GEM channel and timing signals from each STT straw into conclusive hits where particles traveled through the detector's multiple layers. Determination of hit candidates and their locations for the GEMs depends on an

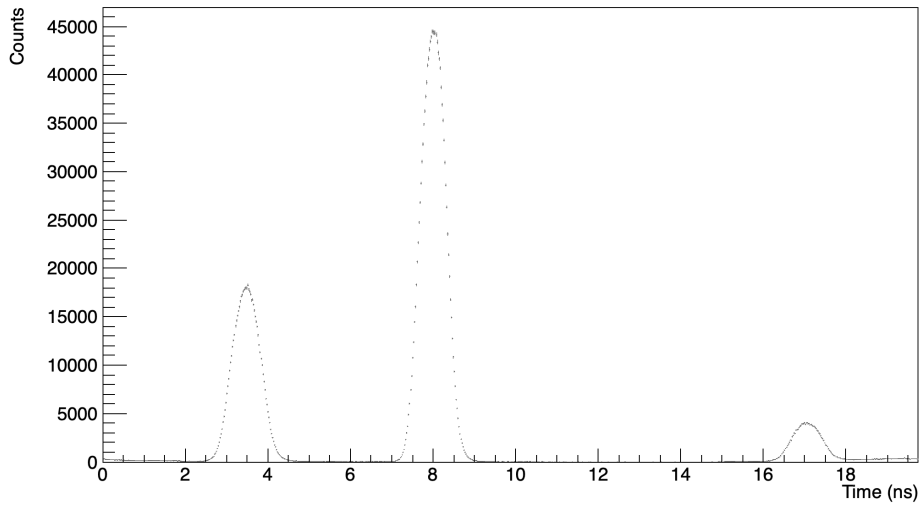

Figure 4.3: RF spectrum of incoming particles detected by BH plane D using timing information from the accelerator and the BH scintillator bars. Each peak in the plot is a particle species, with the electron peak centered at 8 ns, the muon peak at 17 ns, and the pion peak at about 3.75 ns.

analysis of the ADC spectrum, where hits will correspond to clusters within the spectrum where the ADC values are much higher than the surrounding channels. In the case of the STTs, selection of a hit depends on a signal within a straw that receives a time signal, where the width of the pulse (time over threshold) and the drift time (given by the leading edge of the pulse) are used to select on and determine the location of the hit. The drift time is used to determine the position of the hit within a straw, through the time to distance conversion [45]. Obtaining the distance from this calculation allows us to determine the position of a hit within a given straw, which plays a crucial role in the fitting and track forming done at later analysis stages.

Other inputs to the analysis that help inform the decision-making on selecting quality events include the BM, VETO, TCPV, calorimeter, and BFM. The BM, VETO, and TCPV are all used for the purpose of removing events that don't contain relevant scattering events from the data set that will be analyzed to produce cross section values.

4.1.3 Tracking: Candidacy and Construction

For both our incoming and scattered particle tracking detectors, we take the low-level detector analysis from the tracking detector, where hits and their timing and coordinate information are recorded, and we use a fitting algorithm to optimize the grouping of these hits to form tracks that show the trajectory of the incoming or outgoing particles. In the process of

forming these tracks, we aim to minimize the χ^2 associated with the fitting for each grouping of hits.

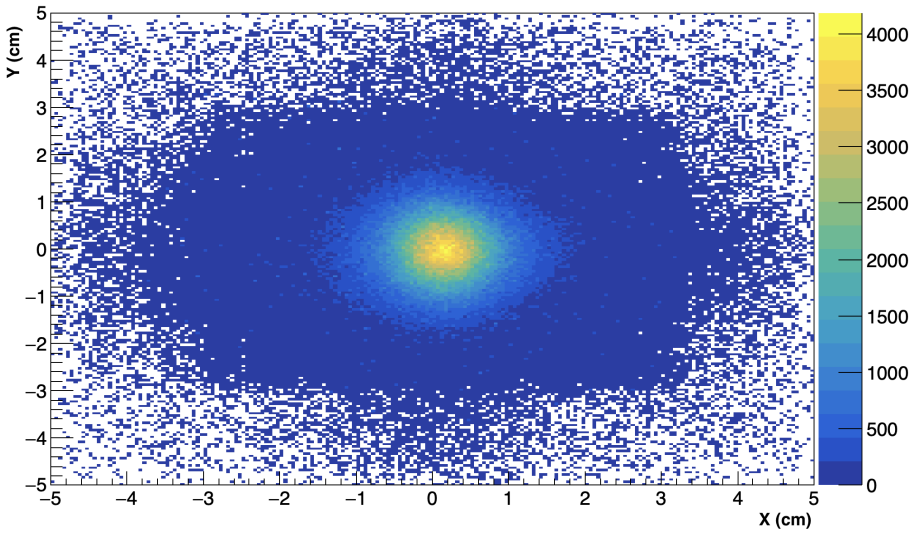

Figure 4.4: Projection of the GEM tracks constructed on to the most downstream plane of the GEMs. The concentration at the center of the plot shows that a majority of the particles pass inside a 2 cm range in x and 1.5 cm range in y, which is expected from beam simulations [2].

The GEM tracks are formed through fitting, and fiducial cuts around the target region are used to select on GEM tracks that likely contribute to relevant scattering events. Figure 4.4 shows how the projection of GEM tracks can be visualized, allowing us to then select tracks based on their trajectories toward the target region.

The formation of tracks in the STT is more difficult than in the GEMs because of the much larger variation in location and direction of scattered particles, as opposed to the general agreement and concentration of particle trajectory in the beamline. In figure 4.5, the STT tracks that are formed are projected onto the front wall of the SPS, and their intersection with this plane is plotted. This visualizes the distribution of scattered particles traveling outward from the target to the SPS walls, where we are able to collect timing and position information to form comprehensive picture of the scattering event.

4.1.4 Event Reconstruction

Once viable tracks have been constructed in the GEMs and STT, we have the components necessary to reconstruct both the vertex where the scattering event occurs and the full path that it travels inside the MUSE apparatus. For each event with qualifying incoming and

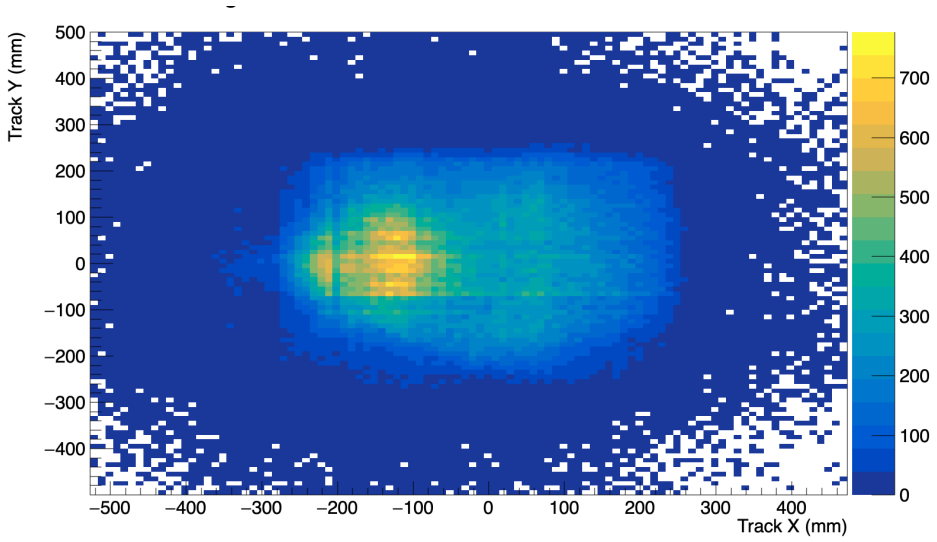

Figure 4.5: 2D projection of constructed STT tracks onto the front wall of the SPS. The concentration of intersection points on the wall correlate with our expectations concerning the distribution of scattered particles as a function of angle (in the x-direction) and matches the height of the vacuum chamber (y-direction).

scattered tracks, we reconstruct a single scattering vertex in the target region. The analysis takes the tracks formed and projects them toward the target, ensuring that the scattering event occurred within the region of interest where the liquid hydrogen cell sits inside the vacuum chamber. The track projection is done by calculating a parameter t, given by

$$t = \frac{m[0] \cdot pos.X + m[1] \cdot pos.Y + m[2] \cdot pos.Z}{m[0] \cdot dir.X + m[1] \cdot dir.Y + m[2] \cdot dir.Z}, \tag{4.1}$$

which is then used to calculate the point where the track intersects the plane of the target, given by

$$intersection = \begin{pmatrix} t \cdot dir.X + pos.X \\ t \cdot dir.Y + pos.Y \\ t \cdot dir.Z + pos.Z \end{pmatrix}, \tag{4.2}$$

with $\begin{pmatrix} dir.X \cdot x \\ dir.Y \cdot y \\ dir.Z \cdot z \end{pmatrix} + \begin{pmatrix} pos.X \\ pos.Y \\ pos.Z \end{pmatrix}$ being the representation of the incoming or scattered track and the plane of the detector (in the case of vertex reconstruction, the target) is represented by $m[0] \cdot x + m[1] \cdot y + m[2] \cdot z = m[3]$.

From this projection, we look at the point at which the distance between the two tracks is minimized. This value, called Distance of Closest Approach (DOCA), is the length of the line

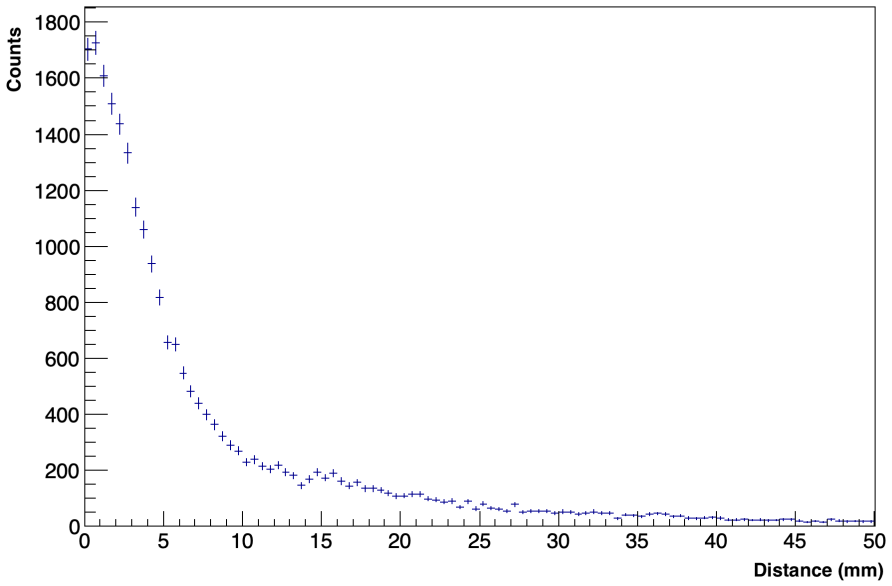

Figure 4.6: Distance of closest approach between the associated GEM track and the STT track that are used to form vertices for a given run at +210 MeV/c.

segment that connects the two tracks at the minimized distance. The midpoint of this line segment is used as the coordinates for the scattering vertex of this event. For an infinitely precise set of tracking detectors, the two tracks would intersect at a single point where no space remains between the tracks. For events where there are multiple track candidates from either or both detectors, we compare and select on the set of tracks for which the DOCA is minimized. Figure 4.6 shows a distribution of DOCA for vertices, where most vertices formed have a separation of 20 mm or less between tracks; we will later place cuts based on any DOCA that is too large to be accepted, based on the resolution of the tracking detectors and the uncertainty of the track fitting.

We are able to reconstruct the rough position of the scattering vertex $\mathbf{V}$ as well as the associated DOCA $\mathbf{D}$ for a given event through the projection of the incoming and scattered tracks toward the target region by

$$\mathbf{V} = (\mathbf{P} + \mathbf{Q}) \cdot 0.5 \tag{4.3}$$

$$\mathbf{D} = |\mathbf{P} - \mathbf{Q}|, \tag{4.4}$$

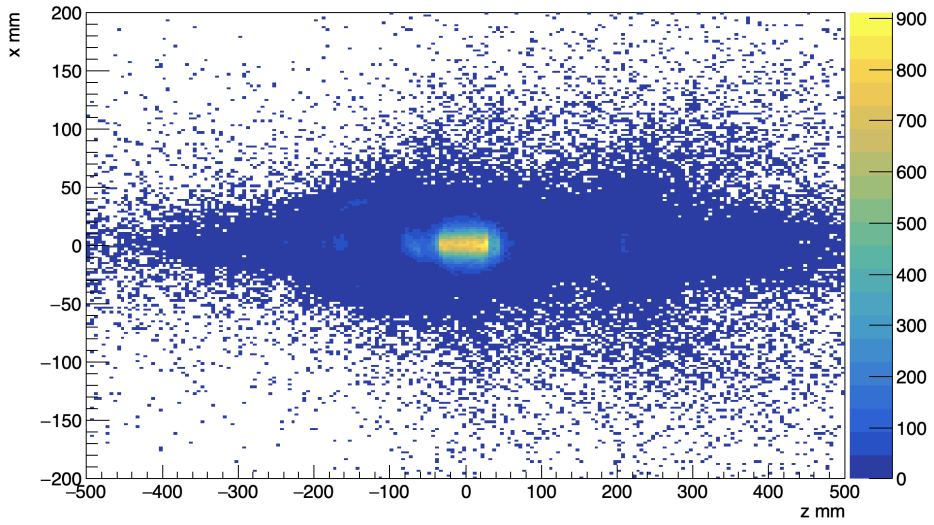

Figure 4.7: $x - z$ plane reconstruction of scattering vertices formed with associated GEM and STT tracks. The concentration of constructed vertices around $z = 0$ is expected and correlates to the scattering off the target inside the vacuum chamber.

where the vectors $\mathbf{P}$ and $\mathbf{Q}$ are calculated by

$$\mathbf{P} = \mathbf{P_0} + s\mathbf{u} \tag{4.5}$$

$$\mathbf{Q} = \mathbf{Q_0} + t\mathbf{v}. \tag{4.6}$$

For this calculation, $\mathbf{P_0}$ is the position used in defining the GEM track, $\mathbf{Q_0}$ is the position used in defining the STT track, and where $\mathbf{u}$ is the vector representing the GEM track, $\mathbf{v}$ is the vector representing the STT track. The variables s and t are used to simplify the notation of the calculation and are given by

$$s = \frac{b \cdot e - c \cdot d}{a \cdot c - b \cdot b} \tag{4.7}$$

$$t = \frac{a \cdot e - b \cdot d}{a \cdot c - b \cdot b}, \tag{4.8}$$

where a, b, c, d, e, and W_0 are proxies for different properties of the vectors representing the

incoming and scattered tracks:

$$a = \mathbf{u} \cdot \mathbf{u} \tag{4.9}$$

$$b = \mathbf{u} \cdot \mathbf{v} \tag{4.10}$$

$$c = \mathbf{v} \cdot \mathbf{v} \tag{4.11}$$

$$d = \mathbf{u} \cdot \mathbf{W_0} \tag{4.12}$$

$$e = \mathbf{v} \cdot \mathbf{W_0} \tag{4.13}$$

$$\mathbf{W_0} = \mathbf{P_0} - \mathbf{Q_0}. \tag{4.14}$$

The reconstruction of vertices in the target region is shown in figure 4.7, in which we can take note of the concentration of vertices around the target cell's location within the vacuum chamber, which is expected. With coordinates for the scattering vertex, we are able to combine information from the tracks, the vertex, and the scintillator hits from the BH and SPS to form a comprehensive picture of a particle's journey through the MUSE experimental set up through the reconstruction of the path traveled. Using the two tracks associated with the vertex, we project the GEM track upstream to the last plane of the BH and the STT track outward to the front SPS wall of the relevant side. The planes of the last BH plane and each front SPS wall will act as constraints for our start and endpoints, where we are able to utilize timing information for further analysis. Additional information on the processes for path length reconstruction can be found in Section 4.2.1.

4.2 High Level Analysis Components

In developing the MUSE analysis code, I had deep involvement in several projects that worked toward and improved the cross section extraction analysis, including path length reconstruction, trigger reconstruction, and studies on corrections to the effective flux at the target.

4.2.1 Path Length Reconstruction

Because MUSE operates in PiM1, which is a secondary mixed beamline comprised of pions, muons, and electrons, it is essential that we are able to accurately reconstruct the scattering events that happen, from identifying the particles involved in the collision to fully reconstructing the paths of the incoming and scattered particle, as well as the vertex where the collision occurred. Within the MUSE experimental set up, we are able to determine the identity of the scattered particle using the full path length traveled by the particle in

conjunction with the respective time of flight, using timing information from the BH and SPS.

In order to reconstruct the path length, it is key to identify a vertex and its associated tracks - GEMs provide the trajectory for the incoming particle, and the STT provides the information for the scattered particle. The tracks are projected into the target region to form the vertex, and they are projected onto the scintillating detectors to extract timing and distance information. The vertex is constructed by associating incoming tracks from the GEMs with scattered tracks from the STT, where the tracks, when projected to the target region, have a DOCA that satisfies the cut condition of being smaller than the uncertainty determined by the resolution of the tracking and scintillating detectors. Due to the uncertainty corresponding to the fitting of hits in the GEMs and STT for the formation of tracks, there is some distance between the closest point on the projected tracks instead of a singular intersection. Therefore, a line segment is formed between the two tracks at their smallest DOCA, and the vertex is recorded as the coordinate position of the center of this line segment.

The path length analysis takes the BH hits, SPS hits, GEM tracks, STT tracks, and constructed vertices for any given run, and it uses the inputs to calculate the full path traveled by any given particle that comes in and scatters off hydrogen in the angular range covered by the SPS and STT. For each event in a run, we use an identified "best" vertex (quantified by which constructed vertex has the smallest DOCA between the two tracks) and its respective tracks in order to reconstruct the full event. To verify the vertex made by the tracks, we look for associated scintillator hits with each track. For the GEM track, it is required that there is at least one hit detected in the BH plane D within a defined DOCA range. This DOCA is the same fundamental quantity as mentioned in section 4.1.4, and it is calculated by

$$DOCA = \sqrt{(x_{int} - x_{hit})^2 + (y_{int} - y_{hit})^2 + (z_{int} - z_{hit})^2}, \tag{4.15}$$

where the coordinate of the hit is given by x_{hit}, y_{hit}, z_{hit}, and the intersection of the track with the detector plane is given by x_{int}, y_{int}, z_{int}.

Likewise, the STT track is verified by at least one hit in the SPS front wall within the defined cut conditions for DOCA between the hit and projected track at the plane of the SPS wall. The GEM track is projected upstream onto plane D of the BH, and the STT track is projected outward from the target to the front wall of the SPS detector for its corresponding side. For the GEMs, this projection and measurement is relatively straightforward, since everything is happening on the beam line with little variance in angles or distances. Once

a track is projected onto the scintillator plane, it is compared against the hits registered in that event. This is also simplified by the cut condition within the analysis that good scattering events are kept if they have one and only one hit in the BH plane.

The DOCA between the registered hit and point at which the projected track intersects the BH plane informs us on the quality of the scattering event within the context of the information we were able to collect on it from our detectors. We utilize this parameter to select the best scintillator hit in order to use the most accurate timing information for full path length and TOF calculations. However, with the STT tracks, we add the complications involved in having tracks at many different angles and potential noise to make the track reconstruction less clean.

The distributions of the measured DOCA for each track/hit pairing is shown in figure 4.8, where panel b shows that the distribution for the STT/SPS correlation is much wider and has a larger mean than the GEM/BH DOCA correlation, shown in panel a, resulting from the widely varied directions of the STT tracks as well as the larger area needing to be detected and analyzed for the scattered tracks than for the incoming tracks. Multiple scattering of particles off the target chamber also results in more variation and larger DOCA for the STT/SPS hit-track correlations. We therefore test the data set against a set of conditions to improve the statistical precision with good scattering events and comprehensive detected information to inform that. In addition to looking at the condition of at least one hit in the SPS front wall, we also compare the coordinates of the projected STT track with the geometry of the SPS wall - if the projected track were to hit outside of the wall in the experimental set up, we elect to rule out this vertex as a good scattering event because we are unable to collect necessary timing information from the SPS.

Once we have determined a vertex and its constituent tracks, we are able to calculate the full traveled path length, consisting of the incoming distance traveled and the scattered distance traveled. For each component, the start point is defined by the coordinate at which the track intersects the plane of its respective scintillating detector. So, the GEM track is projected upstream to the BHD plane, and the point at which the track passes through this plane is used. The vertex coordinate is used as the midpoint of the particle's path traveled; it acts as the endpoint for the incoming path and the start point for the scattered path. The end point for the scattered path is taken to be the point where the projected STT track passes through the front SPS wall for either side.

With the path length calculated, we are equipped to address a prominent complicating factor of mixed particle beams: particle decays before or after scattering. In the same spirit that we are able to determine an incoming particle's species through TOF information from the BH and the accelerator RF, we employ timing information to use TOF and categorize

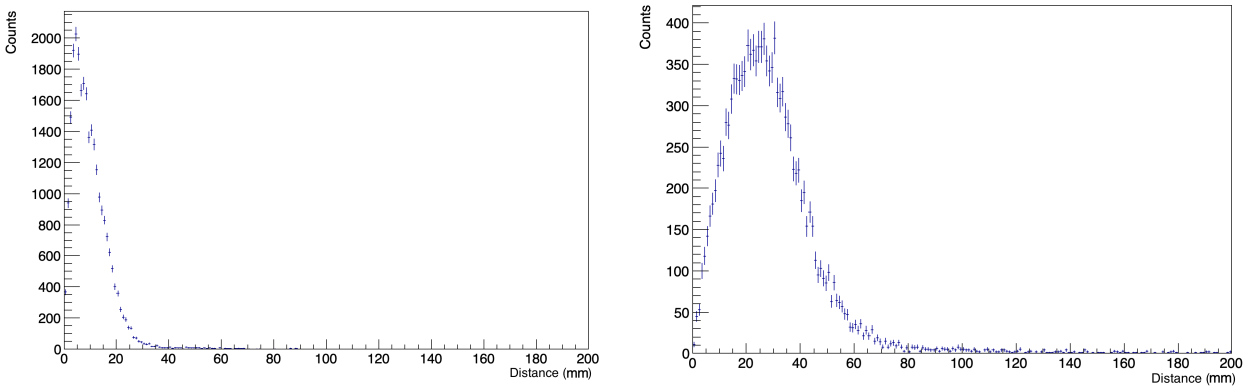

(a) (b)

Figure 4.8: Two examples of examining DOCA: Panel (a) shows the DOCA for GEM tracks projected to BH plane D, and panel (b) shows DOCA for STT tracks projected onto SPS left front wall.

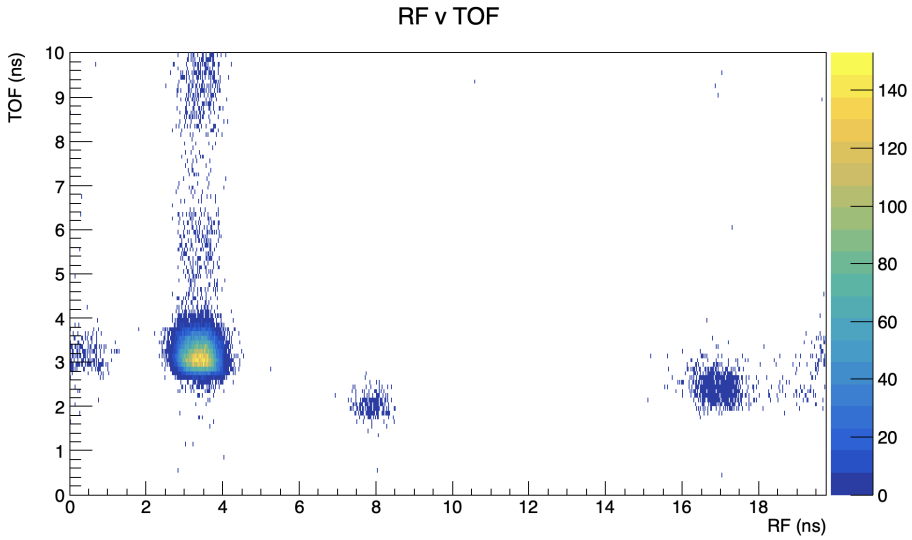

Figure 4.9: Particle TOF plotted against its accelerator RF timing. In addition to the grouping of particles from each species' RF (described in figure 4.3), the plotting against TOF gives us insight into which particles should be excluded from full analysis due to particle decay during flight.

scattering events. For each of the types of scattering events that we observe - electron, muon, and pion scattering off protons - all particle types have the same momentum when entering the MUSE set up. With the different masses of each particle, we then know their expected traveling velocity and can sort events with the calculation of an event's particle velocity. The timing information from the BH and SPS will give the total flight time of a

given particle associated with a scattering vertex, and this TOF will be combined with the path length to produce beta, a proxy for the particle's velocity. By plotting TOF against RF, shown in figure 4.9, we clearly see the three different particle species grouped around their corresponding TOF (calculated from the BH and SPS timing information) and RF time from the accelerator. From these groupings, we see cases that fall outside of these groups, likely indicating that a particle decay occurred during this scattering event. Looking at TOF and RF allows us to filter out the particle decays that cannot be used to extract meaningful cross section data. We also extract cut parameters for each particle species which can be used when examining scattering events and confirming or investigating the species involved in an event.

4.2.2 Trigger Reconstruction

Another tool that MUSE uses to exclusively select the events that are likely to produce good scattering events is a comprehensive trigger that governs the decision-making surrounding data acquisition during a run. There are four main inputs to the trigger logic and inform on whether a trigger is fired: seeing an e or a μ, not seeing a π, receiving a signal from the SPS communicating that a scattering event occurred, and detecting no hits in the VETO detector. For the main scattering trigger, these conditions are ANDed together to select only events that will be processed by the full analysis procedure. The selectivity of the trigger allows us to suppress many π-induced background events that would otherwise overwhelm the DAQ system. A more detailed description of the trigger and trigger logic employed by MUSE can be seen in section 2.3.

The trigger configuration can vary greatly in its structure and contents, so it is not possible to have a single hardcoded trigger configuration included in the analysis to interpret all possible triggers that can be fired. Within MUSE's trigger configuration, the L1 trigger that each channel represents stays constant, with the channel assignments listed in figure 4.10 and the set of channels that each L2 trigger represents can vary depending on the type of data that is being collected, some of which include scattering data, detector threshold configuration, and detector alignment. Therefore, we can utilize a binary representation of the L1 trigger's infrastructure in order to efficiently reconstruct the L2 triggers for higher level analysis. In the trigger reconstruction, the L2 triggers are comprised of a cumulative binary representation of each L1 trigger (that has its own fundamental binary representation) that makes it up, which allows for flexibility in handling the reconstruction of the trigger. As a result, each event's fired triggers is accessible through interpreting the Logic Gate ID (saved for every event in the DAQ system's slow control) in the context of the reconstructed

Trigger Input	Name:	0xa450	0xa451	0xa452
0	Pulser	x	x	x
1	OR_all_BM_bars	x	x	x
2	12×12 cm	x	x	x
3	Primary Proton Current Scaler	x	x	x
4	SPSL_UP	x	x	x
5	SPSL_UP_Positron	x	x	x
6	SPSL_Down	x	x	x
7	SPSL_Down_Positron	x	x	x
8	—	x	x	x
9	SPSR_UP	x	x	x
10	SPSR_UP_Positron	x	x	x
11	SPSR_Down	x	x	x
12	SPSR_Down_Positron	x	x	x
13	—	x	x	x
14	—	x	x	x
15	—	x	x	x
16	PID electron (plane D)	x	x	x
17	PID pion (plane D)	x	x	x
18	PID muon (plane D)	x	x	x
19	PID electron (plane C)	x	x	x
20	PID pion (plane C)	x	x	x
21	PID muon (plane C)	x	x	x
22	VETO	x	x	x
23	Post VETO	x	x	x
24	—	x	x	x

Figure 4.10: List of all L1 triggers used to construct triggers used for MUSE data collection.

L2 trigger. We reconstruct the full master trigger configuration and all of its L2 triggers by pulling the trigger's set configuration from the slow control and translating that into binary, so that we can directly compare it with each event's fired trigger information. The reconstruction for analysis is shown in figure 4.11 and allows us to emulate the trigger set for any run. It is not dependent on using the exact same channel configurations, so 4.11a could be changed between run types, and the binary representation in fig 4.11b would change accordingly. The division of L1 triggers allows us the flexibility to reconstruct the trigger regardless of the change in L2 configurations and combinations.

For each event, the information about which trigger fires is encoded in a variable called the logic gate ID; there are 16 bits in the ID, one for each channel in the L2 trigger. With our post-construction of the master trigger and the event's information about triggers fired, we can then explicitly compare any desired condition with the contents of each event. To construct a specific condition, one can choose one or more of the L1 triggers to be included in the condition, as well as opting to exclude any specific masks. With these constraints, we then do a direct comparison of the triggers fired with the constructed condition through binary operation, and it allows us direct access to the triggers that fired or did not in each event. A particular application of interest for this tool is looking at corrections to the flux in the context of the cross section calculations, which are detailed in section 4.2.3. The other key motivator to represent the MUSE trigger system this way in the analysis is to

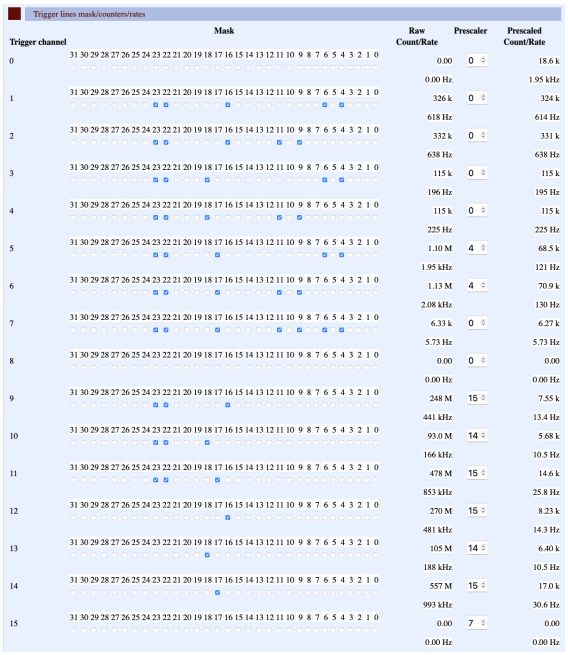

(a)

```
Master Trigger:
 0 : 00000000000000000000000000000001
 1 : 00000000110000010000000001010000
 2 : 00000000110000010000101000000000
 3 : 00000000110001000000000001010000
 4 : 00000000110001000000101000000000
 5 : 00000000110000100000000001010000
 6 : 00000000110000100000101000000000
 7 : 00000000110000100000101001010000
 8 : 00000000000000000000000000000000
 9 : 00000000110000010000000000000000
10 : 00000000110001000000000000000000
11 : 00000000110000100000000000000000
12 : 00000000000000010000000000000000
13 : 00000000000000100000000000000000
14 : 00000000000000010000000000000000
15 : 00000000000000000000000000000000
```

(b)

Figure 4.11: Representations of the MUSE master trigger configuration. Panel (a) shows a screenshot of master trigger configuration from the online webpage GUI for a scattering run; rows represent L2 triggers, and columns represent L1 triggers; panel (b) shows the corresponding binary representation of the master trigger reconstructed in the analysis code.

provide a fundamental framework that can be conveniently used both by the simulation data and experimental, so that the analysis process is readily compatible with data from both simulation and experimental data collection.

4.2.3 Studies for Flux Corrections

For the experimentally calculated cross section

$$\frac{d\sigma}{d\Omega} = \frac{N_{scat}(p,\theta)}{N_{inc}(x\rho)_{target}\Omega_D\epsilon}, \tag{4.16}$$

where N_{scat} is the number of scattered particles, θ is the scattering angle, p is the momentum, $(x\rho)_{target}$ is the areal density of the target, Ω_D is the solid angle, and ϵ is the efficiency factor, the beam flux N_{inc} is an important component of this calculation, and it is complex to evaluate due to the nature of the mixed secondary beam of MUSE. The flux N_{inc} is calculated using

$$N_{inc} = N_{scaler} \times \epsilon_{corr}, \tag{4.17}$$

with N_{scaler} being the raw count of particles of a particular species given by the trigger system, and ϵ_{corr} representing the correction factor for the raw count of the particle flux. The correction factor is comprised of several components that affect the number of analyzable events constrained by particles being counted properly by the detector system and reaching the desired target region; this correction factor is one of multiple correction factors that contributes to ϵ in equation 4.16. Others include detector efficiency and DAQ efficiency. This will ultimately allow us to calculate the beam flux and therefore normalization factor more accurately than without these correction components. The trigger system that MUSE uses counts particles using the BH and information from the accelerator's RF timing. With this set of timing information, TOF can be used to identify each particle's species and correctly sort it for the counting of beam particles.

For each particle species, the raw count of particles N_{scaler} is stored in the master trigger's information through the scalars provided by the trigger. Because of the initialization the DAQ system uses, there is an offset in the scalars counted given by the number produced with the first event. In addition to this, we consider particle identification cuts, simultaneous hits within events, GEM track projection to the target, and multiple PID triggers firing within a single given event as factors that could contribute to a corrected flux and a more accurate normalization. With the corrected flux, we can then more accurately produce the measured cross section for our scattering events of interest.

As mentioned in section 4.2.2, we are able to compare the triggers that fired in an event

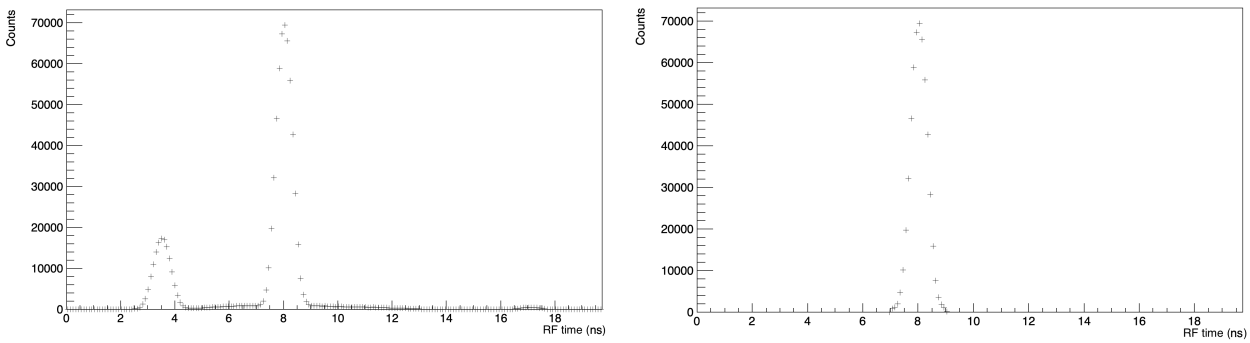

(a) (b)

Figure 4.12: Panel (a) shows particle RF time for events where the beam line electron PID trigger fired; panel (b) shows particle RF time for events with beam line PID electron trigger with RF cut on the electron peak.

to a hypothetical condition we create in order to look more closely at certain situations. With the studies for flux calculations, we want to examine the behavior of hits in the BH in the context of PID triggers firing in BH plane D. We can produce an accurate count of the number of PID electron triggers fired in a run and, going further, can determine when events need to be excluded from the data set and therefore from the flux count. The foundational case for this is looking at the RF spectrum for a given PID trigger and disqualifying the hits that fall outside of the peak corresponding to the relevant particle. Figure 4.12 shows the case from a run at +210 MeV/c data where we select and plot events for which the PID electron trigger for BH plane D fired. Figure 4.12a shows the initial plotting, and figure 4.12b shows the events that survive the cut in the process of calculating the correction factor for the flux.

After the PID cuts are applied, events survive that contain simultaneously firing PID triggers, and these events need to be removed from the data set that will be fully processed. In order to filter these events out, we look at the subset of data where the electron PID trigger fires, and then we can check from here if either the PID muon or PID pion triggers also fired in the same event. If more than one PID trigger has fired for any given event, it is removed from the dataset and the flux count because we handle a single scattering vertex and set of associated tracks, and multiple scattering events would obscure our picture of good scattering events. Figure 4.13 shows the case of looking at a single PID trigger fired, before and after we remove cases where more than one PID trigger fires; the green in each bin represents accepted particles, while the red section of each bin represents rejected events based on the condition of having one and only one beamline PID trigger fire. Here, using a run from +210 MeV/c as an example, we examine the reduction in analyzable events on the

condition of only one beam line PID trigger firing in a given event. The section of each bin highlighted red shows the fraction of events that are removed because more than one PID trigger fired.

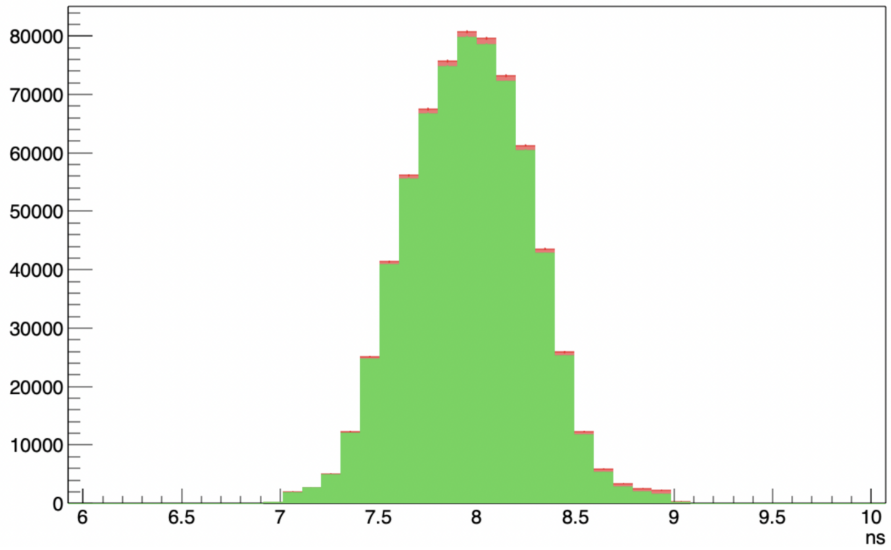

Figure 4.13: Distribution of RF timing hits in BH plane D - green sections of each histogram bar represent accepted events, and red sections represent rejected events.

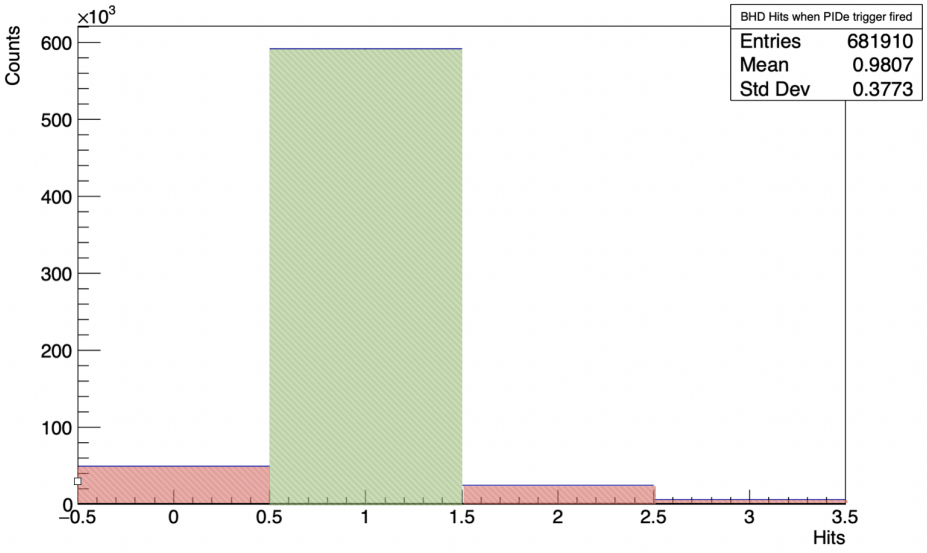

Figure 4.14: Distribution of the number of particle hits seen in BH plane D. Events with one and only one hit seen in BH plane D are kept (colored in green), and all other events (colored in red) are excluded from full analysis as well as the calculation of the flux.

Similar to the complication of multiple PID triggers firing, we also have the case where

Particle Type	$\mathbf{N_{scaler}}$	$\epsilon_{\mathbf{corr}}$	$\mathbf{N_{inc}}$
(+)210 e	3.91×10^8	0.79	3.09×10^8
(+)210 μ	3.49×10^8	0.87	3.04×10^8
(+)210 π	3.99×10^9	0.86	3.39×10^9

Table 4.1: Example of incident particle flux before and after correction factor is applied for each particle species. These correction factors are expected to vary between both different species and different momenta.

simultaneous hits in the BH plane are too close together for the system to register both, due to the nature of the BUSY signals used by the trigger system to efficiently process incoming signals from each detector. Therefore, we filter out events where two hits in the same plane come in and are not separated enough in time. After selecting on events where the beam line PID electron trigger fires, we examine and further constrain good analyzable events by requiring exactly one hit in the BH plane, which is shown in figure 4.14. Cases where more than one hit are seen result from randomly coincidental particles; the removal of these events is accounted for in the calculation of the incident particle count. In a similar fashion, triggered events with no BH hits in the plane are accordingly handled, so that the incident particle number accurately represents the events kept for full cross section analysis. In some cases where, even though a PID trigger fires, no hit is detected in the BH plane, this is caused by the differing criteria between what is required for a trigger to fire and what is required for a hit to register. The trigger only requires either the up or down firing of a bar in the plane, but for a hit to register, both up and down must register a signal. For cases where no hit is detected, we adjust the counted triggers in our correction calculation by not counting the particle and also subtracting the counted trigger for that event.

From these conditions where corrections are necessary to accurately calculate the incident particle flux, we can then directly compare the raw number produced by the scaler count in the DAQ system and the number calculated using the correction factor. An example of this comparison can be seen in table 4.1, where the initial raw count N_{scaler} is noticeably reduced due to the correction factor ϵ_{corr} representing the events removed on the condition of not qualifying as analyzable events, illustrated in figures 4.12, 4.13, and 4.14.

CHAPTER 5

Cross Section Ratio Analysis

Analysis was performed on ±210 MeV/c data collected, and differential cross sections as well as cross section ratios were extracted and will be presented here, along with the procedure used for the calculations. It is important to note that these results are preliminary, with the development and refinement of the analysis still in progress within the collaboration. Ongoing efforts and plans will be discussed more in chapter 6. Additionally, all data and results shown are blinded, with a blinding scheme that is explained later in this chapter in section 5.4.

5.1 Cross Section Calculation

In order to extract the scattering cross section from the data collected by detectors in the MUSE apparatus, each component of the cross section must be collected or calculated. The scattering cross section , as noted in section 4.2.3, is

$$\frac{d\sigma}{d\Omega} = \frac{N_{scat}(p,\theta)}{N_{inc}(x\rho)_{target}\Omega_D\epsilon}, \tag{5.1}$$

where $N_{scat}(p,\theta)$ is the number of scattered particles of a specific momentum p at a given scattering angle θ, N_{inc} is the number of incident particles going into the target, $(x\rho)_{target}$ is the target areal density, Ω_D is the detector solid angle, and ϵ is the efficiency factor. Each component is calculated individually before the cross section is determined in analysis.

The calculation of the incident beam particles at the target is discussed in section 4.2.3, where the scaler number of incident particles N_{inc} is corrected based on the fraction of verifiable beam events from the selection criteria for events detected in the BH and GEMs over the number of distributed triggers. For a given momentum, which in this case is 210 MeV/c, scattered events are separated based on the scattering angle calculated during vertex reconstruction. N_{scat}, similarly to N_{inc}, is corrected based on the number of scattered particle

triggers generated as well as the scattering detector efficiencies, shown to be

$$N_{scat} = \frac{N_{scat\ counted}}{\frac{Ntrig\ verified}{Ntrig\ generated}} \frac{1}{\epsilon_{STT}\epsilon_{SPS}}. \tag{5.2}$$

Here, $N_{scat\ counted}$ is the number of measured events produced, $N_{trig\ generated}$ is the number of generated scattering triggers, $N_{trig\ verified}$ is the number of distributed scattering triggers that satisfy scattering conditions, and ϵ_{STT} and ϵ_{SPS} are the STT tracking and SPS detection efficiencies, respectively. For this data set, the STT tracking efficiency was calculated to be 0.95, and the SPS detector efficiency is taken to be 1.

The target areal density $(x\rho)_{target}$ gives the density of protons in the target cell, and it is calculated by

$$(x\rho)_{target} = \frac{\rho N_A t_{target}}{M}, \tag{5.3}$$

where ρ is the liquid hydrogen density, N_A is Avogadro's number 6.022×10^{23} g/mol, t_{target} is the target thickness along the beam, and M is the molar mass of the liquid hydrogen LH_2 ($M = 2.06$ g/mol). The liquid hydrogen density is calculated from the temperature-to-density expression, which is a second-order polynomial fit [49] to the para hydrogen relation between density and temperature [50] (also discussed in section 3.3). The density function, in units of g/cm^2, is

$$\rho(T) = -3.09 \times 10^{-5}T^2 + 9.99 \times 10^{-5}T + 8.09 \times 10^{-2}. \tag{5.4}$$

Using the target temperature data from the Summer 2023 beam time (as shown in figure 3.11), when the 210 MeV/c data being analyzed for this thesis was taken, we calculate the hydrogen density to be $\rho = 0.069936 \pm 0.000021$ g/cm^3. The target thickness along the beam is calculated using GEM tracks projected into the target region. Figure 5.1 shows an example of the target thickness as a function of the GEM track projected into the target for electrons (panel (a)) and muons (panel (b)). For this example, the mean target thickness was found to be 57.2 mm for electrons and 55.4 mm for muons, but it should be noted that the measured thickness of the target varies with beam momentum and particle type.

The detector solid angle Ω_D gives the areal range covered in the scattered particle detection. The expression for the solid angle is

$$\Omega_D = \int_{20}^{100}\int_{-45}^{45} sin\theta d\theta d\phi, \tag{5.5}$$

where the integration over θ gives the horizontal range of the area covered, and the integration over ϕ gives the vertical range covered. The last term of the cross section expression ϵ,

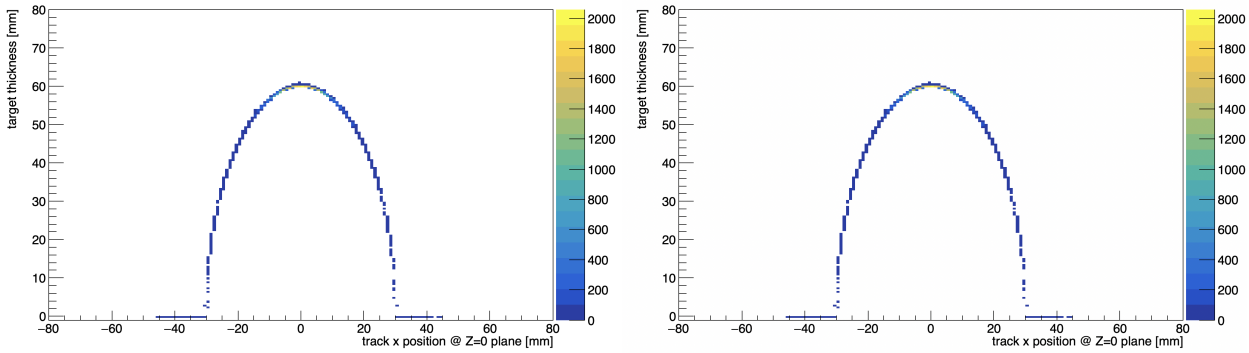

(a) (b)

Figure 5.1: Two examples of the target thickness from the projected GEM track: Panel (a) shows the target thickness for electrons, and the mean target thickness is 57.2 mm. Panel (b) shows the target thickness for muons, and the mean target thickness is 55.4 mm. This is from a (+)210 MeV/c liquid hydrogen scattering run, run 17,800.

which encompasses the efficiency factors, is absorbed into the definitions of the other terms as explained above, and therefore is not calculated as a separate, individual term in the analysis.

5.2 Data and Event Selection

In Summer 2023, the beam time data collection was mainly focused on scattering at ±210 MeV/c momenta, as shown in figures 2.6 and 2.7. I selected the data set for this thesis analysis from the 2023 data; for (+)210 MeV/c there are 80 million full cell and 50 million empty cell events, and for (-)210 MeV/c, there are 50 million full cell and 50 million empty cell events.

With the mixed beam of pions, muons, and electrons, and without a magnetic spectrometer for particle identification, it is important to have a strict prescription for data selection and background removal because there is a significant amount of background. There are selection criteria for each detector that eliminate unwanted data and save qualifying data to be fully analyzed. There are also cuts made on data sets that include only events that meet the cut conditions.

Selection criteria for the detectors that are part of the analysis include

- BH: An event must have one and only one hit detected in each BH plane, and both planes must detect a hit. Additionally, the TOF determined between the two planes must match the PID trigger that is fired in the first plane based on the RF timing.

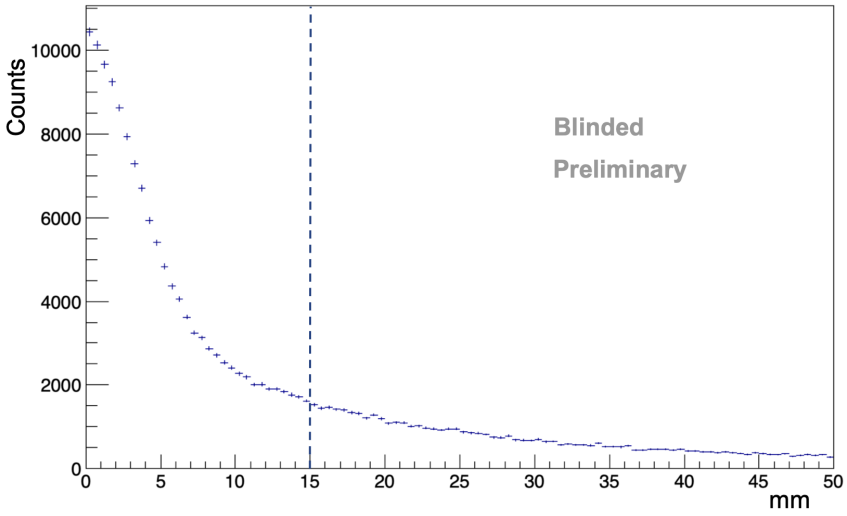

Figure 5.2: Example of the DOCA for vertices constructed for a (+)210 MeV/c run. The vertical dashed line represents the cut placed on the DOCA values.

- GEMs: One and only one GEM track must be formed based on the hits detected, and it must project into the target region through the vacuum chamber entrance window.
- STT: One and only one STT track must be formed, and it must project back into the target region through the vacuum chamber side exit window.
- SPS: The hits seen in the SPS must satisfy the SPS look up table trigger requirements, wherein for the front bar that detects a hit, one of the five bars behind it must also detect a hit to cause the scattered particle trigger to fire.
- VETO: No hit must be detected in the BM, TCPV or veto in order for an event to be included in the scattering data set.
- Calorimeter: The energy level detected in the calorimeter must be less than 40 percent the beam momentum/incident lepton momentum.

In addition to these selection criteria, there are cuts placed on the data to further refine the analyzable events. In the process of vertex reconstruction with the GEM and STT tracks for a given event, the DOCA between the two tracks for a constructed vertex must be smaller than 15 mm, or it does not qualify as an analyzable event. This includes a majority of events, as shown in figure 5.2, while removing cases that are less likely to provide quality scattering events.

Further cuts during the vertex reconstruction include limiting the scattering angle to within the MUSE scattered detector acceptance: $20^\circ \leq \theta \leq 100^\circ$. Since we know our

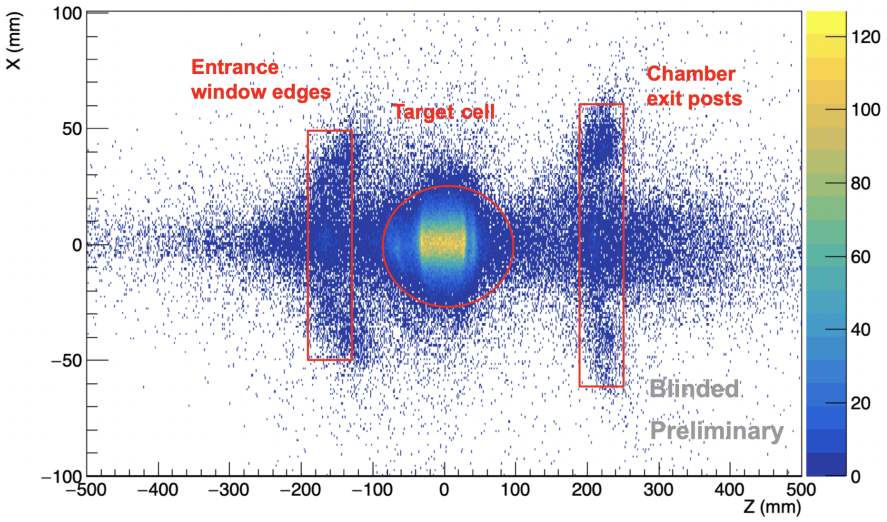

Figure 5.3: Example of reconstructed vertices on the $x - z$ plane in the vacuum chamber region for (+)210 MeV/c run, where the scattering angle and DOCA cuts have been applied.

detectors cannot geometrically reach scattering angles outside this range, we keep only the events where the calculated angle between tracks is within the acceptance range. Beyond scattering angle, there are fiducial cuts made around the target region, to remove events where particles scatter off the entrance windows, exit windows, or downstream exit posts of the vacuum chamber. Figure 5.3 shows the $x - z$ plane of reconstructed vertices after enforcing $20° \leq \theta \leq 100°$, and it is clear to see that, in addition to a concentration of vertices at the target cell, there are also groupings of events at the edge of the entrance window and the downstream exit posts of the vacuum chamber.

As described in section 3.1.1, the target ladder has two Kapton cells: one that is filled with liquid hydrogen during the beam time, and an identical one that remains empty and is used for background subtraction. Figure 5.4 shows the z-coordinate of the reconstructed vertex for both full and empty cell data for (+)210 MeV/c.

Particles are identified with the TOF trigger firing from events detected in the BH, and it is important that the final-state particle ID matches, filtering out decay events and random coincidence events. To accurately reconstruct the timing and travel of particle scattering off the target, the timing of the bars in the BH and SPS must be well-aligned with respect to one another both within the detector and between the detectors. Figure 5.5 shows the electron TOF between BH plane C and BH plane D before and after time alignment. This allows us to align the overall electron TOF to 8 ns within the RF cycle (19.75 ns long), as shown in figure 5.6.

After vertex reconstruction, reaction ID is a key step in the scattering event selection

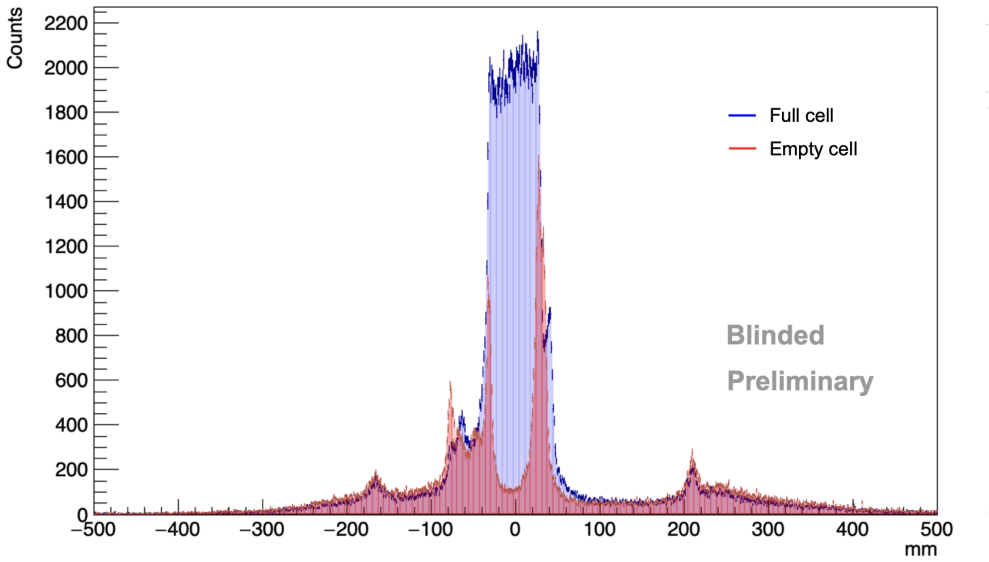

Figure 5.4: z-coordinate of reconstructed vertices for a (+)210 MeV/c run, showing both full and empty cell data. The spikes in the empty cell (red) data at $z = -70$ mm and $z = 40$ mm are a result of scattering off the superinsulated mylar that is wrapped around the target ladder.

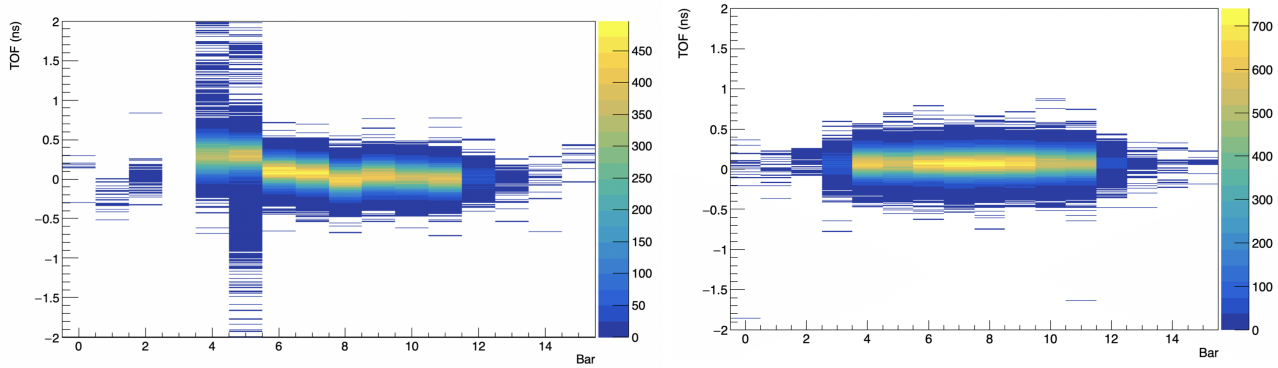

(a) (b)

Figure 5.5: TOF for electrons between BH plane C and plane D. This is from a (+)210 MeV/c liquid hydrogen scattering run; panel (a) shows the RF time before alignment, and panel (b) shows the RF time after alignment. Note that the TOF mean is at 0 ns, which is done to show the offset or necessary correction for each bar.

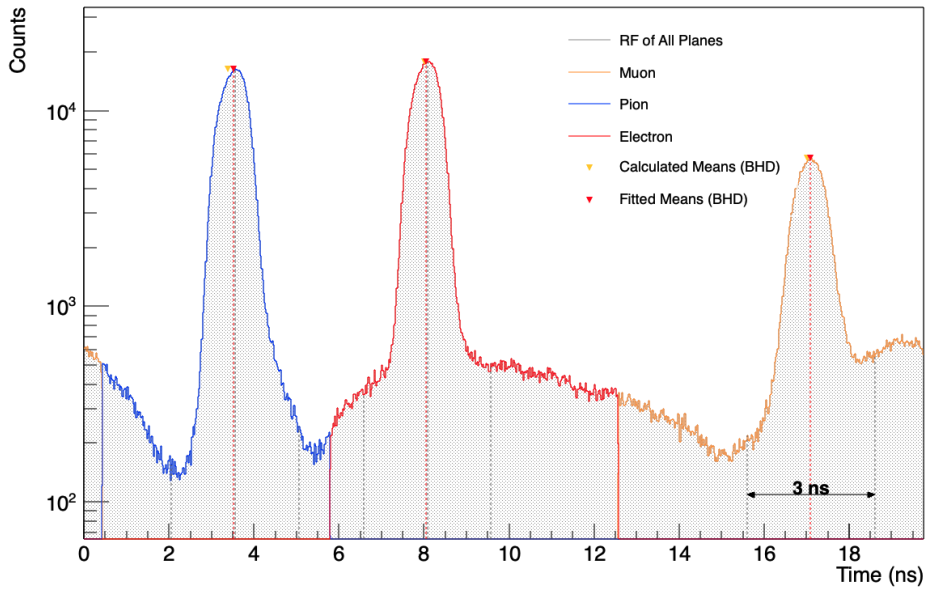

Figure 5.6: RF time of particles with the electron TOF peak aligned at 8 ns.

for analysis. We are able to identify scattering reactions from the outgoing beta, β_{out}. To calculate β_{out}, we need the the total TOF, the ingoing and outgoing distances traveled, and the ingoing and outgoing flight times for those two distances. The ingoing and outgoing distances can be calculated by

$$d_{in} = \sqrt{(x_{vertex} - x_{BH})^2 + (y_{vertex} - y_{BH})^2 + (z_{vertex} - z_{BH})^2},$$
$$d_{out} = \sqrt{(x_{vertex} - x_{SPS})^2 + (y_{vertex} - y_{SPS})^2 + (z_{vertex} - z_{SPS})^2}.$$

Next, we need t_{out} for the β calculation, which is determined by

$$t_{out} = t_{tot} - t_{in} = t_{SPS} - t_{BH} - t_{in} \tag{5.6}$$
$$t_{in} = \frac{d_{in}}{\beta_{in} c} = \frac{d_{in}}{pc^2/\sqrt{p^2 + m^2}}, \tag{5.7}$$

where p and m are the ingoing lepton momentum and mass, respectively. β_{out} can then be calculated by

$$\beta_{out} = \frac{d_{out}}{t_{out}}. \tag{5.8}$$

Figure 5.7 shows the β_{out} of particles as a function of scattering angle θ for electrons (panel a) and muons (panel b). In the case of muons at 210 MeV/c, disentangling the muon events from the muon decay events is trickier due to the overlap in the peaks of these two populations. At 115 MeV/c and 160 MeV/c, the separation between the muon peak and the

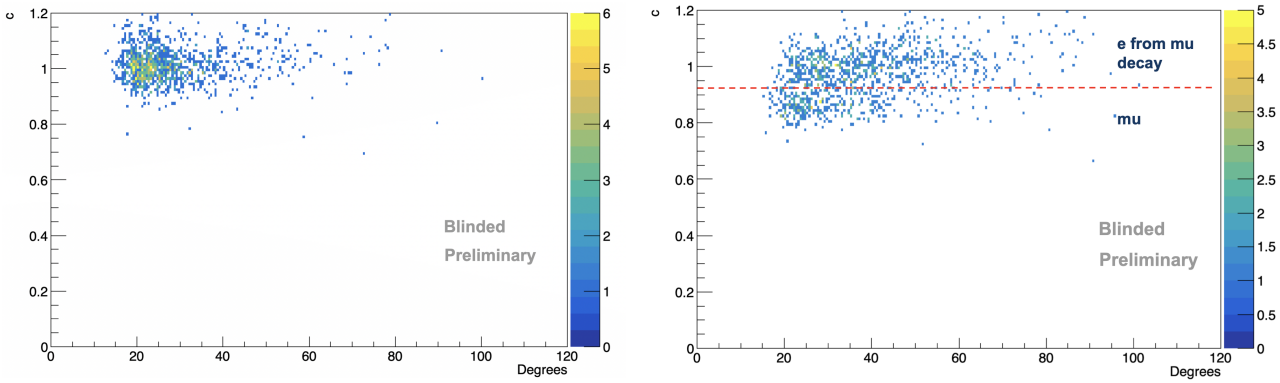

(a) (b)

Figure 5.7: β_{out} vs. scattering angle θ for electrons and muons at (+)210 MeV/c. Panel (a) shows electrons, which we choose to align at $\beta_{out} = 1$ for convenience, which gives clarity to the muon β distribution, shown in panel (b). The red dotted line shows the cut placed to separate the muon scattering events from the muon decay events.

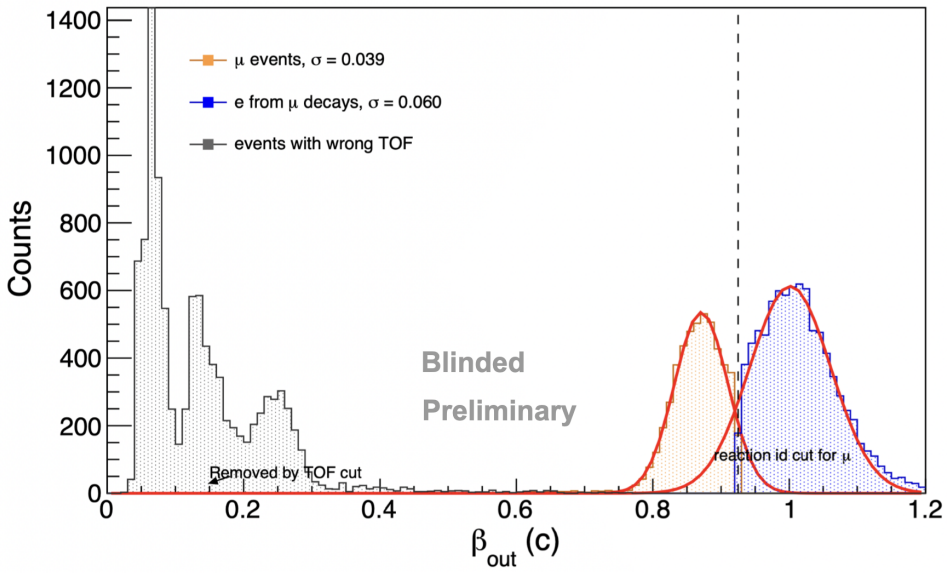

Figure 5.8: β_{out} for muon scattering events and muon decay events at (+)210 MeV/c. The dotted line at $\beta_{out} = 0.925$ shows where the cut is made to exclude the electrons from muon decay events.

electrons from muon decay peak is better than the separation of the peaks at 210 MeV/c, as shown in figure 5.8. The imposed cut removes a majority of the decay events, as well as a small fraction of the muon events, but the tail of the decay events is not completely removable by this cut alone.

5.3 Radiative Corrections

Higher order effects beyond the Born approximation of the scattering cross section contribute to the measured data we use in our cross section calculations, such as bremsstrahlung photon emission, vacuum polarization, and two-photon-exchange effects. The corrections due to these higher-order effects are represented as

$$\frac{d\sigma}{d\Omega} = \left(\frac{d\sigma}{d\Omega}\right)_{Born} (1+\delta), \tag{5.9}$$

with δ encompassing the radiative correction effects. To account for these additional contributions, simulation studies have been performed using MUSE kinematics to study the radiative tail present in the calculated cross section [5]. Figure 5.9 shows the simulation studies done for MUSE for electrons and muons at 161 MeV/c at a scattering angle of $\theta = 60^\circ$ because these values are directly in the middle of our momentum and scattering angle range, respectively. Figure 5.9(b) shows that, for electrons at 161 MeV/c, much of the radiative tail is diminished for energies less than 40 percent of the incident particle momentum. Figure 5.9(c) demonstrates that, for muons at 161 MeV/c, regardless of the resulting energy deposit, the radiative corrections are negligible.

The radiative corrections for the other kinematic settings of MUSE have not been computed yet by the radiative corrections group and are not applied in the results shown in this chapter. However, we can take steps to limit the effects of radiative corrections. The calorimeter detects energy depositions from emitted photons, and, using the simulations shown in figure 5.9, we can enforce a cut condition on the energy values measured in the calorimeter to allow only events where that energy measured is less than $0.4 p_{inc} c$ measuring energy deposited by emitted photons. This will limit the radiative corrections to approximately 10%.

The prescription described above is an intermediate solution to the effects of radiative correction in the measurement of the proton radius. Ultimately, the radiative corrections will be addressed by simulating the radiating events from several event generators, including Elastic Scattering of Electrons and Positrons on Protons (ESEPP) [5]. These simulated events will be factored into the full simulation for scattering events, and the simulation will

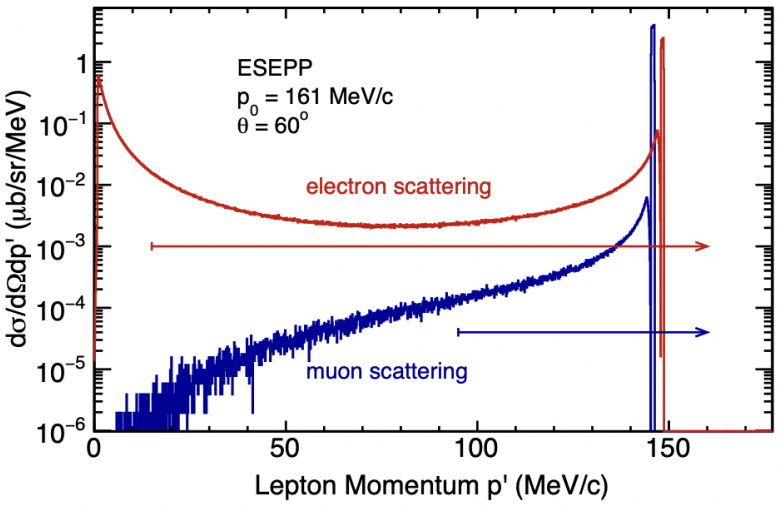

(a)

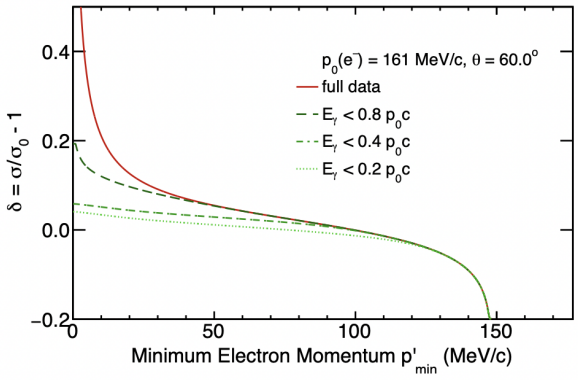

(b)

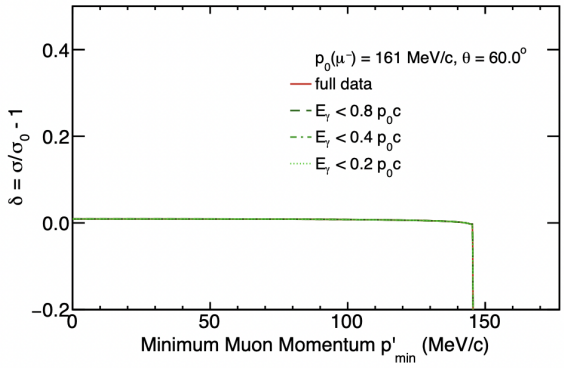

(c)

Figure 5.9: Simulations performed to study the effects of radiative corrections on cross sections extracted for MUSE. Panel (a) shows simulated electron and muon cross sections from MUSE kinematics. The red and blue curves show the electron and muon cross sections at 161 MeV/c, with the red and blue arrows showing the MUSE acceptance for scattered electrons and muons, respectively. Panels (b) and (c) show the simulated radiative correction effects performed by ESEPP event generator to study radiative corrections from MUSE kinematics. The left panel shows the radiative correction δ for electrons for 161 MeV/c beam momentum, and the right panel shows the correction for muons. Figures are from Ref. [5].

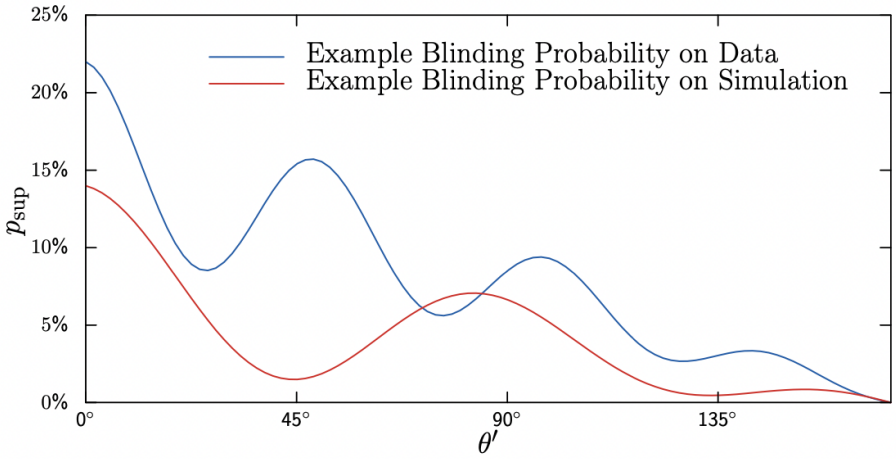

Figure 5.10: An example of the probability distribution of suppressed events for simulation and data as a function of θ' for a set of two arbitrary parameters. For simulation, $A = 0.4$ and $B = 4.1$, and for data, $A = 0.8$ and $B = 7.2$. This figure is from Ref. [6].

be compared to our collected data, where we compare the scattered particle yields for each scattering angle, with an understanding of the contributions of radiative corrections from the simulations.

It is also important to note that radiative corrections will not affect electrons and muons in equal measure. The greater mass of the muon results in far less initial state radiation for muon scattering than for electron scattering, such that the expected contribution of radiative effects for muon scattering as seen from initial simulations is negligible, as shown in figure 5.9.

5.4 Blinding Scheme for MUSE

Due to the contention embedded in the charge radius and its extraction, MUSE implements a blinding scheme in order to avoid biases in the process of analyzing and fitting the data. The blinding scheme being employed involved a random suppression of events at the tracking level, after the individual detector data is processed but before full cross section calculations are done.

For an event where an STT track is constructed, the probability of that event being suppressed is determined by

$$p_{sup} = \frac{0.2}{3}(A_i + 0.3\cos(B_i\theta'))(3.0 - \theta'), \tag{5.10}$$

where θ' is the angle of the constructed track with respect to the beam line axis, and A_i and B_i are fixed-seed pseudo-random generated parameters. Accounting for both parameters for all three particles (e, μ, and π) at all three beam momenta (115, 160, and 210 MeV/c) and both polarities, a total of $2 \times 18 = 36$ sets of parameters are generated in determining the suppression probability.

Once the probability value is calculated for a given reconstructed STT track, the track is then assigned a random number between 0 and 1. If the generated random number is smaller than the the respective probability, then the event is suppressed. Figure 5.10 shows an example of the probability distribution of suppressed events, for two arbitrary parameters A_i and B_i. A detailed discussion of the blinding being used by MUSE is covered in Ref.[6].

5.5 Cross Section Ratio Analysis and Results

The cross section and cross section ratio results are presented in this section in comparison to the theoretical calculations from Preedom and Tegen's scattering cross section expression [51]. The form factors in the expression are calculated using Kelly's form factor parameterization [52]. The lepton-proton scattering cross section in Ref.[51] is defined as

$$\frac{d\sigma}{d\Omega} = \left[\frac{d\sigma}{d\Omega}\right]^{ns} R, \tag{5.11}$$

where the "no-structure" cross section $\left[\frac{d\sigma}{d\Omega}\right]^{ns}$ is given by

$$\left[\frac{d\sigma}{d\Omega}\right]^{ns} = \frac{\alpha^2}{4E^2} \frac{1 - \frac{-q^2}{4EE'}}{\left(\frac{-q^2}{4EE'}\right)^2} \frac{1/d}{1 + \frac{2Ed}{M}\sin^2\frac{\theta}{2} + \frac{E}{M}(1-d)}, \tag{5.12}$$

and R contains the form factor dependence, and is given by

$$R = \frac{G_E^2(q^2) + \eta G_M^2(q^2)}{1+\eta} + \left[2\eta - \frac{m^2}{M^2}\right] G_M^2(q^2) \frac{\frac{-q^2}{4EE'}}{1 - \frac{-q^2}{4EE'}}. \tag{5.13}$$

In equation 5.12, α is the fine structure constant, E and E' are the incident and scattered lepton energies, θ is the scattering angle of the lepton, M is the proton mass, m is the lepton mass, $\eta = \frac{-q^2}{4M^2}$, and d is defined to be

$$d \equiv \left\{ \frac{\left(1 - \frac{m^2}{E^2}\right)}{\left(1 - \frac{m^2}{E^2}\right)} \right\}^{1/2}. \tag{5.14}$$

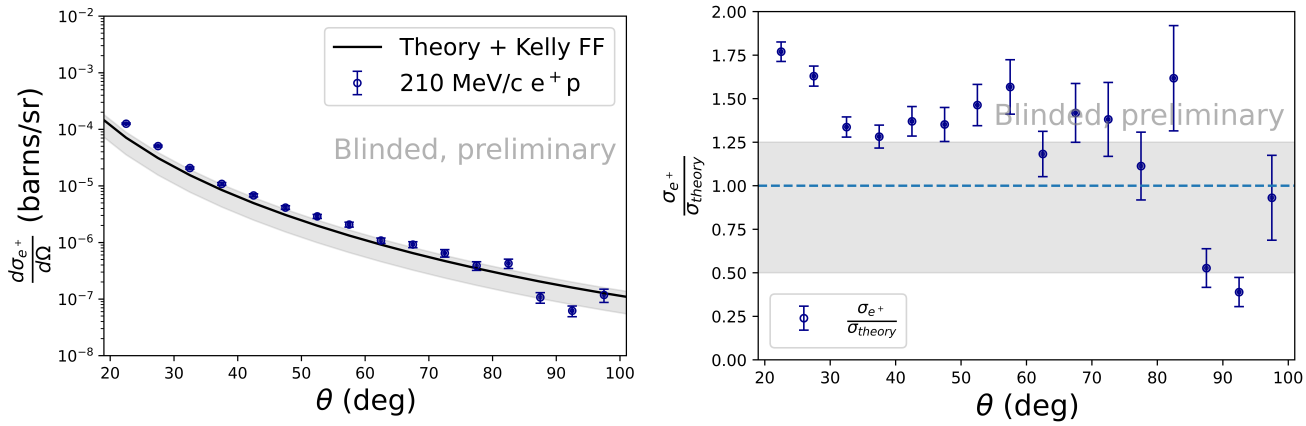

(a) (b)

Figure 5.11: e^+p differential cross section plotted as a function of scattering angle θ at 210 MeV/c. The gray shaded region in both plots represents the cumulative uncertainties from systematic uncertainty (estimated to be 25% above and below) and blinding uncertainty (up to 25% below the theory). Panel (a) shows the calculated cross section values compared to the theory curve obtained from equations 5.11 - 5.13. The data points are in five degree bins in accordance with the current resolution capabilities for the 2023 data set. Panel (b) shows the ratio of data to theory shown in the left panel. The horizontal line at $y = 1$ acts as a reference for the difference between the data and theory.

In this prescription, G_E and G_M are the Sachs electric and magnetic form factors as a function of q^2, and q^2 is given by

$$q^2 = -4EE'\sin^2\frac{\theta}{2}\left\{\frac{\left(1-\frac{m^2}{E^2}\right)}{\left(1-\frac{m^2}{E^2}\right)}\right\}^{1/2} + 2m^2 - 2EE'\left[1-\left\{\frac{\left(1-\frac{m^2}{E^2}\right)}{\left(1-\frac{m^2}{E^2}\right)}\right\}^{1/2}\right]. \tag{5.15}$$

For the case where lepton mass is neglected, q^2 simplifies to $-4EE'\sin^2\frac{\theta}{2}$, equation 5.12 reduces to the Mott cross section, shown in equation 1.3, and equation 5.11 becomes equation 1.2. This set of equations is used to calculate the theoretical values for the electron and muon scattering cross sections that are compared to the data shown in this section.

With the analysis described in this chapter and chapter 4, we are able to obtain and present preliminary scattering cross section results. Figure 5.11 shows the e^+p scattering cross section for 210 MeV/c data. Since the number of total events for full and empty cell scattering data were not equal (80 million full cell and 50 million empty cell), the empty cell data is normalized using the ratio of incident particles from full cell data to empty cell data. All of the cross section data is plotted in five-degree bins. Figure 5.12 shows the 210 MeV/c e^-p scattering cross sections, where panel (a) shows the cross section values with the theory

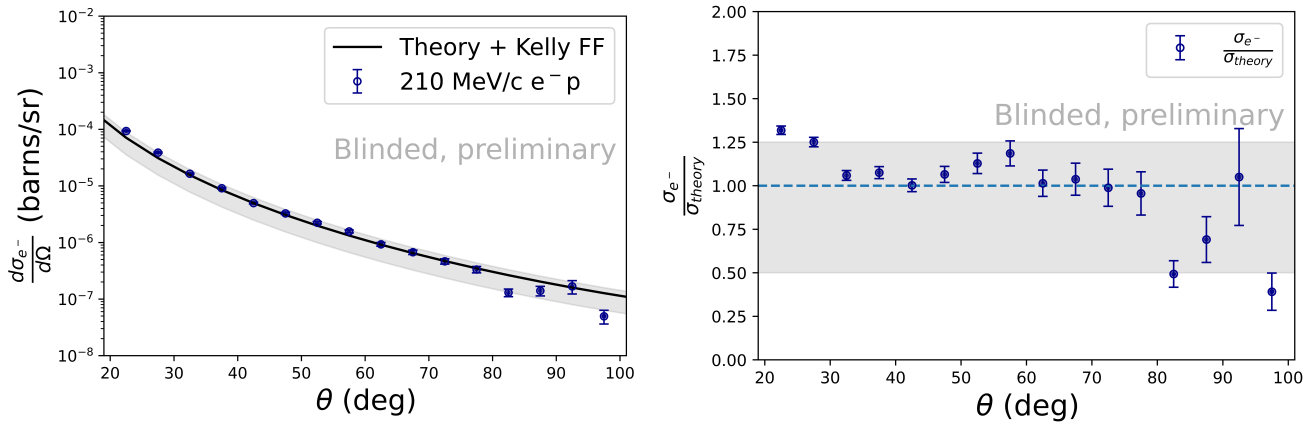

(a) (b)

Figure 5.12: e^-p differential cross section plotted as a function of scattering angle θ at 210 MeV/c. The data points are in five degree bins in accordance with the current resolution capabilities for the 2023 data set. The gray shaded region in both plots represents the cumulative uncertainties from systematic uncertainty (estimated to be 25% above and below) and blinding uncertainty (up to 25% below the theory). Panel (a) shows the differential cross section data plotted with the theory curve, and panel (b) shows the ratio of data to theory shown in the left panel. The horizontal line at $y = 1$ acts as a reference for the difference between the data and theory.

curve and panel (b) plots the ratio of data to theory.

As shown in figure 5.10, the blinding effects can be up to 25%, and so the blinded data may not fall neatly in line with the theory. Additionally, more statistics at higher scattering angles will improve the precision on these calculated cross sections, whose error bars are much larger at high scattering angles than at low scattering angles, as seen in panel (b) of figures 5.11 and 5.12. The data shown here represents less than 20% of the total statistics that will be collected by MUSE for 210 MeV/c data.

Two-photon-exchange effects can be probed through the ratio of opposite polarity cross sections, as described in equation 1.8, and is one of the physics goals of MUSE with the data we are able to collect. Although two-photon-exchange effects are not the focus of this thesis, it is advantageous to produce the cross section ratio e^+/e^- and do an initial comparison to what we would expect. Figure 5.13 shows the ratio of the e^+p to e^-p scattering cross sections. The band of uncertainty is different here in the ratio plot from the cross sections shown in figures 5.11 and 5.12 because, while the blinding can only lower the absolute cross section, taking the ratio of the two cross sections allows the blinding effects to also increase the resulting value, giving us up to ±25%. Additionally, the cross section ratio causes a significant portion of the systematic uncertainties to cancel out, so the effects of these

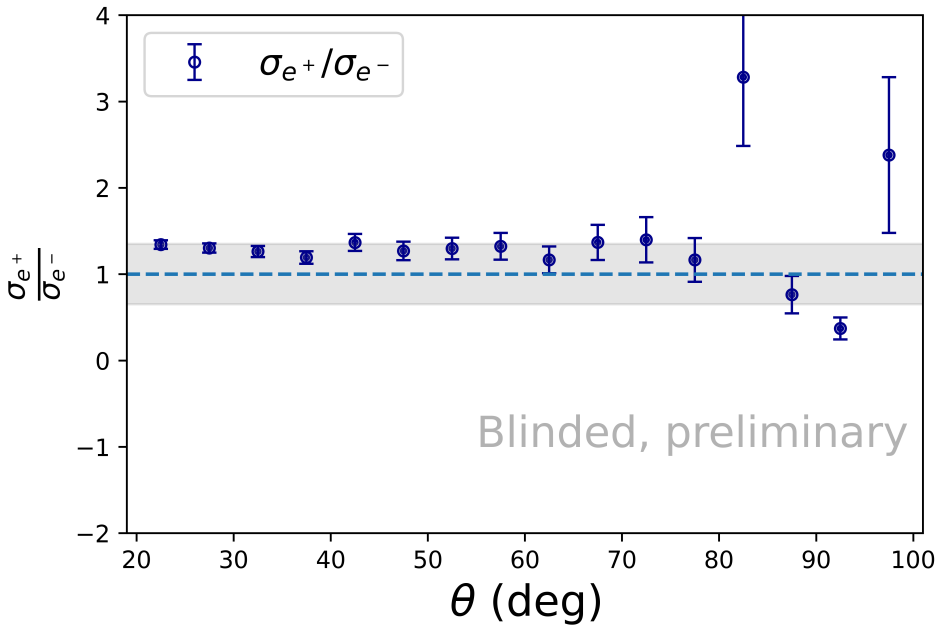

Figure 5.13: e^+/e^- cross section ratio as a function of scattering angle θ at 210 MeV/c. The data is plotted in five degree bins. The gray shaded region represents the uncertainty band for the data, which is ± 35% of the expected value.

uncertainties decreases to ±10%, giving us a cumulative ±35% for the uncertainty band for all ratio plots.

Of the beam momenta that MUSE operates with, 210 MeV/c has the highest percentage of muons, while 115 MeV/c is strongly dominated by electrons. However, 210 MeV/c is also the momentum at which it is most difficult to untangle muon scattering events from the muon decays, as discussed in section 5.2. As our analysis and simulations develop to comprehensively address the separation of these events, the decay cut enforced allows us to take a preliminary look at the muon-proton scattering cross section. Figure 5.14 shows the 210 MeV/c μ^+p scattering cross sections, both compared directly to the theory curve in panel (a) and divided over the theory.

The μ^-p scattering cross section at 210 MeV/c had a more severe overlap of the population of muon scattering events and muon decay events, resulting in increased difficulty when accurately categorizing these events for the cross section calculation. Figure 5.15 shows the β_{out} for muon scattering and decay events, where it is clear that there is a large overlap of the β_{out} values for these two populations. The overlap is to the extent that a cut, as was done for μ^+p scattering, does not suffice to separate the muon scattering events, and so the calculated cross sections do not accurately represent the proper cross sections. Additionally, more involved background removal is required to produce the μ^-p cross section results.

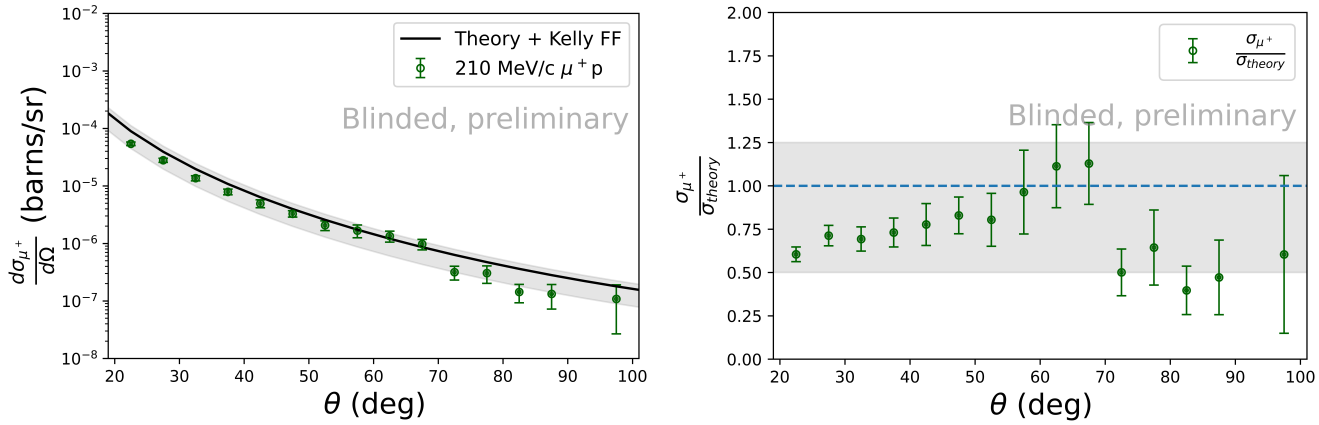

(a) (b)

Figure 5.14: μ^+p differential cross section vs. scattering angle θ at 210 MeV/c. The gray shaded region in both plots represents the cumulative uncertainties from systematic uncertainty (estimated to be 25% above and below) and blinding uncertainty (up to 25% below the theory). Panel (a) shows the muon scattering cross section plotted with the theory curve, and panel (b) shows the data to theory ratio plotted of the same data, with the dashed line at $y = 1$ representing agreement between the data and theory.

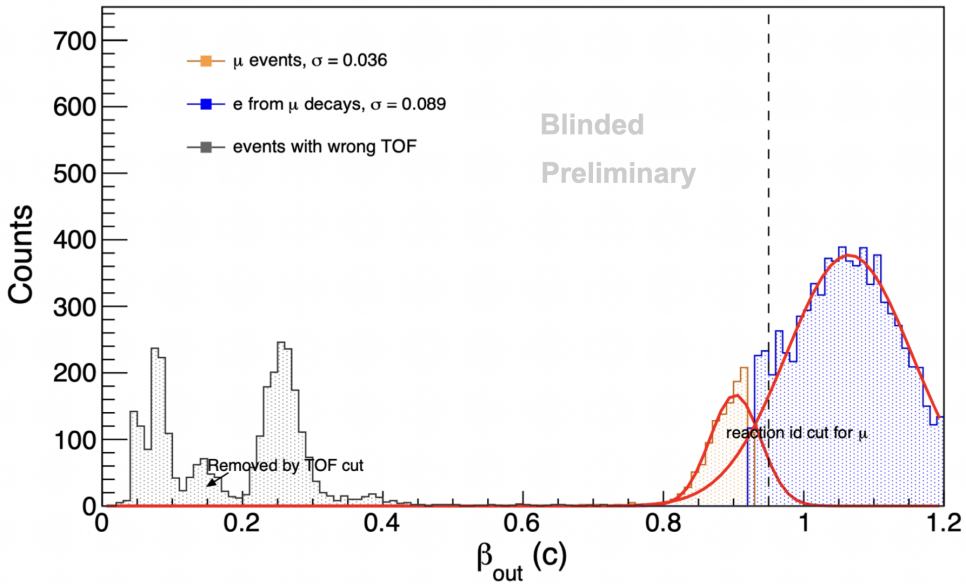

Figure 5.15: β_{out} for (-)210 MeV/c muon scattering and decay events. The dashed line shows where the cut was made for (+)210 MeV/c, where the two peaks were more well-separated.

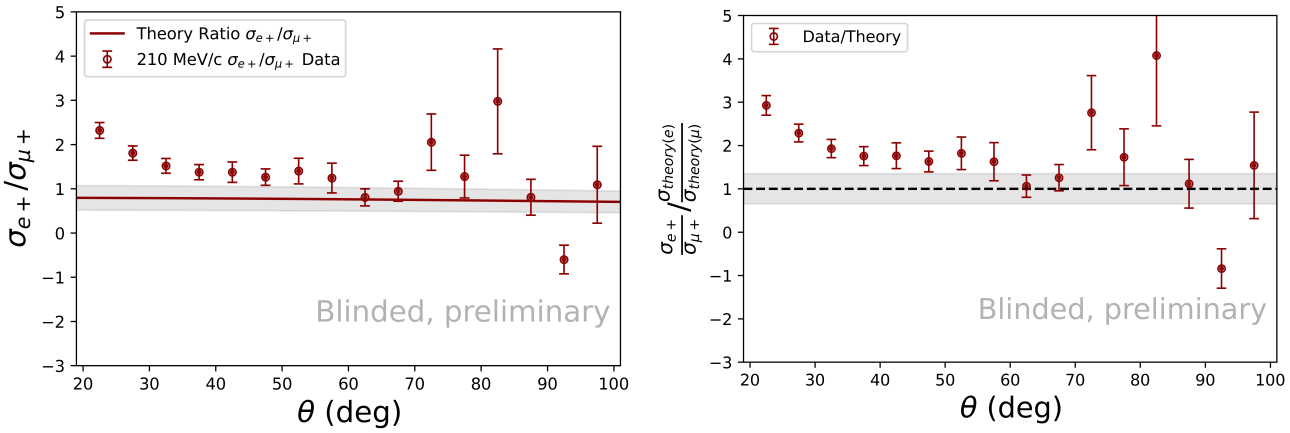

(a) (b)

Figure 5.16: e^+p to μ^+p differential cross section ratio vs. scattering angle θ at 210 MeV/c. The gray shaded region represents the uncertainty band for the data, which is ± 35% of the expected value. Panel (a) shows the ratio of electron scattering cross section to muon scattering cross section, with the red line being the ratio of the theoretical electron scattering cross section to the theoretical muon scattering cross section. Panel (b) shows the ratio of the data ratio to the theory ratio, with the dashed line at $y = 1$ acting as a reference for the difference between data and theory.

Figure 5.16 shows the 210 MeV/c e^+/μ^+ scattering cross section ratios, compared with the ratio of theoretical cross sections in panel (a). Panel (b) shows the data ratio divided by the theory ratio. Although many systematic uncertainties are canceled out in the cross section ratio, each cross section data set is blinded individually, and the blinding effects do not cancel out. The blinding effect could increase one cross section value while decreasing another, so the shape of the presented data does not necessarily inform the true behavior.

Though the results presented are blinded and preliminary, we can perform a χ^2 test in order to compare the data and theory for the cross section ratio, to gain a quantitative understanding of the differences between data and theory. Table 5.1 shows the results of the χ^2 test with a 95% confidence interval (CI) for the cross section data and ratios presented. This also gives us an insight into the agreement of data with theory, with the effects of blinding factored in.

To calculate the χ^2 while accounting for the blinding effects, we adjust the standard χ^2 expression to get

$$\chi^2 = \frac{(O_i - E_i)^2}{(\sigma_i + 0.25O_i)^2}, \tag{5.16}$$

where O_i is the observed value, E_i is the expected value, and σ_i is the standard deviation of the observed value. The addition of $0.25O_i$ to the standard deviation encompasses the

Data Set	ν	z_l	z_u	χ^2	χ^2_ν
e^+p	16	7.96	26.3	26.2	1.64
e^-p	16	7.96	26.3	18.3	1.14
e^+/e^-	16	7.96	26.3	16.7	1.04
μ^+p	16	7.96	26.3	41.3	2.58
$e^+/\ \mu^+$	16	7.96	26.3	24.5	1.53

Table 5.1: Table showing χ^2 values for the cross section data sets shown in this section, where ν is the degrees of freedom for the data set, z_l and z_u are the lower and upper bounds for a 95% CI.

blinding effect of up to 25%, and we use this to produce the χ^2 values in table 5.1.

The 210 MeV/c e^+p scattering cross section produces a χ^2 value of 26.2, which falls within the 95% CI, so we can say with 95% confidence that the difference between the data and theory is not significant. Likewise, the e^-p scattering cross section χ^2 is 18.3 and lands within the 95% CI, as well as the χ^2 value for the e^+/e^- cross section ratio, which is 16.7.

The χ^2_ν is the reduced chi-square, given by $\frac{\chi^2}{\nu}$ and provides a goodness-of-fit test for the data. The χ^2_ν for e^-p scattering cross section and the e^+/e^- ratio are near unity, indicating that the theory is a good fit for the data. The χ^2_ν for e^+p scattering cross section χ^2_ν is 1.64, indicating that, while the difference between data and theory is not significant, the uncertainty may be underestimated.

For the 210 MeV/c μ^+p scattering cross section, the χ^2 value is 2.58 and falls outside of the 95% CI range. There are a couple of potential reasons for this, including:

- Effects of muon decay events are not fully removed, pulling the data further from the expected values.

- Systematic uncertainties that are unaccounted for in the current analysis procedure. This is supported by the μ^+p/e^+p χ^2 value being within the 95% CI, where the ratio would have caused some systematic uncertainties to cancel out.

The χ^2_ν for the μ^+p scattering cross section is 2.58, and this could be a result of the model being a poor fit for the data, or the error bars are underestimated for the data. With the continued development of the analysis framework and the simulations, we will progress on gaining insight into the background subtraction necessary to extract the μ^-p scattering cross section. These challenges are part of the reason why a high-precision μp scattering cross section result is still a missing piece in the proton radius puzzle.

Finally, the 210 MeV/c e^+p to μ^+p cross section ratio produces a χ^2 value of 24.5 that falls within the 95% CI, as seen in table 5.1. This shows that the difference between the data

and theory for the cross section ratio is not significant. The $\mu^+ p$ χ^2_ν is 1.53, which indicates that the error bars may be too small for the data presented.

CHAPTER 6

Conclusions and Outlook

The analysis and results presented in this thesis are merely a part of the multi-faceted ongoing efforts of the MUSE collaboration in its quest to measure the proton radius through elastic electron-proton scattering and muon-proton scattering, examine two-photon-exchange effects, extract the electric and magnetic form factors from measured cross sections, and test lepton universality between electron and muon interactions with protons. MUSE has successfully collected and analyzed data, working to both improve the experimental detector configuration as well as refine the analysis techniques and reach the necessary precision for the desired physics measurements.

The liquid hydrogen target for MUSE was built with great care and precision in order to allow for the collection of this scattering data. The target has consistently operated very reliably since its commissioning in 2018, even through excessive temperatures and humidity in the experimental hall and service interruptions within the hall. The stability of the target's operation during data-taking provides an incredibly consistent density ($\mathcal{O}(0.2\%)$) for scattering, contributing to reaching the necessary level of precision for this measurement.

Although the cross section and cross section ratio results shown are preliminary and are not to the point of robustly testing lepton universality, they act as a demonstration of the progress and ability that MUSE has gained throughout its running times. As mentioned in section 5.2, one of the main difficulties in analyzing the 210 MeV/c data is in the process of untangling the muon scattering events from the cases where the muon decays to an electron within the MUSE experimental set up; simulation is being developed that will allow us to more accurately separate out the muon scattering events from the muon decay events. Additionally, radiative corrections are currently handled with a cut condition on the energy levels detected in the calorimeter, depending on the momentum. There is also simulation in development that will handle this effect in a more nuanced way, allowing us to keep more of the collected data and more comprehensively navigate the radiative corrections.

The χ^2 tests for a 95% confidence level were performed on the data results and showed that for the e^+p, e^-p, e^+/e^- and the e^+/μ^+ cross sections and cross section ratios are in

agreement with the theory, when the error bars are artificially increased to include the effects of blinding. The χ^2 value for the $\mu_+ p$ scattering cross section results was not in agreement with the 95% CI, and there are several possible explanations for this lack of agreement. Decay events could still be contaminating the scattering event data, such that the calculation could be affected. It is also possible that systematic uncertainties that are not currently accounted for are changing the value away from the theoretical predictions. As we continue taking and analyzing data, we can gain a better understanding of the factors contributing to the $\mu^+ p$ scattering, as well as fully untangle the $\mu^- p$ scattering and produce cross section results for this data too.

MUSE is collecting data for five months in 2024 and plans to have another beam time in 2025, in order to greatly increase the number of scattering events and decrease the error bars on extracted cross sections. The 2024 beam time will focus on collecting scattering data at ± 115 MeV/c to gather higher statistical precision of muon scattering because of the domination of electrons in the beam at this momentum. We will continue improving our methods and analysis, hoping to produce exciting new physics in the next 2-3 years.

Appendix A

Target Requirements with Creare

When working with Creare to construct the target ladder system, two lists of hard and soft requirements were used to design and build a system that met all of the needs for MUSE data taking and physics goals. The two lists of requirements are outlined below:

MUSE LH_2 Target Hard Requirements

1. Entrance window centerline and target center position shall be 1.5 m above floor.
2. The vacuum chamber shall be adjustable vertically $\pm$ 2 cm and in the horizontal plane $\pm$ 5 mm in two directions.
3. Vacuum chamber shall be removable from the base with locating pins between chamber support and chamber for repeatable positioning.
4. Target system feet shall have an O.D. less than 75 cm.
5. Vacuum chamber O.D. shall be less than or equal to 49 cm.
6. Target clearance zone shall limit vacuum chamber diameter to below 50 cm for up to 2 m above beam height.
7. Beam entrance window shall be less than or equal to 200 μm and have I.D. = 7 cm clear aperture.
8. Vacuum chamber shall include 4 targets (from top to bottom): 1 LH_2, 1 GH_2, 1 C target, 1 empty position.
9. LH_2 target cell shall be an upright cylinder (coffee can) with end caps not in beam.
10. LH_2 target cell shall have O.D. = 6 cm, height = 8 cm plus end caps.

11. LH_2 target cell wall thickness shall be less than or equal to 120 μm

12. GH_2 target shall be built to be as dimensionally equal to the LH_2 target as possible.

13. There shall be at least one level-sensing resistor in each cell - at the top, inside the cup to know that the cell is full.

14. There shall be one heater at the bottom of each cell.

15. There shall be one temperature sensor at the bottom of each cell.

16. There shall be redundant temperature sensors and heaters on the copper condenser.

17. Carbon target attachment shall support a replaceable 6 cm x 6 cm x 0.5 mm thick C target or similarly sized optics target.

18. "Empty" target (no material) center position shall be 7 cm below C target center.

19. Exit windows shall be 10.0 - 24.5 cm from the cell vertical axis (aim for 14 cm) and shall be less than or equal to 200 μm thickness.

20. Scattered particle exit window geometry shall be $20^\circ < \theta < 100^\circ$, and $-20^\circ < \theta < -100^\circ$, $\phi = \pm 45^\circ$ from target center position.

21. A beam exit window in line with the entrance window shall match the height of the scattered particle window and be 7 cm wide.

22. Vacuum chamber system shall include covers for all thin windows. Engineering effort should be taken to design covers to minimize or prevent possibility of damage to the windows as part of cover installation and removal.

23. Vacuum chamber system shall use metric sizes/components and Swiss voltage standards.

24. Creare shall deliver 2 sets of copies of windows and cell ladder system as spares.

25. Creare shall provide survey markers that allow to determine cell position with respect to vacuum chamber to 0.1mm (z). Number, style and location TBD.

26. Creare shall provide survey markers (3) on vacuum chamber. Style and locations TBD.

MUSE LH_2 Target Soft Requirements

1. Both LH_2 and GH_2 targets will have MLI (superinsulation) covering. Number of layers TBD.

2. If possible, there may be one level-sensing resistor inside each cell - at the bottom, inside the cup to watch as we begin to accumulate liquid.

3. If possible, exit window will be continuous: $\theta = \pm 110\,\mathrm{deg}$, $\phi = \pm 45\,\mathrm{deg}$ from cell center position, and the thickness less than or equal to 120 μm.

4. Cooldown time (from warm cell to LH_2 cell filled) will be ≤ 1 day.

5. If possible, Creare will provide a N_2 baffle to cryopump chamber.

6. Creare will provide camera view of target position/motion (maybe use mirrors & ports or camera inside to avoid ports or optical fibers & lens).

7. Vacuum chamber will be constructed of material (Al, SS, other?) which minimizes thickness while maintaining structural integrity with large window. Mass near targets and scattering zones should be kept as small as possible, with more mass allowed at greater distances.

Appendix B

Target Ladders Timeline

This timeline details the survey and work for the three target ladders since 2019. The ladders are numbered 1 through 3: ladder 1 is the leftmost orange cylinder in each set of three, ladder 2 is in the center, and ladder 3 is the rightmost cylinder.

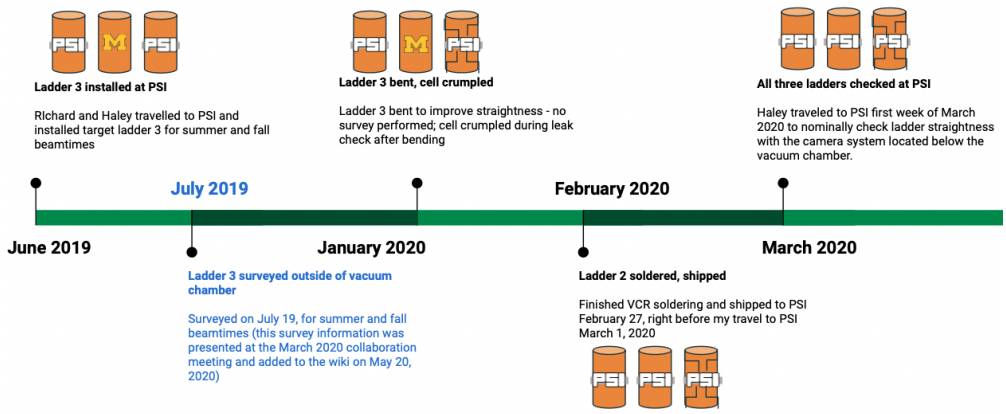

Figure B.1: Timeline from June 2019 - March 2020

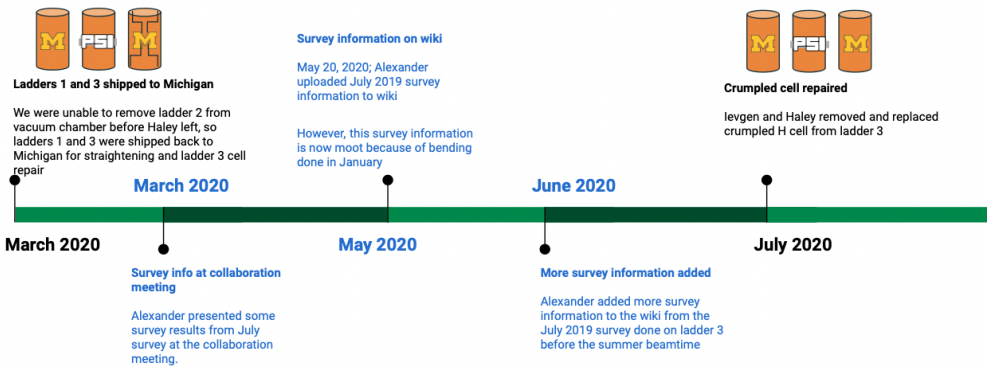

Figure B.2: Timeline from March 2020 - July 2020

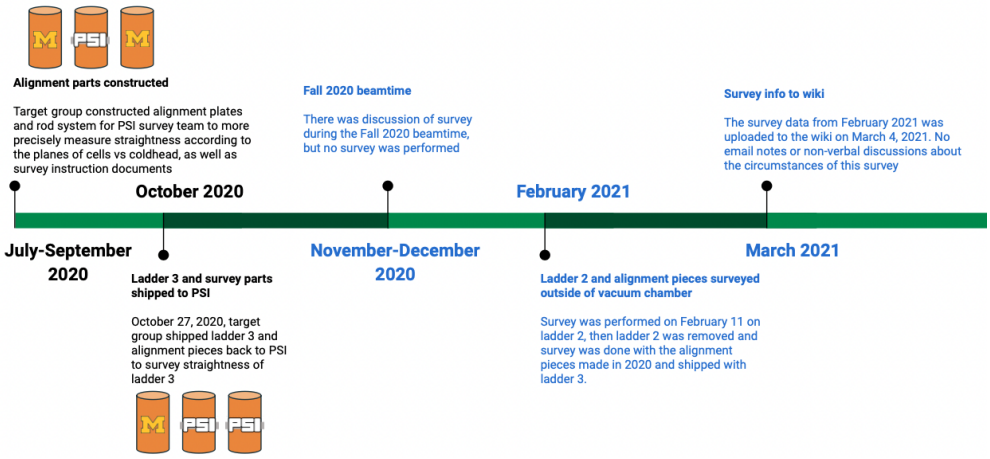

Figure B.3: Timeline from July 2020 - March 2021

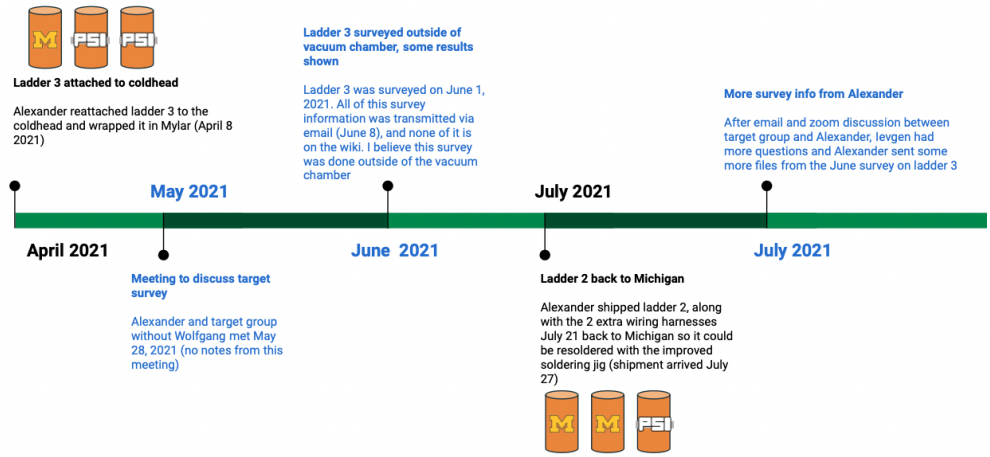

Figure B.4: Timeline from April 2021 - July 2021

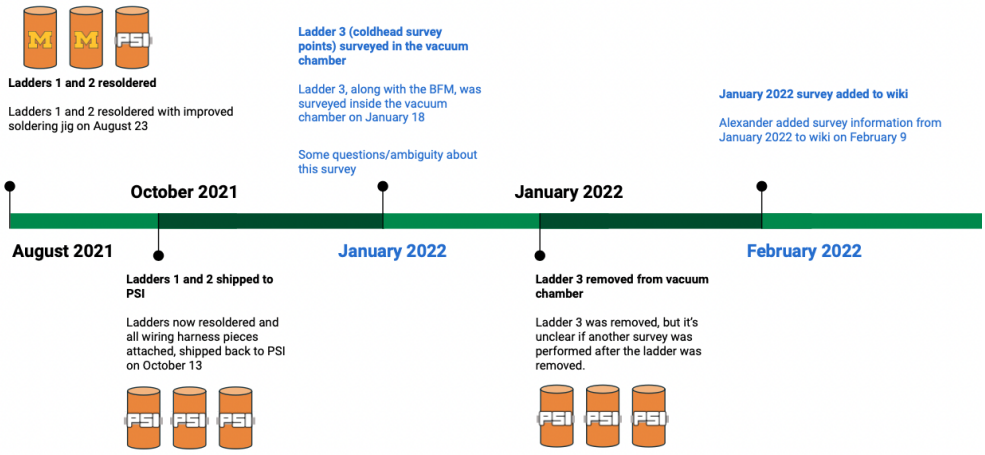

Figure B.5: Timeline from August 2021 - February 2022

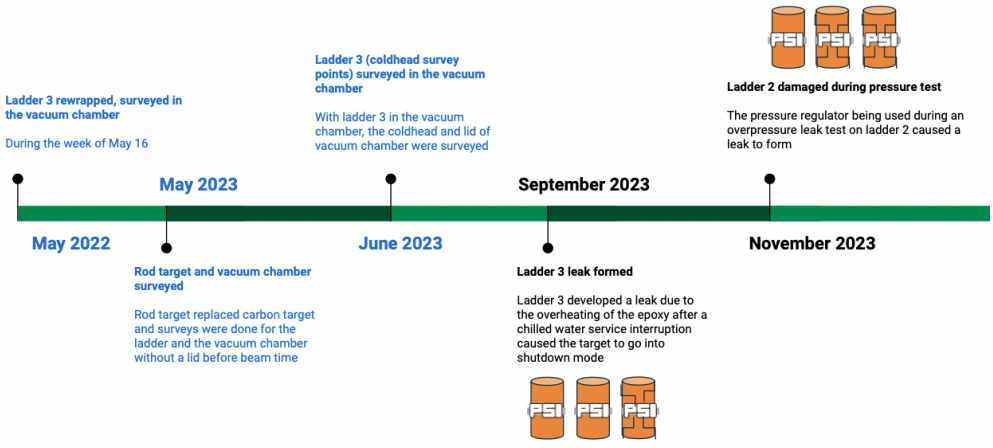

Figure B.6: Timeline from May 2022 - November 2023

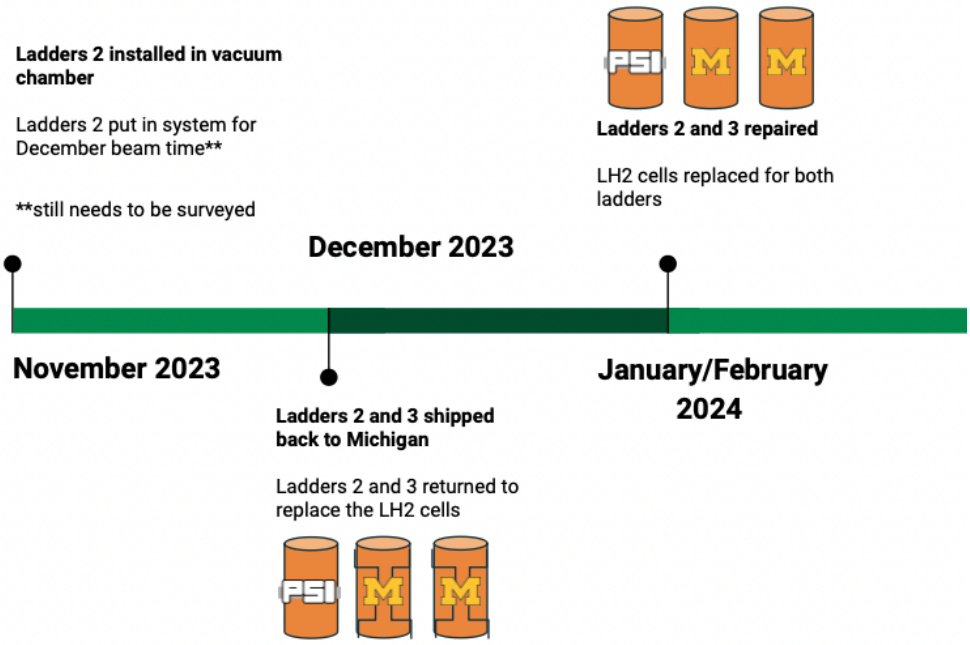

Figure B.7: Timeline from November 2023 - January 2024

BIBLIOGRAPHY

[1] Randolf Pohl, Ronald Gilman, Gerald A. Miller, and Krzysztof Pachucki. Muonic hydrogen and the proton radius puzzle. *Annu. Rev. Nucl. Sci.*, 63, 2013.

[2] E. Cline *et al.* Characterization of Muon and Electron Beams in the Paul Scherrer Institute PiM1 Channel for the MUSE Experiment. *Physical Review C.*, 105, 2022.

[3] R. Gilman *et al.* Technical Design Report for the Paul Scherrer Institute Experiment R-12-01.1: Studying the Proton "Radius" Puzzle with μp Elastic Scattering. *arXiv: Physics - Instrumentation and Detectors*, 2017.

[4] T. Rostomyan *et al.* Timing detectors with SiPM read-out for the MUSE experiment at PSI. *Nucl. Instrum. Methods A*, 986, 2021.

[5] Lin Li *et al.* Instrumental uncertainties in radiative corrections for the muse experiment. *unpublished*, 2024.

[6] J. C. Bernauer *et al.* Blinding for precision scattering experiments: The MUSE approach as a case study, 2023.

[7] E. Rutherford. LIV. Collision of α particles with light atoms. IV. An anomalous effect in nitrogen, 1919.

[8] J. D. Cockcroft and E. T. S. Walton. Artificial Production of Fast Protons. *Nature*, 129, 1932.

[9] M. N. Rosenbluth. High Energy Elastic Scattering of Electrons on Protons. *Physical Review*, 1950.

[10] Robert Hofstadter. Electron Scattering and Nuclear Structure. *Reviews of Modern Physics*, 28, 1956.

[11] P. Lehmann, R. Taylor, and Richard Wilson. Electron-Proton Scattering at Low Momentum Transfers. *Physical Review*, 126, 1962.

[12] L. N. Hand, D. G. Miller, and Richard Wilson. Electric and Magnetic Form Factors of the Nucleon. *Reviews of Modern Physics*, 35, 1963.

[13] J. J. Murphy II, Y. M. Shin, and D. M. Skopik. Proton Form Factor from 0.15 to 0.79 fm^{-2}. *Physical Review C*, 9, 1974.

[14] G. G. Simon, Ch. Schmitt, F. Borkowski, and V. H. Walther. Absolute electron-proton cross sections at low momentum transfer measured with a high pressure gas target system. *Nuclear Physics A*, 333, 1980.

[15] R. G. Sachs. High-Energy Behavior of Nucleon Electromagnetic Form Factors. *Physical Review*, 126, 1962.

[16] J. Bernauer *et al.* The electric and magnetic form factors of the proton. *Physical Review C*, 90, 2014.

[17] Barry N. Taylor Peter J. Mohr and David B. Newell. CODATA recommended values of the fundamental physical constants: 2006. *Reviews of Modern Physics*, 80, 2008.

[18] Peter J. Mohr, Barry N. Taylor, and David B. Newell. CODATA Recommended Values of the Fundamental Physical Constants: 2010. *Reviews of Modern Physics*, 84, 2012.

[19] R. Pohl *et al.* The size of the proton. *Nature*, 466, 2010.

[20] Aldo Antognini *et al.* Proton Structure from the Measurement of 2S-2P Transition Frequencies of Muonic Hydrogen. *Annu. Rev. Nucl. Sci.*, 63, 2013.

[21] J.C. Bernauer *et al.* High-precision determination of the electric and magnetic form factors of the proton. *AIP Conf. Proc.*, 1388, 2011.

[22] X. Zhan *et al.* High Precision Measurement of the Proton Elastic Form Factor Ratio $\mu_p G_E/G_M$ at low Q^2. *Physics Letters B*, 705(1–2):59–64, November 2011.

[23] W. Xiong *et al.* A small proton charge radius from an electron-proton scattering experiment. *Nature*, 575, 2019.

[24] Axel Beyer *et al.* The Rydberg constant and proton size from atomic hydrogen. *Science*, 358, 2017.

[25] N. Bezginov, T. Valdez, M. Horbatsch, A. Marsman, A. C. Vutha, and E. A. Hessels. A measurement of the atomic hydrogen Lamb shift and the proton charge radius. *Science*, 365, 2019.

[26] H. Fleurbaey *et al.* New measurement of the 1S3S transition frequency of hydrogen: contribution to the proton charge radius puzzle. *Physical Review Letters*, 120, 2018.

[27] Alexey Grinin *et al.* Two-photon frequency comb spectroscopy of atomic hydrogen. *Science*, 320, 2020.

[28] A. D. Brandt, S. F. Cooper, C. Rasor, Z. Burkley, A. Matveev, and D. C. Yost. Measurement of the $2S_{1/2} - 8D_{5/2}$ Transition in Hydrogen. *Phys. Rev. Lett.*, 128, 2022.

[29] Ingo Sick. Proton charge radius from electron scattering, 2018.

[30] J. M. Alarcón, D. W. Higinbotham, C. Weiss, and Zhihong Ye. Proton charge radius extraction from electron scattering data using dispersively improved chiral effective field theory. *Phys. Rev. C*, 99, 2019.

[31] Peter J. Mohr, David B. Newell, and Barry N. Taylor. CODATA recommended values of the fundamental physical constants: 2014. *Reviews of Modern Physics*, 88, 2016.

[32] Eite Tiesinga, Peter Mohr, David Newell, and Barry Taylor. CODATA Recommended Values of the Fundamental Physical Constants: 2018. *Review of Modern Physics*, 93, 2021.

[33] A. Gasparian *et al.* PRad-II: A New Upgraded High Precision Measurement of the Proton Charge Radius. *arXiv: Physics - Nuclear Experiment*, 2022.

[34] B. Adams *et al.* COMPASS++/AMBER: Proposal for Measurements at the M2 beamline of the CERN SPS Phase-1: 2022-2024. Technical report, CERN, Geneva, 2019.

[35] Sören Schlimme, Kurt Aulenbacher, Sebastian Baunack, Niklaus Berger, Achim Denig, Luca Doria, Alfons Khoukaz, Harald Merkel, Concettina Sfienti, and Michaela Thiel. The MESA physics program, 2024.

[36] Toshimi Suda. Low-energy electron scattering facilities in Japan. *Journal of Physics: Conference Series*, 2391, dec 2022.

[37] M. K. Jones *et al.* The ratio of proton's electric to magnetic form factors measured by polarization transfer. *Physical Review Letters*, 84, 2000.

[38] J. Arrington, P. G. Blunden, and W. Melnitchouk. Review of two-photon exchange in electron scattering. *Progress in Particle and Nuclear Physics*, 66, 2011.

[39] J. Arrington. How well do we know the electromagnetic form factors of the proton? *Physical Review C*, 68, 2003.

[40] R. Aaji *et al.* Test of lepton universality in beauty-quark decays. *Nature*, 18, 2022.

[41] J. C. Bernauer *et al.* MUSE: The MUon Scattering Experiment. *SciPost Phys. Proc.*, 2021.

[42] Anusha Liyanage, Michael Kohl, Jesmin Nazeer, and Tanvi Patel. Development of GEM Detectors at Hampton University. *arXiv: Physics - Instrumentation and Detectors*, 2018.

[43] B. S. Henderson *et al.* Hard Two-Photon Contribution to Elastic Lepton-Proton Scattering Determined by the OLYMPUS Experiment. *Physical Review Letters*, 118, 2017.

[44] W. Lin *et al.* The muse beamline calorimeter. Unpublished manuscript.

[45] P. Gianotti *et al.* The Straw Tube Trackers of the PANDA Experiment. *arXiv: Physics - Instrumentation and Detectors*, 2013.

[46] P. Roy *et al.* A Liquid Hydrogen Target for the MUSE Experiment at PSI. *Nuclear Instruments and Methods in Physics Research Section A: Accelerators, Spectrometers, Detectors and Associated Equipment*, 949, 2020.

[47] T. Rostomayan *et al.* Suppression of the background originating from the muse target vacuum chambers beam exist window posts. *Nucl. Instrum. Methods A*, preprint, unpublished.

[48] J. C. Bernauer *et al.* Measurement of the Charge-Averaged Elastic Lepton-Proton Scattering Cross Section by the OLYMPUS Experiment. *Physical Review Letters*, 126, 2021.

[49] MUSE Collaboration. Muse analysis report. Submitted in January 2024 in accordance with the instructions of the January 2023 BVR53 MUSE subcommittee.

[50] R.B. Stewart and H.M. Roder. *"Technology and Uses of Liquid Hydrogen"*. Pergamon Press, New York, 1964.

[51] B. M. Preedom and R. Tegen. Nucleon electromagnetic form factors from scattering of polarized muons or electrons. *Physical Review C*, 36, 1987.

[52] J. J. Kelly. Simple parametrization of nucleon form factors. *Physical Review C*, 70, 2004.